DOCTORAL THESIS

Physico-chemical Study of some Perovskite-type Methylammonium Trihalogenometallates

by

Noriko Onoda-Yamamuro

Department of Chemistry

Faculty of Science

Osaka University

1992

Doctoral Committee

Professor Hiroshi Suga

Professor Shichio Kawai

Professor Michio Sorai

Abstract

Heat capacities of $CH_3NH_3PbX_3$ (X = Cl, Br, I) were measured between 13 and 300 K (365 K for the iodide). Two anomalies were found both in the chloride and the iodide, and three in the bromide. All the phase transitions were of the first order, although the highest temperature transitions in the bromide and the iodide were close to the second order. Their temperatures and entropies are as follows,

$CH_3NH_3PbCl_3$; 171.5 K (14.6 J $K^{-1}mol^{-1}$), 177.2 K (10.0 J $K^{-1}mol^{-1}$)

$CH_3NH_3PbBr_3$; 148.8 K (11.2 J $K^{-1}mol^{-1}$), 154.0 K (4.1 J $K^{-1}mol^{-1}$), 236.3 K (8.2 J $K^{-1}mol^{-1}$)

$CH_3NH_3PbI_3$; 161.4 K (19.0 J $K^{-1}mol^{-1}$), 330.4 K (9.7 J $K^{-1}mol^{-1}$)

The magnitudes of the transition entropies indicate that the phase transitions are of the order-disorder type. They are interpreted in terms of three possible statistical models involving the methylammonium ions disordered as to the orientation of the C-N axis itself and around the C-N axis. Infrared line width of the ν_{12} vibration of the methylammonium ion depended markedly on temperature and was interpreted as caused by the hindered rotational motion in the cubic and tetragonal phases.

Complex dielectric permittivities of $CH_3NH_3PbX_3$ (X = Cl, Br, I) were measured at frequencies between 20 Hz and 1 MHz and at temperatures between 20 and 300 K (15 and 350 K for the iodide). Discontinuities or a sharp bend of the real part of the dielectric permittivity occurred at the phase transitions, except at the tetragonal(I4/mcm)-cubic phase transition where the permittivity showed no apparent change. The dielectric behavior in

the cubic and tetragonal(I4/mcm) phases are well described by a modified Kirkwood-Fröhlich equation. Dielectric dispersions were found in the orthorhombic phases of $CH_3NH_3PbBr_3$ and $CH_3NH_3PbI_3$ at temperatures between 30 K and 120 K.

Pressure-temperature phase relations of $CH_3NH_3PbX_3$ (X = Cl, Br, I) crystals were studied by using a high pressure DTA apparatus in the range between 0.1 and 200 MPa. A triple point was found in each compound below 100 MPa. By pressurization, the low pressure phases disappeared at the triple point in the chloride and bromide while a new high-pressure phase appeared in the iodide. The pressures and temperatures of the triple points are 75.1 MPa, 175.7 K for $CH_3NH_3PbCl_3$, 43.2 MPa, 152.9 K for $CH_3NH_3PbBr_3$, and 84.8 MPa, 176.2 K for $CH_3NH_3PbI_3$. All the boundaries between the cubic and tetragonal phases are upward convex and that of the iodide has a maximum at about 120 MPa. Other phase boundaries are essentially straight lines in the measured pressure and temperature ranges. By the use of the Clausius-Clapeyron equation, the transition volumes were calculated from the slopes of the phase boundaries and the transition entropies obtained in the calorimetric experiment.

Heat capacity of $CH_3NH_3SnBr_3$ was measured between 13 and 300 K. Four anomalies were found. Their temperatures and entropy changes are : 46.0 K, 0.37 J $K^{-1}mol^{-1}$ (H); 188.2 K, 6.02 J $K^{-1}mol^{-1}$ (F); 213.0 K (H) and 229.4 K, 18.98 J $K^{-1}mol^{-1}$ (F), where H and F mean higher order and first order transitions, respectively. The last entropy value is the sum of the entropies of the two highest-temperature transitions. The transition entropies indicate that the transition at 46.0 K is of the displa-

cive type and those at 188.2 K and 229.4 K of the order-disorder type. The total of the transition entropies is consistent with the orientational disorder expected for a methylammonium ion in a cubic environment. The electric properties changed from insulating to semiconducting at the 229.4 K transition where the conductivity increased by a factor of 10^4 as the transition temperature was traversed from below. Thermal activation energy of 29.1 kJ mol^{-1} was determined for the conductivity process in the high temperature phase. A dielectric dispersion was found below 150 K for frequencies between 20 Hz and 1 MHz. A Cole-Cole analysis of the dielectric permittivities showed that the relaxation is characterized by a strong deviation from a single Debye process. Pressure-temperature phase relation was studied by high pressure DTA at pressures between 0.1 and 160 MPa and at temperatures between 90 and 300 K. The phase transition observed at 213 K in the calorimetric study at 0.1 MPa was not detected. The phase boundary between the cubic and the lower temperature phases is essentially a straight line with negative slope in the observed pressure range.

Two types of $CH_3NH_3SnI_3$ samples, $CH_3NH_3SnI_3$(T) and $CH_3NH_3SnI_3$(G), were obtained. No structural difference between the two samples was recognized at room temperature in the observed X-ray powder diffraction patterns. Heat capacities were measured for both samples between 13 and 300 K (350 K for $CH_3NH_3SnI_3$(T)). For $CH_3NH_3SnI_3$(T), five anomalies were found. Their temperatures and entropy changes are 98.5 K, 2.4 J $K^{-1}mol^{-1}$(F); 109.4 K(F) and 114.7 K, 6.7 J $K^{-1}mol^{-1}$(F); 150.5 K(H) and 272.3 K, 12.9 J $K^{-1}mol^{-1}$(F). The second and the last

entropy values are the sum of the entropies of the two transitions, respectively. For $CH_3NH_3SnI_3$(G), a glass transition was found at 129 K. Comparison of the total entropies of the two samples at sufficiently high temperature showed that $CH_3NH_3SnI_3$(G) lost most of the orientational entropy due to the $CH_3NH_3^+$ ion at the lowest temperature. The electrical conductivities of the two samples were the same (1×10^4 S m^{-1}) at 300 K. They differed markedly at lower temperature, though both of them remained metallic and showed uneven temperature dependence at about the same temperature regions. High pressure DTA study was made on $CH_3NH_3SnI_3$(T) at pressures between 0.1 Pa and 160 MPa. The phase transitions observed at 115 K and 150 K in the calorimetric measurement at 0.1 MPa were not detected. The phase boundary between the cubic and the lower temperature phases is essentially straight with positive slope in the observed pressure range. In the low temperature range, p-T phase relation is complicated with two triple points in a narrow pressure range. Their locations are (~59 MPa, 99.4 K) and (98 MPa, 106 K). The low and high pressure phases, which are separated by the phase boundary connecting the two triple points, exist in a narrow temperature range between the lowest and medium temperature phases.

Contents

Chapter 1
INTRODUCTION

1.1 Historical Background

Disorder in crystals has long fascinated many scientists. Ordering of orientationally disordered molecules and ions is of interest because it is a clear indication of the role played by intermolecular forces in determining macroscopic properties of a substance.

Orientational disorder arises when the polyatomic molecule or ion has two or more possible and distinguishable orientations available to them in the crystalline lattice. If a disordered crystal is cooled down, the crystal is expected to undergo one or more phase transitions and becomes ordered finally. The decrease in entropy ΔS associated with the order-disorder phase transition can be related to the molecular (or ionic) disorder by the following relation,

$$\Delta S = R \ln (W_h/W_l). \qquad (1.1)$$

Here W_h and W_l are the numbers of accessible orientations in the high and low temperature phases. This simple equation often provides important physical insight into the mechanism of the order-disorder phase transition.

From the thermodynamic standpoint, the phase transition can be classified according to their *order* (the Ehrenfest classification). A transition is said to be of the n'th order when any physical quantities corresponding to the n'th derivative of the

Gibbs free energy are discontinuous at the phase transition. In the present study, the phase transitions are divided into the first order and higher order phase transitions as is widely done rather than into the first and second ones. Discontinuous change occurs in volume (= $(\partial G/\partial P)_T$) or entropy (= $-(\partial G/\partial T)_P$) at a first order phase transition, while continuous change occurs at a higher order phase transition.

There is another path that the disordered crystal passes through on cooling. In some cases, orientationally disordered crystal does not undergo a phase transition and retains a definite amount of entropy at 0 K. The ordering is the thermally activated process. When the disordered crystal is cooled, reorientational motion of the molecules becomes slower with decreasing temperature. If the motion is too slow to be observed in the time scale of experiment, the crystal is in a glassy state. This means that the orientational freedom of the molecules (or ions) has been frozen in the crystal at some temperature (the glass transition temperature) where the entropy and other thermodynamic properties of the crystal start to deviate from its equilibrium values. The crystal then possesses a finite amount of entropy at 0 K (residual entropy). On heating, enthalpy relaxation from the nonequilibrium state to the equilibrium state in the crystal begins to be observed at the temperature where the relaxation time is comparable to the experimental time scale.

Methylammonium ion $CH_3NH_3^+$ (abbreviated as MA ion hereafter) can have two types of orientational disorder in the crystal: One is the orientation of the C-N axis relative to the crystal axes

(type A) and the other related to the rotation around the C-N axis (type B). The MA ion is often orientationally disordered to satisfy the site symmetry in the crystal. The corresponding entropy is expected to decrease on cooling through one or more phase transitions. A number of crystals containing MA ion are known to undergo phase transitions. A list of such compounds is shown in Table 1-1. Phase transitions involving the A type of disorder are found in MAX (X=Br, I) [1, 2], $MAClO_4$ [3, 4], $MANO_3$ [5], $(MA)_2SO_4$ [6] and $(MA)_2[TeX_6]$ (X=Cl, Br, I) [7, 8]. Those involving the B type of disorder are found in MAX (X=Cl, Br, I) [9, 10], $(MA)_2[SnCl_6]$ [11] and $(MA)_2[TeX_6]$ (X=Cl, Br, I) [7, 8]. Recently, the ordering process around the C-N axis was confirmed in MAI [12] and $(MA)_2[SnCl_6]$ [13] by neutron diffraction experiments. A glass transition has not been found for MA compounds.

It is to be noted that many crystals formed by MA ion have cubic symmetry in the highest temperature phase even though the cation is polar and has the symmetry of C_{3v} at the most . Figure 1-1 shows the ideal (cubic) perovskite structure. The MA ion is located at the center of the regular cube and is surrounded by 12 X and 8 B. In contrast to ABO_3-type oxides and ABF_3-type fluorides, only a limited number of ABX_3-type chlorides, bromides and iodides crystallize in the perovskite structure.

As is shown in Table 1-1, all of the three $MAPbX_3$ compounds undergo phase transitions. Transition temperatures and structures were determined by dielectric and X-ray diffraction studies [14]. For $MASnBr_3$, phase transitions were found at 189 K, 214 K and 233 K by NQR and DTA studies [15]. For $MASnI_3$, a phase transition was found at 273 K by DTA experiments [16]. However,

Table 1-1 Structures and transition temperatures of some typical MA compounds.

MA^+X^- (NaCl or CsCl type)

MACl	? (β)	220	? (γ)	261	P4/nmm (α)					1,2
MABr	? (β)	280	P4/nmm (α')	385	P4/nmm (α)					3,4,5
	Pbma (δ)	197								
MAI	? (β)	220	P4/nmm (α')	415	Pm3m (ε)					3,6,7,8
	Pbma (δ)	166								
MASCN	?	242	?							9
$MABF_4$	?	250	?							10
$MAClO_4$	$P2_1/n$	321	tetragonal	451	Pm3m					11,12
$MANO_3$	?	245	Pcmn	352	?					13

$(MA^+)_2X^{2-}$ (anti-fluorite type)

$MASnCl_6$	R$\bar{3}$	154	R$\bar{3}$m							14,15,16
$MASnBr_6$	(R$\bar{3}$)	146	R$\bar{3}$m							14,15
$MATeCl_6$	?	73	R$\bar{3}$m	137	?	155	?	226	P$\bar{3}$ 439 Fm3m	17,18
$MATeBr_6$	?	129	?	164	?	289	Fm3m			19,20
$MATeI_6$	?	66	?	116	Fm3m					19,20
$MAPtCl_6$	(R$\bar{3}$)	125	R$\bar{3}$m							14,15,16

$MA^+A^{2+}(X^-)_3$ (perovskite type)

$MAPbCl_3$	$P222_1$	173	P4/mmm	179	Pm3m					21
$MAPbBr_3$	$Pna2_1$	145	P4/mmm	155	I4/mcm	237	Pm3m			21
$MAPbI_3$	$Pna2_1$	162	I4/mcm	327	Pm3m					21
$MASnBr_3$	?	189	?	214	?	233	Pm3m			22
$MASnI_3$	?	273	Pm3m							23

References to Table 1-1.

1. J. G. Aston and C. W. Ziemer, *J. Am. Chem. Soc.* **68**, 1405 (1946).
2. E. W. Hughes and W. N. Lipscombe, *J. Amer. Soc.* **68**, 1970 (1946).
3. A. Cabana and C. Sandorfy, *Spectrochim. Acta* **18**, 843 (1962).
4. H. Ishida, R. Ikeda and D. Nakamura, *J. Phys. Chem.* **86**, 1003 (1982).
5. E. J. Gabe, *Acta Cryst.* **14**, 1296 (1961).
6. H. Ishida, R. Ikeda and D. Nakamura, *Phys. Status Solidi* **A70**, K151 (1982).
7. O. Yamamuro, M. Oguni, T. Matsuo and H. Suga *Thermochim. Acta* **98**, 327 (1986).
8. O. Yamamuro, T. Matsuo, H. Suga, W. I. F. David, R. M. Ibberson and A. J. Leadbetter, *Acta Crystallogr.* B, in press.
9. H. Ishida, R. Ikeda and D. Nakamura, *Bull. Chem. Soc. Jpn.* **55**, 3116 (1982).
10. O. Yamamuro, M. Oguni, T. Matsuo and H. Suga, *Thermochim. Acta* **99**, 67 (1986).
11. M. Stammler, R. Bruenner, W. Schmidt and D. Orcutt, *Advan. X-ray Anal.* **9**, 170 (1966).
12. P. F. Zanazzi, *Acta Crystallogr.* **B24**, 499 (1968).
13. M. Mylrajan, T. K. K. Srinivasan and G. Sreenivasamurthy, *J. Cryst. Spectrosc. Res.* **15**, 493 (1985).
14. Y. Kume, R. Ikeda and D. Nakamura, *J. Magn. Reson.* **33**, 331 (1979).
15. W. I. F. David, W. T. A. Harrison, R. L. Ward, A. J. Leadbetter, T. Matsuo and H. Suga, *Physica* **B156&157**, 96 (1989).
16. R. W. G. Wycoff, *"Crystal Structures"*, 2nd ed., vol. 5, Interscience, New York, 1966, P142.
17. K. Kitahama and H. Kiriyama, *Acta. Crystallogr.* **A34**, S302 (1978).
18. N. Onoda, T. Matsuo and H. Suga, *Phil. Mag.* **A57**, 245 (1988).
19. Y. Kume, R. Ikeda and D. Nakamura, *J. Phys. Chem.* **82**, 1928 (1978).
20. N. Onoda, T. Matsuo and H. Suga, *J. Phys. Chem. Solids* **47**, 211 (1986).
21. A. Poglitsch and D. Weber, *J. Chem. Phys.* **87**, 6373 (1987).
22. K. Yamada, H. Kawaguchi, T. Matsui, T. Okuda and S. Ichiba, *Bull. Chem. Soc. Jpn.* **63**, 2521 (1990).
23. K. Yamada, T. Matsui, T. Tsuritani, T. Okuda and S. Ichiba, *Z. Naturforsch.* **45a**, 307 (1990).

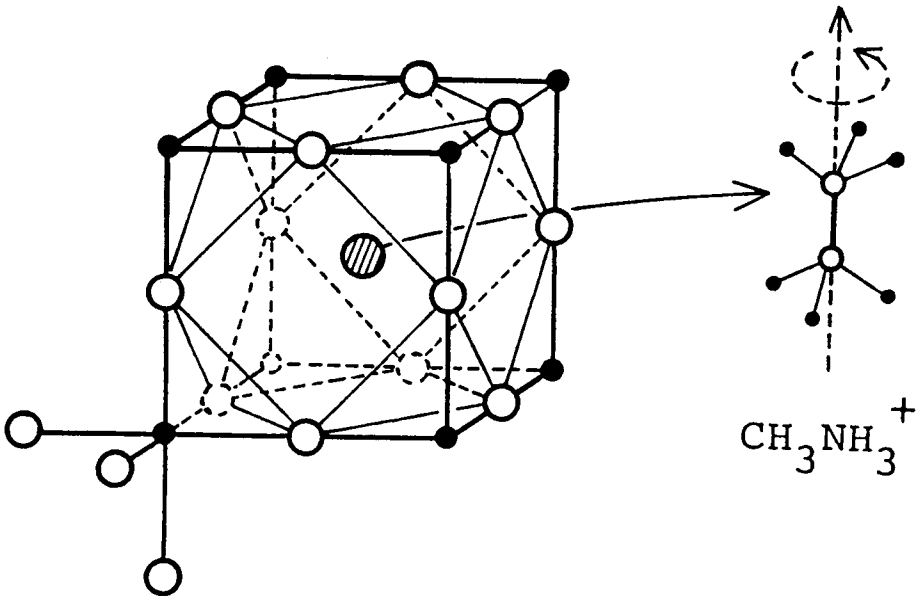

Fig. 1-1 Cubic perovskite structure of ABX_3.
A: shaded large circle, B: filled small circle,
X: empty large circle.
$CH_3NH_3^+$ replaces A in $CH_3NH_3BX_3$.

absence of quadrupole splitting at 85 K in Mossbauer spectroscopy [17] suggested another possibility that the crystal retains the cubic symmetry down to 85 K. Crystal structures of the low temperature phases of the Sn compounds are not known. By analogy with the other MA compounds, these phase transitions are likely to be due to the orientational ordering of the MA ion. These five compounds were chosen in the present study. The compound $MASnCl_3$ is not known to exist.

Phase behavior at high pressures is another aspect of interest of these compounds. It has been known for ammonium halides NH_4X (X = Cl, Br, I) that a systematic relation holds for the stability of different phases as a function of the anionic size and pressure; the increase in pressure is equivalent to the decrease in ionic size of the halogen (NH_4Cl under atmospheric pressure corresponds to NH_4Br under pressure *etc*) [18]. Closely related phase sequence of $MAPbX_3$ at atmospheric pressure [14] suggests that such a systematic relation may also hold in $MAPbX_3$.

Halogen perovskites containing tin are also interesting for their electric properties. The black crystal $CsSnBr_3$ has the cubic perovskite structure at room temperature and behaves as a metallic conductor over a wide range of temperature [19, 20]. $CsSnI_3$ crystallizes in the orthorhombic structure (distorted perovskite) and shows semiconducting behavior [20]. A drastic change in conductivity from semiconducting to metallic occurs at the orthorhombic-(slightly distorted) tetragonal phase transition at 425 K [16, 20], where the color changes from green to black. High conductivity and metallic luster of these compounds appear to originate in their cubic (or slightly distorted tetragonal)

structure. (an exception is $CsSnCl_3$ which is cubic, of pale color and nonconducting at $T > 360$ K [22].) In contrast, the known monoclinic or orthorhombic crystal modifications of these trihalides are nonconducting.

High conductivity and interesting electrical property are also expected for the MA analogues. Electrical properties of these compounds have already been studied by dc conductivity measurement. The dark-red $MASnBr_3$ crystal exhibits semiconducting behavior in the room temperature phase [17]. The crystal becomes non-conducting at the 233 K phase transition and is an insulator below that temperature [23]. Black crystals $MASnI_3$ is a metallic conductor at room temperature [17]. No significant change in conductivity was found at low temperatures down to 100 K [20].

1.2 The Aim of the Present Study

The aim of the present study is to investigate how orientational ordering of the MA ion proceeds at low temperatures. To clarify the mechanism of the phase transitions and molecular motions of the MA ion, experimental investigation was carried out by use of the following techniques; adiabatic calorimetry, infrared absorption spectroscopy, dielectric permittivity measurement, and powder X-ray diffraction. Adiabatic calorimetry gives the transition entropies which are very important for clarification of the mechanism of the phase transition. The calorimetric measurement detects the isothermal heat absorption at the phase transition which characterizes the first order nature of the phase transitions. High sensitivity and long term stability of

the temperature measurement enable determination of the heat capacity to be made in close vicinity of phase transition points on one hand and slow heat evolution around a glass transition on the other. The complex dielectric permittivity was measured for $MAPbX_3$ and $MASnBr_3$ to investigate the molecular motion of the MA ion. Infrared spectroscopic data gave important information about the molecular motion on the basis of the symmetry of the MA ion and its site in the crystal. Powder X-ray diffraction measurement was carried out for $MASnI_3$ to identify the two samples which were accidentally obtained (see Chapter 5).

High pressure DTA was carried out to investigate the phase transition as functions of temperature and pressure, and to examine whether or not a systematic relation described above exists in the present series of compounds. The pressure dependence of the phase transition temperature is a useful piece of information for discussion of the mechanism of the phase transition.

AC conductivity was measured for $MASnBr_3$ to examine the electrical property more precisely. For $MASnI_3$, dc conductivity measurement was extended to lower temperatures based on the new information that the two types of samples exist. On the basis of the results of the other experiments in this work, how the orientational ordering affects the electrical property was investigated.

In this thesis, experimental details are described in Chapter 2. The results and discussion are described for $MAPbX_3$ (X = Cl, Br, I) in Chapter 3 and $MASnX_3$ (X = Br, I) in Chapters 4 and 5. Since the behavior of the Sn compounds was rather different, they

are described separately in two chapters; $MASnBr_3$ in Chapter 4 and $MASnI_3$ in Chapter 5. In the last Chapter 6, general discussion and conclusion are given.

References to Chapter 1

1. M. Tansho, D. Nakamura and R. Ikeda, *Z. Naturforsch.*, 44a, 738 (1989).
2. H. Ishida, R. Ikeda and D. Nakamura, *Phys. Status Solidi*, A70, K151 (1982).
3. M. Stammler, R. Bruener, W. Schmidt and D. Orcutt, *Adv. X-ray Anal.*, 9, 170 (1968).
4. P. F. Zanazzi, *Acta Crystallogr.*, B24, 499 (1968).
5. H. Ishida, R. Ikeda and D. Nakamura, *Chem. Lett.*, 1943 (1982).
6. H. Ishida, N. Matsuhashi, R. Ikeda and D. Nakamura, *Chem. Lett.*, 1859 (1985).
7. N. Onoda, T. Matsuo and H. Suga, *J. Phys. Chem. Solids*, 47, 211 (1986).
8. N. Onoda, T. Matsuo and H. Suga, *Phil. Mag.*, A57, 245, (1988).
9. J. G. Aston and C. W. Ziemer, *J. Am. Chem. Soc.*, 68, 1405, (1946).
10. O. Yamamuro, M. Oguni, T. Matsuo and H. Suga, *J. Chem. Thermodyn.*, 18, 939 (1986).
11. T. Matsuo, M. Ueda and H. Suga, *Chem. Phys. Lett.*, 82, 577 (1981).
12. O. Yamamuro, T. Matsuo, H. Suga, W. I. F. David, R. M. Ibberson and A. J. Leadbetter, *Acta Crystallogr.*, B, in press.
13. W. I. F. David, W. T. A. Harrison, R. L. Ward, A. J. Leadbetter, T. Matsuo and H. Suga, *Physica B*, 156&157, 96 (1989).

14. A. Poglitsch and D. Weber, *J. Chem. Phys.*, 87, 6373 (1987).
15. K. Yamada, S. Nose, T. Umehara, T. Okuda and S. Ichiba, *Bull. Chem. Soc. Jpn.*,, 61, 4265 (1988).
16. K. Yamada, T. Tsuritani, T. Okuda and S. Ichiba, *Chem. Lett.*, 1325 (1989).
17. D. Weber, *Z. Naturforsch.*, 33b, 862 (1978).
18. Y. Yamada, M. Mori and Y. Noda, *J. Phys. Soc. Jpn.*, 32, 1565 (1972).
19. J. Barrett, S. R. Bird, J. D. Donaldson and J. Silver, *J. Chem. Soc. A*, 3105 (1971).
20. K. Yamada, T. Matsui, T. Tsuritani, T. Okuda and S. Ichiba, *Z. Naturforsch.*, 45a, 307 (1990).
21. P. Mauersberger and F. Huber, *Acta Crystallogr.*, B36, 683 (1980).
22. J. D. Donaldson and J. Silver, *J. C. S. Dalton*, 666 (1973).
23. K. Yamada, H. Kawaguchi, T. Matsui, T. Okuda and S. Ichiba, *Bull. Chem. Soc. Jpn.*, 63, 2521 (1990).

Chapter 2

EXPERIMENTAL

2.1 Samples

$MAPbX_3$ (X = Cl, Br, I) crystals were prepared by drop-by-drop addition of aqueous solution of $Pb(CH_3CO_2)_2$ to an excess quantity of hot aqueous solution of MAX (X = Cl, Br, I) [1] and slow cooling to about 5 °C. For $MAPbI_3$, the temperature was kept above 40 °C because otherwise yellow crystals of the composition $(MA)_4PbI_6 \cdot 2H_2O$ formed [2]. The cube-shaped crystals of 1-2 mm in the edge were obtained. They were colorless (chloride), orange (bromide) and black (iodide).

$MASnBr_3$ crystals were prepared by drop-by-drop addition of anhydrous ethanol solution of CH_3NH_3Br to a boiling ethanol solution of $SnBr_2$ and slow cooling of the mixture in an atmosphere of dry N_2 [3]. $SnBr_2$ was purified by sublimation in an evacuated glass tube. CH_3NH_3Br was recrystallized from ethanol. Cube-shaped dark red crystals of 1-2 mm in the edge were obtained.

$MASnI_3$ crystals were prepared by solid state reaction [4]. SnI_2 was purified by sublimation in an evacuated glass tube. CH_3NH_3I was recrystallized from ethanol. Stoichiometric amounts of finely powdered SnI_2 and CH_3NH_3I crystals were mixed and ground together in a mortar in an atmosphere of dry N_2 and then kept at 170 °C for 3 days in a glass tube filled with He gas. Black powder crystals with metallic luster were obtained. The material thus prepared was sensitive to unidentified small change of the reaction condition, and two types of samples were acciden-

tally obtained. One showed a phase transition at 272 K, and the other a glass transition (see Chapter 5). They are designated as $MASnI_3$(T) and $MASnI_3$(G) hereafter. In most cases, $MASnI_3$(T) was obtained. At present, specific conditions for preparation of the different modifications have not been identified.

Elemental analysis gave the following results.

$MAPbCl_3$: C 3.58 %(calc. 3.48 %), H 1.82 %(1.75 %), N 4.09 %(4.05 %), Pb 59.56 %(59.95 %), Cl 30.87 %(30.77%);

$MAPbBr_3$: C 2.50 %(2.51%), H 1.35 %(1.26 %), N 2.92 %(2.92 %), Pb 43.20 %(43.26 %), Br 50.08 %(50.05 %);

$MAPbI_3$: C 1.90 %(1.94 %), H 0.98 %(0.98 %), N 2.29 %(2.26 %), Pb 33.37 %(33.42 %), I not analyzed;

$MASnBr_3$: C 3.13 %(3.08 %), H 1.61 %(1.55 %), N 3.53 %(3.59 %), Sn 30.0 %(30.4 %), Br 61.1 %(61.4 %);

$MASnI_3$: not analyzed.

$MASnCl_3$: the compound is not known.

For the complex permittivity and conductivity measurements, powdered crystals were pressed to form a disk, 13 mm in diameter and about 1 mm in thickness. For $MAPbI_3$ and $MASnX_3$ (X = Br, I), the disks were prepared in an atmosphere of dry N_2 to prevent the decomposition. The disk was annealed at 380 K for 2~3 hours to remove the effect of the pressure applied. Gold was vapor-deposited to the circular surfaces of the disk as electrodes.

2.2 Heat Capacity

The heat capacity was measured for $MAPbX_3$ (X = Cl, Br, I) and $MASnX_3$ (X = Br, I). In adiabatic calorimetry, the average heat

capacity C of the cell and sample is given by

$$C = \Delta E / \Delta T, \tag{2.1}$$

where ΔE is the supplied energy and ΔT is the temperature increase. The molar heat capacity of the sample C_p is calculated from C using the following equation,

$$C_p = (C - C_{cell} - C_{He}) / n, \tag{2.2}$$

where C_{cell} is the heat capacity of the sample cell, C_{He} the heat capacity of the helium gas enclosed in the cell with the sample, and n the amount of the sample. C_{cell} was measured in a separate experiment and expressed as a polynomial function of temperature. C_{He} was calculated using the ideal gas heat capacity and the amount of He gas enclosed in the cell.

The heat capacities were measured with a computerized adiabatic calorimeter which operated in the discontinuous heating mode [5,6]. In this mode of operation, the sequence of heat capacity measurement is composed of two alternating periods. One is the rating period during which the calorimetric temperature is measured as a function of time. In this period, attainment of thermal equilibrium in the sample is confirmed by measuring the sample temperature for a certain (typically 600～1200 s) length of time. The other is the energy input period during which a definite amount of electrical energy is supplied to the sample. It is assumed (and the apparatus is so constructed) that all the supplied energy is used to raise the temperature of the sample and cell under an adiabatic condition.

The sample cell was suspended in the double (inner and out-

er) adiabatic shields. The temperature of the inner shield was controlled to follow that of the sample cell as closely as possible. The temperature of the outer shield was regulated so as to provide an environment in which the inner one functioned properly (usually it was kept at a temperature 0.5～1 K lower than the inner one). They were suspended in the double vacuum cans. The spaces within the cans were evacuated to about 10^{-4} Pa by the use of a rotary pump and an oil diffusion pump.

A platinum resistance thermometer (100 Ω at 273 K, the Minco Products, USA) calibrated on the temperature scale IPTS-68 was used for the temperature measurement. An automatic AC resistance bridge (Model A7 and a later Model F17, Automatic System Laboratory Ltd, England) was used to measure the thermometer resistance.

The current through the cell heater and the potential difference across it were measured with a digital multimeter (Model TR 6875, Takeda Riken Co. Ltd., Japan). The measurements of the temperature and the Joule energy, and the calculation of the molar heat capacity of the sample were performed by a personal computer (Model MZ 80B, Sharp Corp., Japan). Temperatures down to 12 K could be obtained by standard cryogenic techniques using liquefied H_2 and N_2. The temperature interval of the measurement was about 1 K below 60 K and about 2 K above it for usual heat capacity measurement. In the vicinity of phase transition temperatures, the temperature increment was reduced to 0.1 K in order to avoid the imprecision due to averaging the heat capacity in a large temperature interval. The precision of heat capacity measurement is within 0.1 % and 0.2 % below and above 20 K.

Two sample cells were made of gold plated copper. Their mass and inner volume were about 14 g and 4.5 cm^3. Helium heat exchange gas of about 10^5 Pa at the ambient temperature was sealed in the cell together with the sample.

The temperature range and the mass of the calorimetric sample of the measurement were as follows:

$MAPbCl_3$; 13-300 K, 6.0483 g (0.017500 mol),

$MAPbBr_3$; 13-300 K, 8.8810 g (0.018541 mol),

$MAPbI_3$; 13-365 K, 9.3384 g (0.015062 mol),

$MASnBr_3$; 12-300 K, 7.1639 g (0.018346 mol),

$MASnI_3$(G); 12-300 K, 9.0696 g (0.017065 mol),

$MASnI_3$(T); 13-350 K, 7.2352 g (0.013614 mol).

2.3 Infrared Absorption

The infrared absorption of $MAPbX_3$ (X = Cl, Br, I) was measured with a JASCO spectrometer Model DS-402G. The spectral slit width was 1 cm^{-1} at 1000 cm^{-1}. The low temperature spectra were obtained with a variable temperature cell using flow of cold nitrogen gas. The sample temperature was detected with a Chromel-Constantan thermocouple embedded in one of the KBr (KCl for $MAPbCl_3$) plates between which the sample was sandwiched and was kept within $\pm$ 0.2 K of the intended temperatures.

2.4 Dielectric Permittivity and AC Conductivity

The complex dielectric permittivity and ac conductivity of the sample were measured for $MAPbX_3$ (X = Cl, Br, I) and $MASnBr_3$. They were determined by measuring the electric capacitance and the dissipation factor. The real and imaginary parts of the di-

electric permittivity ε' and ε'', and the ac conductivity σ_{ac} were determined by using the relations;

$$\varepsilon' = (C - C_0 - C_f)/C_v, \tag{2.3}$$

$$\varepsilon'' = \varepsilon' D, \tag{2.4}$$

$$C_v = \varepsilon_0 S/t, \tag{2.5}$$

$$\sigma_{ac} = \omega \varepsilon'' \varepsilon_0, \tag{2.6}$$

where C is the capacitance with the sample in the cell, C_f the capacitance due to the fringe effect, D the dissipation factor, ε_0 the dielectric constant of the vacuum (= 8.854 pF m^{-1}), d the thickness of the sample, S the area of the electrodes, ω the angular frequency (= $2\pi f$). In this measurement, the stray capacitance C_0 was neglected since it was very small as compared with C itself. The vacuum capacitance C_v was calculated from the geometry of the electrodes.

The measurement was carried out by means of a doubly jacketed low temperature cryostat [7] and a precision LCR meter (Hewlett Packard 4284A). A sample disk was placed on the sample stage. A platinum-cobalt alloy resistance thermometer and a heating wire for the temperature control were fixed to the sample stage. It was surrounded by a temperature-controlled shield and further by a vacuum can. The temperature was controlled with the thermometer and a potentiometer. The off-balance signal from the potentiometer was amplified and fed back to the heater. The accuracy of the temperature measurement below and above 40 K was ± 0.3 K and ± 0.2 K, respectively. Liquid H_2 (He for $MAPbI_3$) and N_2 were used as the coolant for the measurement below and above 90 K. The temperature regions of the measurements were 20-300 K

for $MAPbCl_3$, $MAPbBr_3$ and $MASnBr_3$ and 15-350 K for $MAPbI_3$.

2.5 DC Conductivity

The dc conductivity was measured for $MASnI_3$. The conductivity σ of a sample is given by

$$\sigma_{dc} = \frac{I}{S} \cdot \frac{l}{V}, \tag{2.7}$$

where I is the current, V the voltage, S and l the cross sectional area and the length of the sample. In the present study, a four-probe method was used because the contact resistance was high. Figure 2-1 shows schematically the arrangement of the probes and the sample. Four probes contact a flat surface of the sample material in a row with uniform distance s. The outer two probes (1 and 4) supply a constant current and the inner two (2 and 3) measure the voltage drop across a portion of the sample. The dc conductivity σ_{dc} for a sample is given by

$$\sigma_{dc} = I / (V \cdot C), \tag{2.8}$$

where V is the potential difference, I the constant current and C the correction factor. The factor C is a constant based on the geometry of the sample and probes and varies on a/s for a circular thin plate sample of diameter a and thickness t ($C = \pi t / \ln 2$ for sufficiently large and thin sample) [8].

Figure 2-2 shows a sketch of the sample stage. The probes A are U-shaped platinum wires of 0.5 mm diameter. Each of them was soldered to an edge of a thin plate B made of phosphor bronze as shown in the inset. The plates were then fixed on an electric-

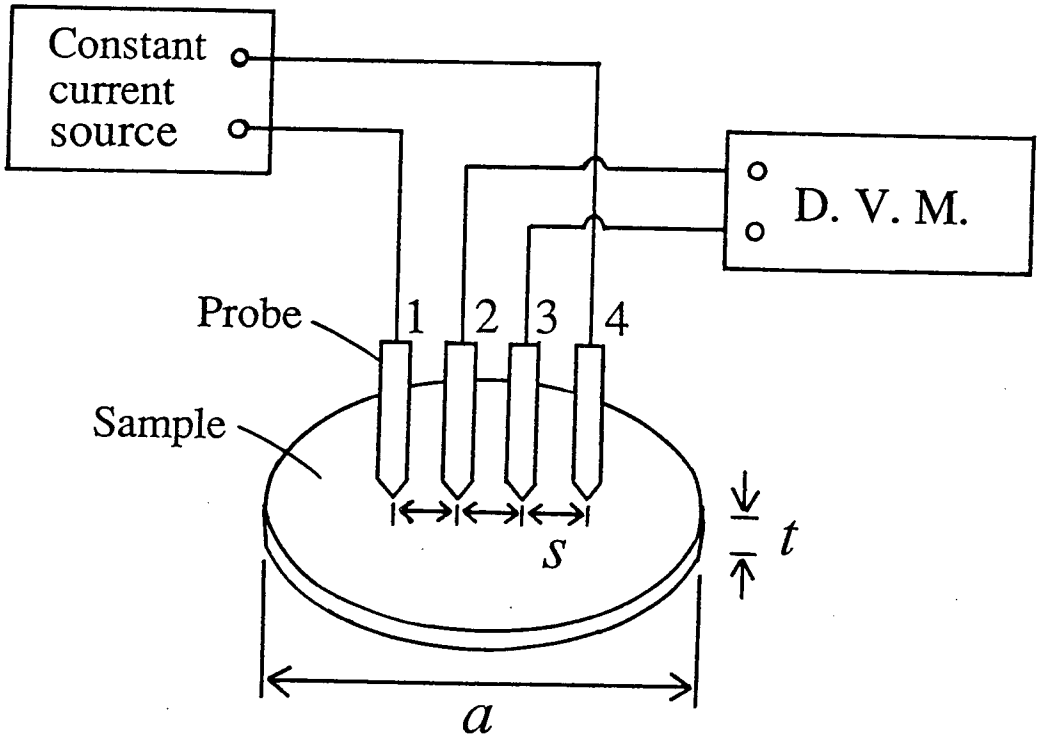

Fig. 2-1 Schematic drawing of the four-probe measurement of electric conductivity.

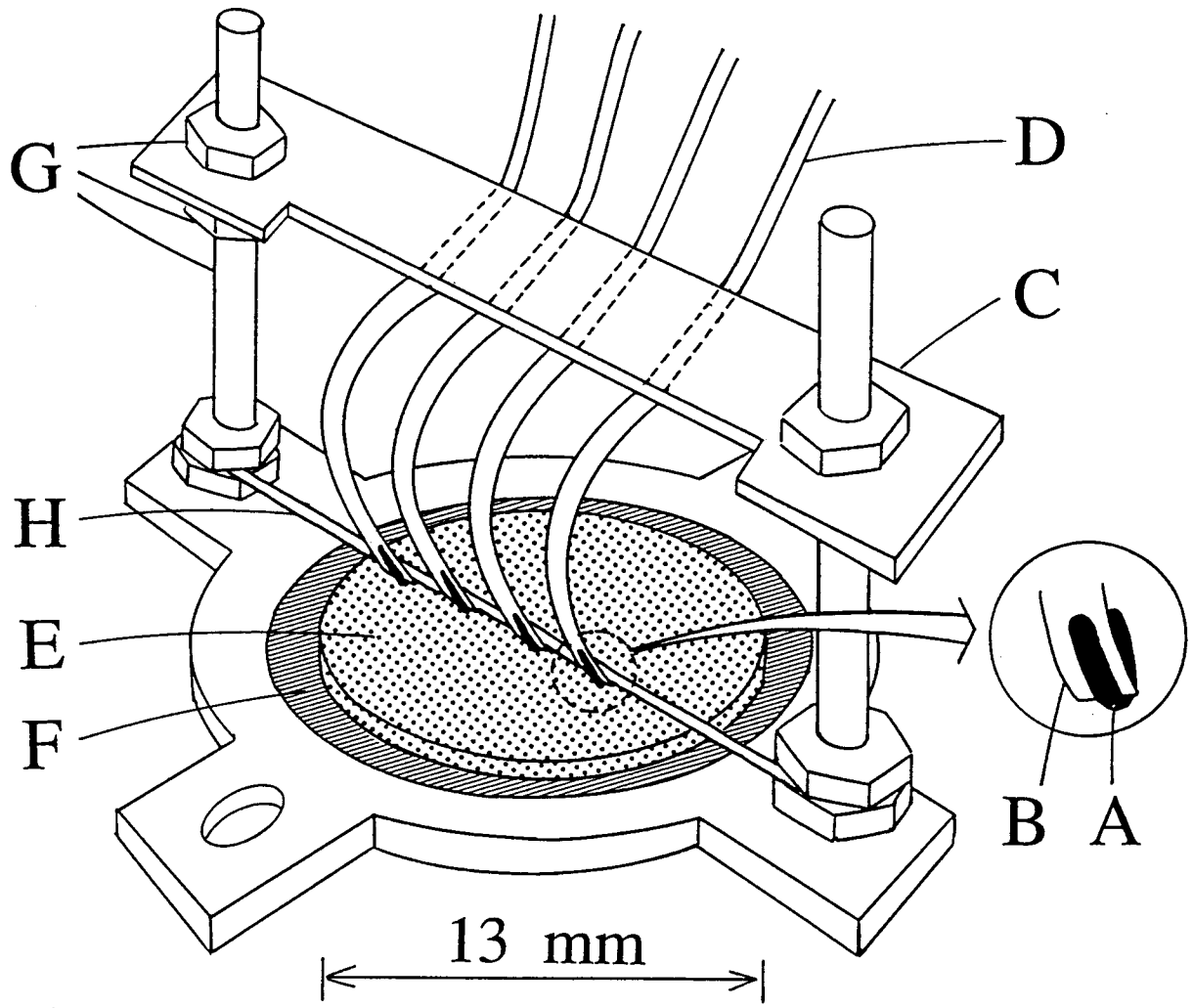

Fig. 2-2 Sectional drawing of the sample stage.
(A): probe, (B): phosphor-bronze plate,
(C): electric insulating plate,
(D): copper lead wire, (E): sample disk,
(F): electric insulating plate, (G): nuts,
(H): teflon wire.

insulating plate C and therein connected to a copper lead wire D by soldering. The sample disk E was placed on another insulating plate F. To obtain good contacts between the probes and the sample surface, the probes were pressed onto the sample by making use of the spring action of the phosphor bronze plates B, which were bent by adjusting the height of the plate C with nuts G. The distances between the neighboring probes were 3 mm. The teflon wire H fixed the positions of the sample disk and the probe.

The sample stage was screwed to a plate in the sample room. The rhodium-iron alloy resistance thermometer and a heating wire for the temperature control were fixed to the plate. The sample stage and the thermostatted plate were surrounded by a temperature-controlled shield and further by double vacuum cans. The resistance of the thermometer was measured potentiometrically. The output signal of the zero detector of the potentiometer was used to control the sample temperature through a negative feedback circuit. Liquid He and N_2 were used as the coolant below and above 100 K. The details of the cryostat will be reported later [9]. Stability of the temperature control was typically $\pm$ 30 mK, and its accuracy $\pm$ 0.1 K.

A constant current was supplied by a current source (Type 2555, Yokogawa, Japan) and the potential difference was measured by a digital multimeter (Model 196, KEITHLEY Instruments, Inc, USA). The potential differences were measured at several different values of electric current. To avoid the thermal and stray electromotive forces, the potential difference was measured for the normal and reverse polarities at each value of the electric current and the average of their absolute values was taken.

Figure 2-3 shows typical *I-V* characteristics observed at 130 K for $MASnI_3$(G). The data gave a straight line passing through the origin, indicating ohmic behavior of the sample. It also indicates that the self heating of the sample was insignificant. The slope of the line gave the resistance of the sample. The value dV/dI determined by the least-squares method was 11.02 ± 0.03 mΩ. Temperature ranges of the measurements were 7-305 K.

2.6 High Pressure DTA

The high pressure DTA experiments were performed for all the samples in the present study with a home-made apparatus described elsewhere [10]. Its essential part is a metal block made of copper-beryllium alloy. Two wells are drilled symmetrically in the block, one being for sample and the other for reference material. Temperature difference between the two wells and the temperature of the reference material were measured by copper-constantan thermocouples encapsulated in stainless-steel sheaths and are recorded on a strip chart as a function of time. The ΔT signal was amplified with an Okura AM 1001 microvolt amplifier or a Guildline photocoupled nanovolt amplifier (model 9460A) before being recorded. The apparatus works in the temperature range between 90 and 400 K.

Hydrostatic pressure was applied to the sample crystals using helium gas as a pressure transmitting medium (nitrogen gas was also used for $MASnBr_3$). Pressure range of the measurement was between 0.1 MPa (atmospheric pressure) and 200 MPa. The applied pressure was not regulated but the pressure change experienced by the sample during traverse of any phase transitions was

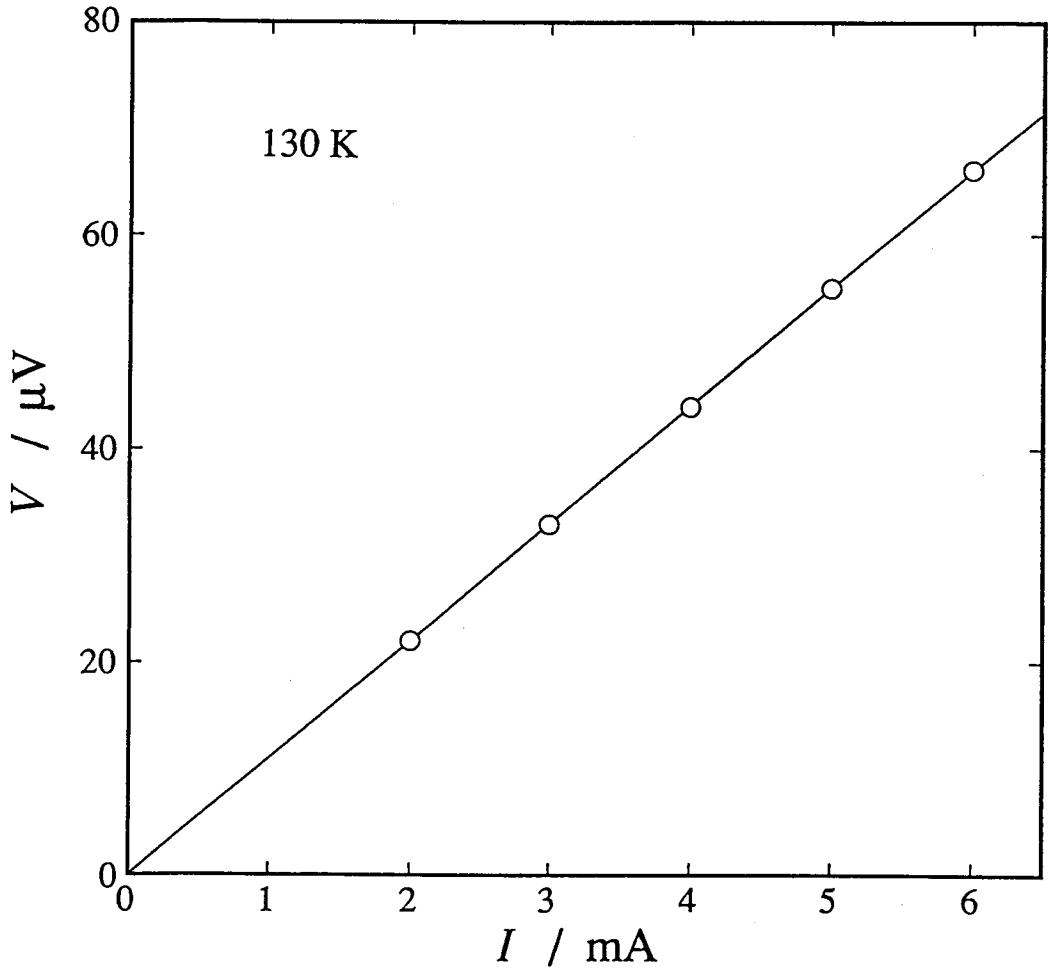

Fig. 2-3 Typical *I-V* characteristics observed at 130 K for $CH_3NH_3SnI_3$(G).

within 0.1 MPa. The DTA curve at each pressure was usually taken in the order of decreasing pressure from the maximum pressure measured. DTA runs were performed several times for each of the samples. The peaks were reproduced well on repeated pressurization except for $MASnI_3$ (see below). The heating rate was 1.0-2.0 K min^{-1} and was kept as nearly constant as possible for the measurement of the same phase transition at different pressures. All the phase transitions observed in the present study were of the first order, and so the transition temperatures were determined as the intersections of the extrapolation of the rising part of the peaks and the base lines. The transition temperatures determined at 0.1 MPa (atmospheric pressure) agreed closely with those determined by the heat capacity measurement.

Two sample containers were used. One was a stainless steel cylinder that fitted closely in the hole of the DTA block. Its top was open and the bottom had a reentrant well which accepted the thermocouple junction. This cell was used for $MAPbX_3$ (X = Cl, Br, I). The other was of a similar structure but had a plug at the upper end, as shown in Fig. 2-4. Its outer tube of 5.6 mm outside diameter and 23 mm length, and bottom plate were made of stainless steel and the reentrant inner tube is made of copper. The plug was made of stainless steel and had holes for the pressure medium to pass through. It was screwed on the outer tube. Fibrous teflon was packed tightly over the sample. This sample cell was embedded in the block symmetrically with respect to the reference(empty) cell and a thermocouple junction was adjusted in height to the middle of the inner tube. With this cell, high base-line stability was obtained as well as with the previous

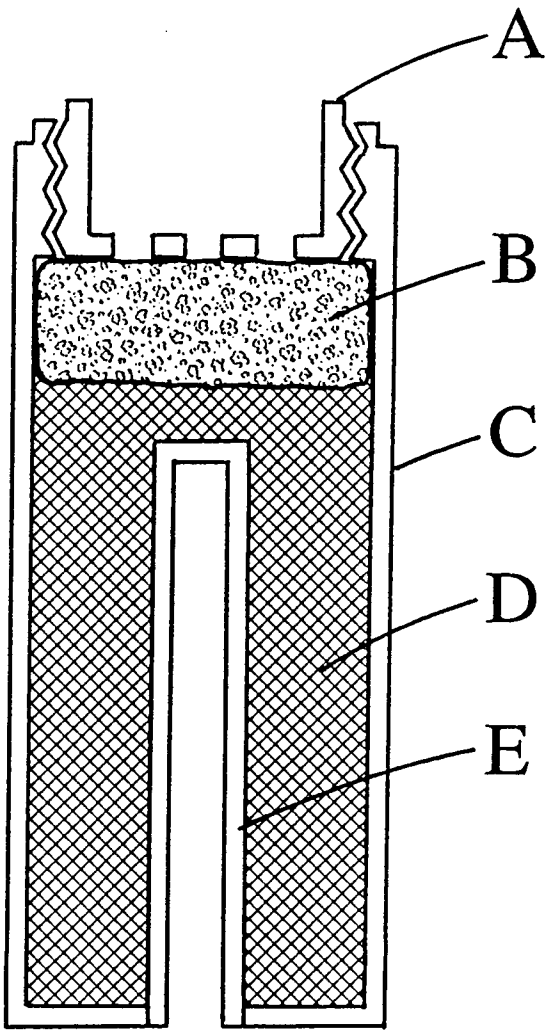

Fig. 2-4 Schematic drawing of the DTA sample cell.
(A): perforated plug, (B): fibrous teflon,
(C): stainless-steel cell, (D): sample,
(E): re-entrant well of copper.

cell. This cell was used for $MASnX_3$ (X = Br, I). The mass of the samples was 0.4-0.7 g.

All of the three $MAPbX_3$ (X = Cl, Br, I) crystals had triple points in the *p-T* range examined (see Section 5 in Chapter 3). The measurements were carried out with low heating rate (0.3-1.0 K min^{-1}) to determine the pressures and the temperatures of the phase transitions as precisely as possible.

For $MASnI_3$, the two peaks observed at 0.1 MPa in the low temperature range were originally very small. The pressure dependent behavior was complicated and broadening of the peaks occurred on repeated pressurization. Transition temperatures were determined as that of the peaks because of the difficulty to distinguish the rising point of the peaks, even though they are of the first order phase transitions.

2.7 Powder X-ray Diffraction

Powder X-ray diffraction of $MAPbI_3$, $MASnI_3$(T) and $MASnI_3$(G) was recorded with a Rigaku RAD-ROC system using Kα radiation. The 2θ range of the measurement was between 10 and 90 °. The low temperature patterns were obtained with a variable temperature stage (RIGAKU 2351 B1) using liquid N_2 as the coolant. The sample temperature was measured with a copper-constantan thermocouple which was soldered to the sample stage.

References to Chapter 2

1. D. Weber, *Z. Naturforsch.*, 33b, 1443 (1978).
2. B. R. Vincent, K. N. Robertson, T. S. Cameron and O. Knop, *Can. J. Chem.*, 65, 1042 (1987).
3. D. Weber, *Z. Naturforsch.*, 33b, 862 (1978).
4. K. Yamada, T. Tsuritani, T. Okuda and S. Ichiba, *Chem. Lett.*, 1325 (1989).
5. M. Tatsumi, T. Matsuo, H. Suga and S. Seki, *Bull. Chem. Soc. Jpn.*, 48, 3060 (1975).
6. T. Matsuo and H. Suga, *Thermochim. Acta*, 88, 149 (1985).
7. T. Matsuo and H. Suga, *Solid State Commun.*, 21, 923 (1977).
8. S. M. Sze, *Physics of Semiconductor Devices*, 2nd. ed., John Wiley (1981), p31.
9. M. Fukai, T. Matsuo and H. Suga, to be published.
10. O. Yamamuro, M. Oguni, T. Matsuo and H. Suga, *Thermochim. Acta*, 99, 67 (1986).

Chapter 3

$CH_3NH_3PbX_3$ (X = Cl, Br, I)

3.1 Introduction

$MAPbX_3$ (X=Cl, Br, I) have the cubic perovskite structure [1]. All of the three compounds undergo phase transitions [2, 3]. Temperature dependent structures determined by Poglitsch and Weber are as follows [2],

$MAPbCl_3$ orthorhombic I —— tetragonal II ———————— cubic
172.9 K 178.8 K

$MAPbBr_3$ orthorhombic II —— tetragonal II —— tetragonal I —— cubic
~145 K 155.1 K 236.9 K

$MAPbI_3$ orthorhombic II ———————— tetragonal I —— cubic
162.2 K 327.4 K

It is to be noted that the bromide has two tetragonal phases. One of them corresponds to the tetragonal phase of the chloride and the other to that of the iodide. According to Poglitsch and Weber, the space groups are as follows [2];

cubic : Pm3m,

tetragonal I : I4/mcm,

tetragonal II : P4/mmm,

orthorhombic I : $P222_1$,

orthorhombic II : $Pna2_1$

They suggested eight equivalent orientations for an MA ion lying along the body diagonals of the lattice as a model of disorder to satisfy the cubic symmetry. The MA ions are disordered also in

the tetragonal phase and become ordered in the orthorhombic phase. They further suggested that the eight-fold disorder might be preserved in the tetragonal I phase. Moreover, they deduced that the C-N axis of the MA ion in the orthorhombic phase has head-to-tail disorder in the chloride whereas it is ordered in the bromide and the iodide. They expected that the dielectric property should reveal a dynamic process in which the orientation of MA ions changes, and carried out the dielectric measurement at temperatures between 100 and 300 K and at frequencies between 50 and 150 GHz. A discontinuity in the dielectric constant was found at the orthorhombic-tetragonal phase transition for all three substances. Above the transition temperatures, the real part ε' of the dielectric constant increased monotonically with temperature. No significant change was found at the tetragonal I-cubic transition in the bromide. The dielectric behavior at and above the transition temperature in the iodide was not studied because of the higher transition temperature. A picosecond relaxation due to the dynamic disorder of the reorientating MA ion was found in the high temperature phases (cubic and tetragonal I). However, the dielectric behavior of the tetragonal II phase was not clear in their measurement because of its narrow temperature range. The comparatively large values (18$\sim$30) of ε' at 100 K suggest that one should expect a further temperature dependence of ε' below 100 K.

Molecular motion of the MA ion was also investigated by ^{1}H, ^{2}H and ^{14}N NMR [3-6]. In the cubic and tetragonal I phases, the MA ion undergoes extremely rapid overall reorientation [3-6]. The reorientation of the C-N axis approaches to the rapidity

calculated for the free ion [4]. In the lower temperature phases (tetragonal II, orthorhombic I and II), the reorientation of the C-N axis seems to be frozen but that around the C-N axis persists [4]. A precessional motion of the C-N axis was suggested in the tetragonal II phase [5,6].

In this chapter, the results of infrared absorption spectroscopy (Section 2), adiabatic calorimetry (Section 3), dielectric measurement (Section 4) and high pressure DTA (Section 5) are reported, and they are discussed in relation to the phase transition and the molecular motion.

The heat capacities were measured with an adiabatic calorimeter to clarify the nature and the mechanism of the phase transition from thermodynamic point of view. Presice temperatures, enthalpies and entropies of transition were determined. The temperature dependence of the transition entropy revealed the nature of the phase transition. The entropy values are interpreted with the structure models of reorientating MA ions.

Temperature variations of the infrared spectra were measured to investigate the molecular motions of MA ions. Temperature dependence of the infrared line width of the ν_{12} vibration (rocking mode) of the MA ion was interpreted as caused by the rotational motion in the cubic and tetragonal I phases. It turned out to be informative in providing additional evidence for rapid rotation of the MA ion in $MAPbX_3$ crystals.

The complex permittivity measurement was extended to lower frequencies (20 Hz-1 MHz) and lower temperatures (~20 K) as required and expected described above. Temperature and frequency dependent dielectric behavior in each phase was investigated in

detail. The results were compared with the structure models suggested by the heat capacity measurement.

A high pressure DTA measurement was carried out at pressures between 0.1 and 200 MPa to investigate the pressure-temperature phase relations. Complicated p-T phase diagrams containing triple points, a new high-pressure phase, and a convex phase boundary with a maximum were determined. By using the Clausius-Clapeyron equation, the transition volumes were calculated from the slopes of the phase boundaries and the transition entropies obtained in the heat capacity measurement.

3.2 Infrared Absorption

3.2.1 Temperature Dependence of the Infrared Spectra

Internal vibrations of an MA ion are classified into A_1, A_2 and E species according to the C_{3v} symmetry of the molecular ion. Fundamental vibrations were assigned by comparison with the well-documented spectra of the MA ion in other compounds [7,8]. The assignment is given in Table 3-1. These frequencies were used in the calculation of the vibrational heat capacity described below (in Section 3.2).

Some of the spectra were strongly dependent on the temperature in its line shape. Figure 3-1 shows the temperature variations of the ν_5 (C-N stretching, $\sim$980 cm^{-1}) and the ν_{12} spectra (rocking, $\sim$910 cm^{-1}) of the MA ion in $MAPbCl_3$, $MAPbBr_3$ and $MAPbI_3$. The arrows in the figures indicate their respective transition temperatures. For the three compounds, the ν_{12} spectra were very broad at room temperature and narrowed as the temperature was reduced. For $MAPbCl_3$, no obvious change of the ν_{12}

Table 3-1 Vibrational frequencies of the $CH_3NH_3^+$ ion (MA ion) in $CH_3NH_3PbX_3$ (X=Cl, Br, I).

Mode	Symmetry	$\tilde{\nu}_{obs}$ / cm^{-1}		
		$CH_3NH_3PbCl_3$	$CH_3NH_3PbBr_3$	$CH_3NH_3PbI_3$
ν_1	A_1	2993	3035	3012
ν_2	A_1	2917	2926	2924
ν_3	A_1	1500	1500	1486
ν_4	A_1	1420	1408	1406
ν_5	A_1	978	966	961
ν_6	A_2	internal rotation, see text.		
ν_7	E	3080	3085	3098
ν_8	E	2963	2967	2963
ν_9	E	1588	1584	1578
ν_{10}	E	1485	1449	1460
ν_{11}	E	1250	1252	1240
ν_{12}	E	922	918	907

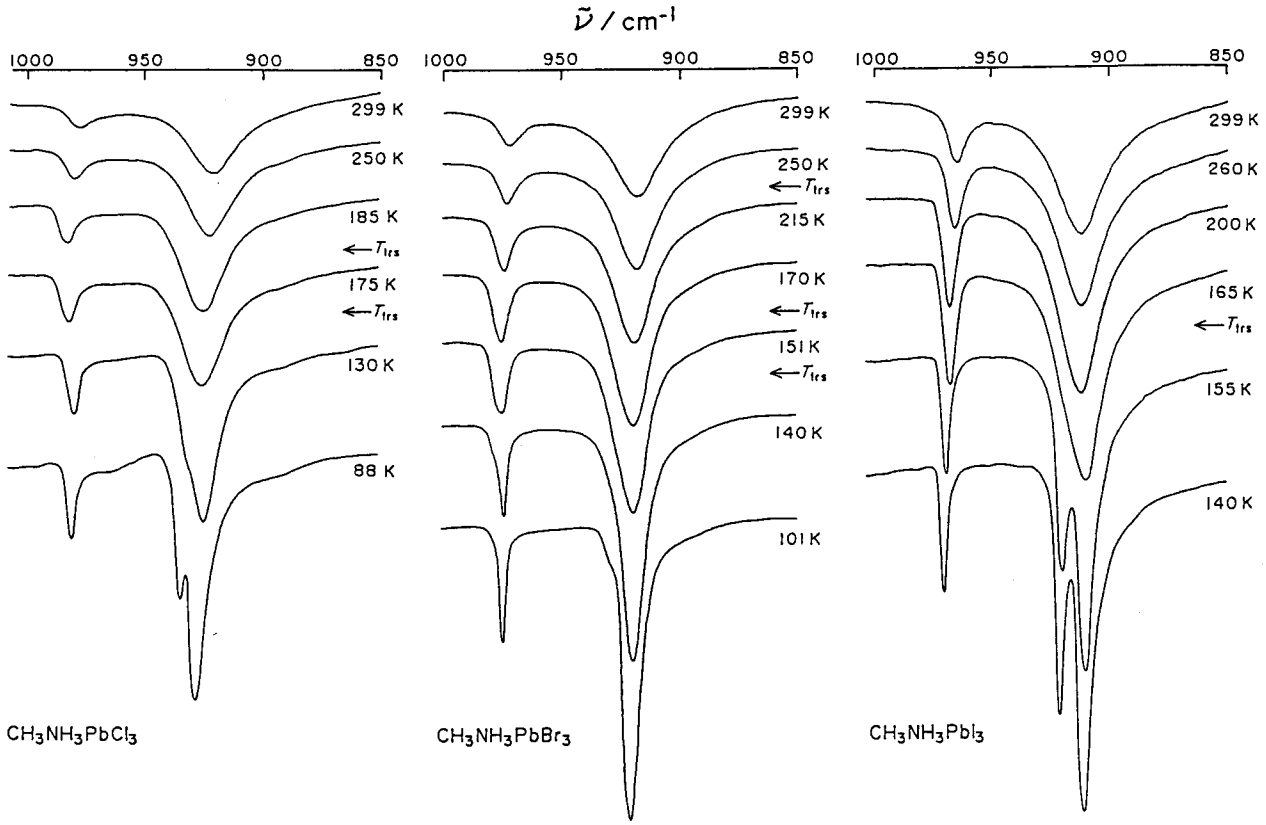

Fig. 3-1 Temperature variation of the infrared spectra in the region of the ν_5 (C-N stretching, ~980 cm^{-1}) and the ν_{12} (rocking, ~910 cm^{-1}) of the $CH_3NH_3^+$ ion in $CH_3NH_3PbX_3$ (X = Cl, Br, I). Arrows indicate the phase transition temperatures.

line shape occurred as the 177.2 K transition temperature (cubic-tetragonal II) was traversed. On further cooling, the spectrum split into two components, which is seen as a shoulder at 130 K and as well-separated peaks at 88 K. For $MAPbBr_3$, the splitting occurred below the 148.8 K phase transition (tetragonal II-orthorhombic II) as a weak shoulder. Except for the narrowing, no drastic change was observed at the phase transition at 236.3 K (cubic-tetragonal I) and 154.0 K (tetragonal I-tetragonal II). The splitting of ν_{12} spectrum in $MAPbI_3$ occurred at the 161.4 K phase transition (tetragonal I-orthorhombic II). The spectrum in the highest temperature phase (>330.4 K) was not recorded.

In all of the compounds, the splitting occurred below the tetragonal-orthorhombic transition rather than the cubic-tetragonal or the tetragonal-tetragonal transition. In the tetragonal phases, the ν_{12} spectra were singlet in these compounds. Apparently the three-fold symmetry about the C-N axis of the MA ion is preserved not only in the cubic phase but also in the tetragonal phases.

3.2.2 Line Broadening of the Infrared Spectra

Line shape of the vibrational spectra is related to the vibrational and rotational correlation functions expressing persistence of the motional states of the absorbing molecules. The two effects (vibrational and rotational) can be separated from each other in Raman spectroscopy by the use of different scattering geometry. This is not possible in infrared spectroscopy. However, it was found previously that the line width of the *E*

mode of the MA ion in $(MA)_2[SnCl_6]$ is much more temperature dependent than that of the A_1 modes [9]. This was explained by the rapid reorientation about the C-N axis [9,10]. The ν_{12} line width of $(MA)_2[TeBr_6]$ and $(MA)_2[TeI_6]$ was analyzed in the same way [11]. The correlation time and the activation energy derived from the line width agreed with those from NMR for these compounds. The same analytical method was applied to the ν_{12} line width of $MAPbX_3$ (X = Cl, Br, I). The ν_{12} line shape was assumed to be Lorentzian ;

$$\ln [I_0(\tilde{\nu}) / I(\tilde{\nu})] = a / [(\tilde{\nu} - \tilde{\nu}_0)^2 + b^2], \qquad (3\text{-}1)$$

where $I(\tilde{\nu})$ is the observed infrared intensity at $\tilde{\nu}$, $I_0(\tilde{\nu})$ the incident intensity, $\tilde{\nu}_0$ the frequency of the band center, and b the half width at the half maximum of the absorption. In fitting the function to the experimental data, the base intensity $I_0(\tilde{\nu})$ was assumed to be linear in $\tilde{\nu}$. The spectra recorded on a strip chart were read on a digitizing tablet and fed numerically into a personal computer. A nonlinear least-squares program written in BASIC was used to determine the best-fit parameter values. Some of the typical results are shown in Fig. 3-2 for $MAPbBr_3$. The line shapes were reproduced well at all temperatures in the cubic and two tetragonal phases.

The line width parameter b is related to the correlation time τ_c by

$$\tau_c = 1/(2\pi cb), \qquad (3\text{-}2)$$

where c is the velocity of light in vacuo [12]. The instrumental width was corrected by the method of Ramsay [13]. A small con-

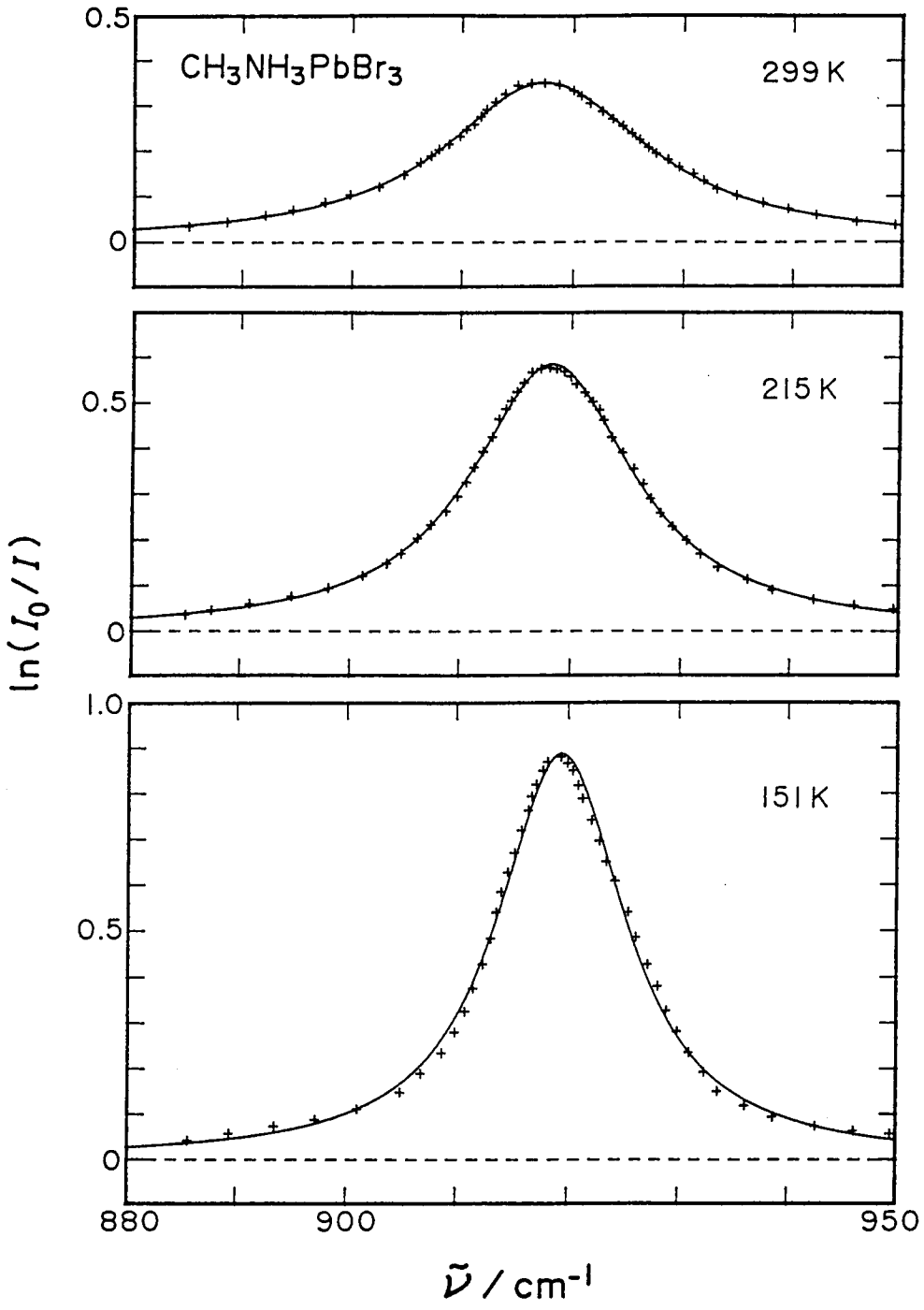

Fig. 3-2 Comparison of the experimental and the best-fit Lorentzian curves of the ν_{12} mode of the CH_3NH_3 ion in $CH_3NH_3PbBr_3$.

stant width remaining at the lowest temperature was determined by the extrapolation based on the Arrhenius law for the temperature dependence of τ_c. For $MAPbBr_3$, the extrapolation was separately carried out for the cubic phase and the tetragonal I phase. The Arrhenius plot of τ_c is given in Fig. 3-3. They were straight lines to a good approximation. The activation energies obtained from the slopes were 2.4 kJ mol^{-1} for the cubic phase of $MAPbCl_3$ and 2.6 kJ mol^{-1} for the tetragonal I phase of $MAPbI_3$. For $MAPbBr_3$, activation energies of 2.4 kJ mol^{-1} and 2.0 kJ mol^{-1} were obtained for the cubic phase and the tetragonal I phase, respectively. They are the activation energy for the hindered rotational motion of the MA ion about the C-N axis (external rotation). For the sake of comparison the activation energies obtained in the same way for other compounds are 3.2 kJ mol^{-1}, 4.0 kJ mol^{-1}, 3.9 kJ mol^{-1} and 3.1 kJ mol^{-1} for $(MA)_2[SnCl_6]$ [9], $(MA)_2[SnBr_6]$, $(MA)_2[TeBr_6]$ and $(MA)_2[TeI_6]$ [11], respectively. For the orthorhombic phase, Furukawa and Nakamura obtained 5.6 kJ mol^{-1} for $MAPbCl_3$ and 3.8 kJ mol^{-1} for $MAPbBr_3$ in a ^1H NMR study. Xu *et al.* obtained 5.1 kJ mol^{-1}, 3.9 kJ mol^{-1} and 5.8 kJ mol^{-1} for the orthorhombic phases of $MAPbCl_3$, $MAPbBr_3$ and $MAPbI_3$, respectively, by the same method [6]. The larger values reported in the NMR studies compared to those determined here indicate that this motion is more hindered in the orthorhombic phase than in the cubic and tetragonal phases.

3.3 Heat Capacity

3.3.1 Heat Capacity

The numerical values of the molar heat capacity are given in

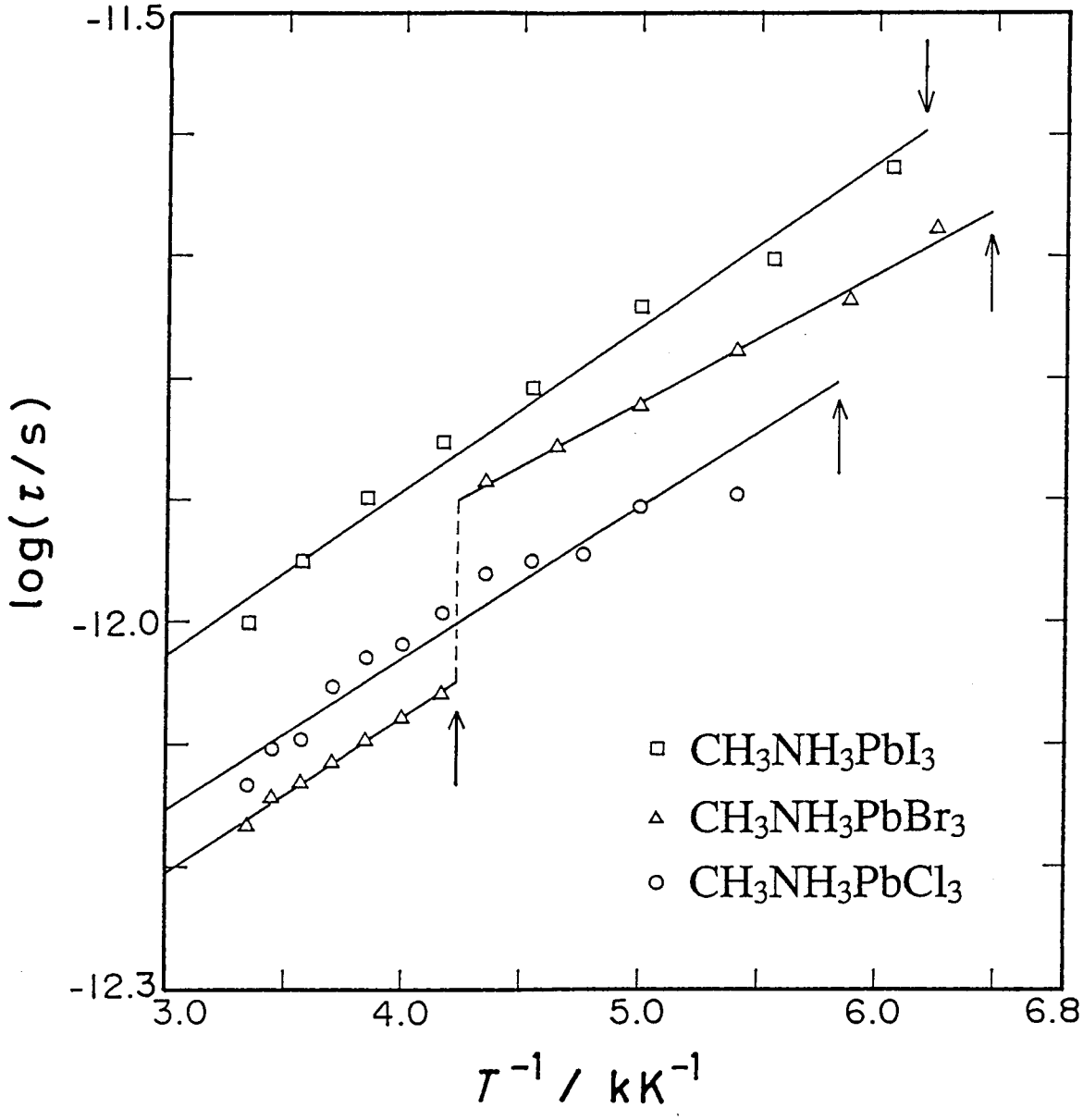

Fig. 3-3 Arrhenius plots of the correlation time τ_c of the reorientation of the $CH_3NH_3^+$ ion in $CH_3NH_3PbX_3$ (X = Cl, Br, I)

○: $CH_3NH_3PbCl_3$, △: $CH_3NH_3PbBr_3$, □: $CH_3NH_3PbI_3$. Arrows indicate the phase transition temperatures.

Tables 3-2, 3-3 and 3-4 and shown in Figs. 3-4, 3-5 and 3-6 for $MAPbCl_3$, $MAPbBr_3$ and $MAPbI_3$, respectively. The dotted curves in the figures represent the normal heat capacities determined as described below (in Section 3.2). Standard thermodynamic functions derived from the calorimetric data are given in Tables 3-5, 3-6 and 3-7 for $MAPbCl_3$, $MAPbBr_3$ and $MAPbI_3$, respectively. For T < 10 K where the heat capacities were not measured, they are calculated by using known vibrational frequencies, barriers of hindered rotations and optimized Debye and Einstein parameters (see Section 3.2).

Two anomalies were found at 171.5 K and 177.2 K in $MAPbCl_3$ and 161.4 K and 330.4 K in $MAPbI_3$, respectively. Three anomalies occurred at 148.8 K, 154.0 K and 236.3 K in $MAPbBr_3$. Their temperatures agree satisfactorily with those which have been reported [2, see Section 3.1]. The phase transitions in $MAPbCl_3$ and two lower temperature phase transitions in $MAPbBr_3$ occur at close temperatures and their pre- and post-transition effects overlap with each other. The highest temperature transitions in $MAPbBr_3$ and $MAPbI_3$ have a strong precursory effect on the heat capacities. It is interesting that the heat capacities of the highest temperature phases are almost constant for all of these compounds.

3.3.2 Determination of the Base Lines of the Heat Capacities

It is assumed that the experimental heat capacity can be divided additively into the normal and the transitional parts. The normal part consists of the vibrational heat capacity and a small correction for the dilation. There are 36 degrees of

Table 3-2 Molar heat capacity of $CH_3NH_3PbCl_3$.

T_{av} / K	C_P / J K^{-1}mol^{-1}	T_{av} / K	C_P / J K^{-1}mol^{-1}	T_{av} / K	C_P / J K^{-1}mol^{-1}	T_{av} / K	C_P / J K^{-1}mol^{-1}	T_{av} / K	C_P / J K^{-1}mol^{-1}
13.09	8.114	46.38	73.88	112.18	136.4	174.34	176.3	226.50	168.2
13.77	9.185	47.86	76.34	114.34	137.4	175.05	177.0	228.91	168.3
14.43	10.26	49.37	78.77	116.54	138.6	175.76	177.7	231.32	168.3
15.09	11.42	50.82	81.13	118.80	139.7	176.47	180.0	233.72	168.3
15.77	12.61	52.29	83.44	121.05	140.8	177.00	223.3	237.16	168.7
16.56	14.09	53.82	85.72	123.29	141.8	177.20	3633	238.50	168.5
17.45	15.83	55.43	88.04	125.51	142.8	177.35	853.4	240.89	168.3
18.37	17.71	57.06	90.32	127.73	143.7	177.61	196.6	243.28	168.4
19.30	19.67	58.66	92.44	130.00	144.7	177.99	179.1	245.66	168.2
20.18	21.56	60.29	94.54	132.33	145.6	178.37	174.8	248.03	168.3
21.08	23.43	61.96	96.57	134.64	146.6	178.75	172.9	250.41	168.3
21.99	25.37	63.66	98.55	136.95	147.4	179.14	172.3	252.77	168.3
22.87	27.20	65.46	100.6	139.25	148.4	179.52	171.7	255.14	168.4
23.76	29.18	67.32	102.7	141.54	149.2	179.91	171.2	257.11	168.5
24.65	31.04	69.15	104.6	143.89	150.1	180.87	170.5	259.47	168.4
25.43	32.72	71.00	106.5	146.29	150.9	182.41	169.9	261.82	168.4
26.13	34.22	72.91	108.4	148.68	151.7	183.95	169.6	264.17	168.6
26.86	35.77	74.89	110.2	151.06	152.6	185.49	169.3	266.52	168.6
27.61	37.37	76.89	112.0	153.45	153.4	187.28	169.1	268.86	168.7
28.29	38.90	78.87	113.7	155.82	154.2	189.33	168.9	271.20	168.7
29.02	40.41	80.82	115.4	158.25	154.9	191.37	168.8	273.53	168.9
29.88	42.28	82.80	117.0	160.73	155.9	193.59	168.6	275.86	169.0
30.73	44.11	84.79	118.6	163.20	156.7	195.88	168.4	278.19	169.0
31.57	45.90	86.36	119.8	164.70	157.3	198.30	168.5	280.51	169.1
32.47	47.81	88.38	121.3	166.76	158.2	200.80	168.3	282.83	169.3
33.43	49.81	90.49	122.8	168.37	159.4	203.27	168.3	285.15	169.3
34.42	51.82	92.69	124.5	169.54	161.5	205.73	168.2	287.46	169.7
35.49	53.97	94.87	125.9	170.28	169.3	208.18	168.1	289.77	170.4
36.70	56.32	97.02	127.4	170.83	202.0	210.63	168.0	291.03	170.8
37.94	58.71	99.15	128.7	171.23	1388	213.07	168.0	293.33	170.1
39.14	60.96	101.26	130.0	171.62	2229	215.50	168.3	295.63	169.8
40.43	63.36	103.42	131.4	172.04	177.0	216.80	168.4	297.93	170.0
41.90	66.05	105.64	132.6	172.60	175.5	219.23	168.3	300.23	170.2
43.43	68.76	107.83	134.0	173.15	175.5	221.66	168.3		
44.93	71.40	110.01	135.1	173.70	175.8	224.08	168.2		

Table 3-3 Molar heat capacity of $CH_3NH_3PbBr_3$.

T_{av} / K	C_P / J K^{-1}mol^{-1}	T_{av} / K	C_P / J K^{-1}mol^{-1}	T_{av} / K	C_P / J K^{-1}mol^{-1}	T_{av} / K	C_P / J K^{-1}mol^{-1}	T_{av} / K	C_P / J K^{-1}mol^{-1}
12.78	14.54	48.72	95.86	115.42	146.6	164.58	168.8	236.31	732.7
13.44	16.37	50.14	98.18	117.42	147.3	167.41	168.9	236.43	241.5
14.17	18.19	51.57	100.3	119.45	148.0	170.22	169.2	236.60	181.2
14.91	20.07	52.99	102.4	121.47	148.8	173.02	169.6	236.78	178.5
15.66	22.06	54.42	104.4	123.48	149.4	175.80	170.1	236.96	176.2
16.43	24.20	55.86	106.3	125.49	150.2	178.58	170.5	237.49	174.9
17.19	26.08	57.28	108.1	127.53	150.8	181.35	170.8	238.40	173.7
17.91	28.21	58.81	109.9	129.59	151.7	184.10	171.3	239.39	173.5
18.62	30.14	60.47	111.9	131.64	152.3	186.84	171.8	240.44	172.8
19.33	31.96	62.09	113.8	133.66	153.0	189.56	172.4	241.56	173.0
20.00	34.01	63.72	115.5	135.65	153.8	191.14	172.6	242.74	172.7
20.68	35.79	65.41	117.2	137.63	154.5	193.30	173.1	243.98	172.9
21.38	37.70	67.12	118.9	139.60	155.3	195.45	173.4	245.30	172.4
22.12	39.57	68.86	120.5	141.55	156.0	197.60	173.7	247.00	171.9
22.85	41.46	70.67	122.0	143.30	157.2	199.75	174.3	249.05	171.9
23.59	43.41	72.50	123.5	144.96	158.5	201.88	174.8	251.10	171.5
24.35	45.36	74.30	124.9	145.91	159.3	204.02	175.0	253.14	171.5
25.11	47.30	76.08	126.3	146.75	161.1	206.14	175.7	255.18	171.1
25.86	49.19	77.89	127.6	147.48	164.2	208.26	176.1	257.22	171.1
26.61	51.07	79.71	128.7	148.09	175.4	210.37	176.6	259.35	170.9
27.42	53.05	81.52	130.0	148.57	468.0	212.47	177.1	261.69	170.9
28.28	55.24	83.31	131.3	148.94	3331	214.57	177.7	264.14	170.7
29.12	57.19	85.13	132.2	149.40	228.5	216.66	178.1	266.59	171.0
29.96	59.20	86.97	133.5	149.94	186.4	218.75	178.5	269.03	170.4
30.89	61.37	88.79	134.4	150.44	186.2	220.83	179.4	271.47	170.5
31.95	63.91	90.60	135.7	151.06	186.9	222.90	180.1	273.90	170.2
33.00	66.38	92.44	136.3	151.68	188.1	224.96	180.8	276.33	170.3
34.07	68.75	94.30	137.5	152.17	191.7	227.02	181.7	278.75	170.5
35.16	71.00	96.16	138.1	152.62	195.1	228.80	182.7	281.17	170.3
36.31	73.51	98.00	139.1	153.07	197.2	230.31	183.7	283.59	170.1
37.62	76.17	99.87	140.0	153.61	203.4	231.56	185.0	286.01	170.0
39.04	78.93	101.76	140.9	154.41	479.6	232.57	186.5	288.42	170.4
40.44	81.58	103.65	141.7	155.23	171.7	233.58	187.4	290.83	171.1
41.78	84.07	105.53	142.8	155.87	169.7	234.55	190.1	293.23	170.6
43.14	86.53	107.46	143.5	156.50	169.1	235.15	191.7	295.64	170.1
44.51	88.92	109.46	144.3	157.14	168.7	235.67	196.4	298.04	170.3
45.84	91.20	111.46	145.1	158.89	168.6	235.85	199.1	300.44	170.7
47.25	93.59	113.44	145.8	161.74	168.5	236.02	201.0		

Table 3-4 Molar heat capacity of $CH_3NH_3PbI_3$.

T_{av} / K	C_P / J K^{-1}mol^{-1}	T_{av} / K	C_P / J K^{-1}mol^{-1}	T_{av} / K	C_P / J K^{-1}mol^{-1}	T_{av} / K	C_P / J K^{-1}mol^{-1}	T_{av} / K	C_P / J K^{-1}mol^{-1}
12.67	22.91	63.61	118.8	152.94	166.8	209.81	169.8	312.94	193.7
13.46	25.28	65.26	120.3	154.36	168.2	211.99	170.3	314.84	194.5
14.32	27.93	66.99	121.8	155.25	168.9	214.15	170.8	316.73	195.4
15.21	30.45	68.75	123.1	156.13	170.0	216.32	171.3	318.62	196.4
16.04	32.91	70.55	124.4	157.01	171.2	218.49	171.6	320.13	197.2
16.84	35.17	72.39	125.7	157.89	172.7	220.66	172.1	322.52	199.1
17.64	37.46	74.26	127.0	158.76	175.6	222.95	172.6	323.52	200.0
18.50	40.01	76.17	128.2	159.43	178.8	225.24	173.1	324.89	201.8
19.39	42.54	78.11	129.4	159.79	180.8	227.52	173.6	325.53	202.7
20.25	44.98	80.08	130.7	160.05	185.1	229.81	174.2	326.45	204.4
21.08	47.22	82.08	131.9	160.31	190.0	232.13	174.6	327.61	207.5
21.94	49.43	83.07	132.5	160.54	197.6	234.50	175.1	328.55	211.2
22.83	51.76	85.20	133.8	160.72	206.8	236.86	175.5	329.04	213.5
23.58	53.71	87.30	134.9	160.90	227.4	239.19	176.1	329.41	217.1
24.33	55.55	89.37	136.0	161.05	266.6	241.50	176.7	329.66	218.9
25.18	57.66	91.42	137.1	161.19	407.5	243.86	177.1	329.91	222.0
26.07	59.80	93.44	138.1	161.38	8410	246.26	177.5	330.15	245.8
27.00	61.99	95.45	139.1	161.65	481.2	248.01	178.0	330.36	856.9
27.91	64.16	97.44	140.1	161.95	164.9	250.35	178.6	330.56	321.7
28.97	66.59	99.47	141.1	162.27	162.8	252.75	179.0	330.74	203.2
30.15	69.29	101.55	142.0	162.59	162.0	255.15	179.4	330.87	195.5
31.30	71.85	103.61	143.0	163.11	161.7	257.55	179.8	331.08	191.0
32.41	74.33	105.65	143.9	163.84	161.6	259.94	180.4	331.52	185.5
33.50	76.59	107.68	144.9	164.66	161.4	262.34	181.1	332.18	183.3
34.72	79.08	109.70	145.7	165.64	161.6	264.73	181.6	332.96	182.3
36.08	81.73	111.70	146.7	166.76	161.8	267.13	182.0	333.80	181.8
37.37	84.12	113.75	147.5	168.02	161.9	269.52	182.6	334.70	181.5
38.59	86.35	115.85	148.4	169.42	162.1	271.91	183.0	336.69	181.3
39.79	88.43	117.94	149.3	171.26	162.4	274.30	183.6	339.03	180.6
40.99	90.45	120.01	150.2	173.46	162.8	276.69	184.1	340.65	180.5
42.20	92.39	122.08	151.0	175.66	163.2	279.14	184.7	342.52	180.4
43.42	94.39	124.13	151.9	177.91	163.6	281.64	185.3	344.62	180.4
44.68	96.32	126.18	152.8	180.21	164.0	284.14	185.9	346.73	180.4
45.96	98.27	128.22	153.7	182.50	164.4	286.65	186.6	348.63	180.3
47.47	100.5	130.30	154.6	184.80	164.9	289.15	187.8	350.89	180.1
49.07	102.6	132.43	155.5	187.09	165.3	291.64	188.9	353.16	180.0
50.51	104.6	134.56	156.5	189.44	165.8	294.14	188.2	355.44	180.0
51.91	106.4	136.67	157.4	191.83	166.2	296.64	188.7	357.77	179.8
53.29	108.2	138.78	158.4	194.22	166.6	299.14	189.6	360.17	179.9
54.67	109.8	140.88	159.4	196.57	167.0	301.45	190.4	362.58	180.0
56.06	111.4	142.98	160.5	198.88	167.6	303.57	190.8	365.00	180.1
57.49	113.0	145.12	161.6	201.12	168.1	305.69	191.4		
58.96	114.5	147.31	162.8	203.30	168.4	307.81	192.1		
60.47	116.0	149.50	164.3	205.47	168.9	309.92	192.7		
62.02	117.4	151.00	165.3	207.64	169.4	311.03	193.1		

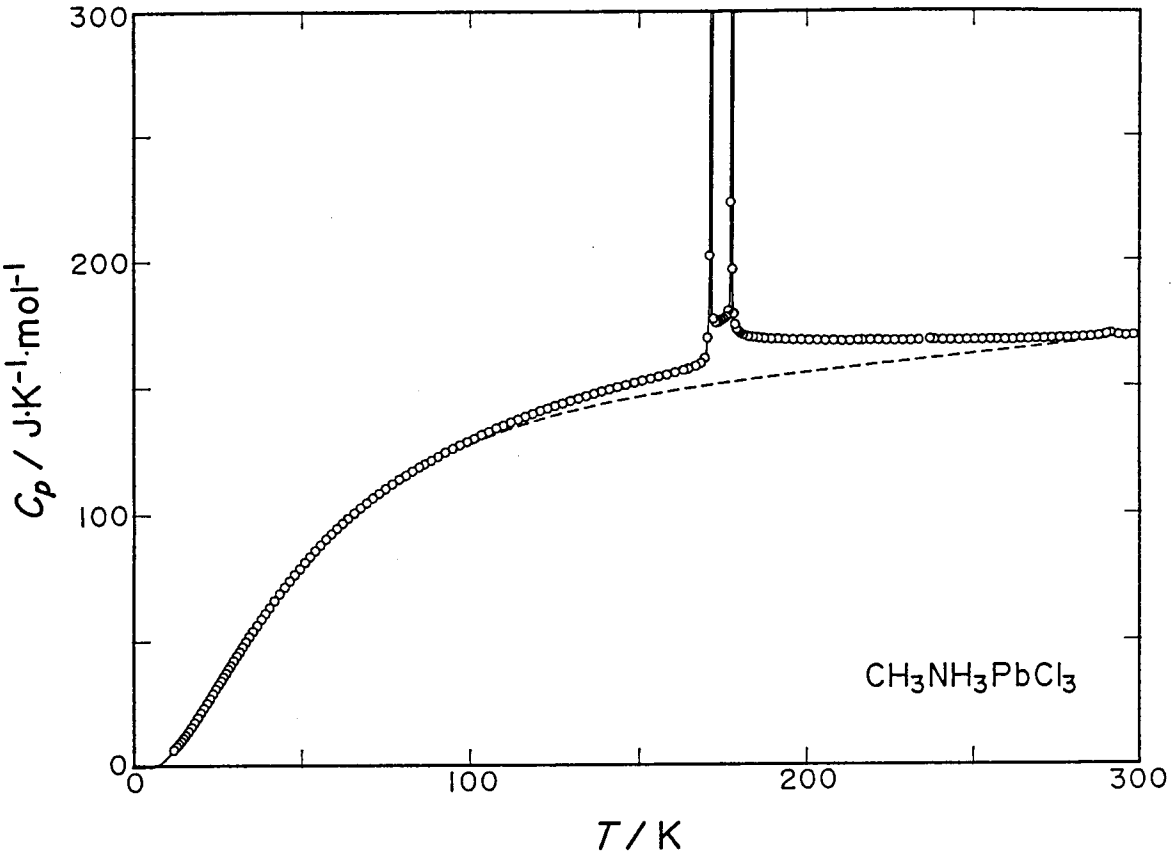

Fig. 3-4 Molar heat capacity of $CH_3NH_3PbCl_3$.

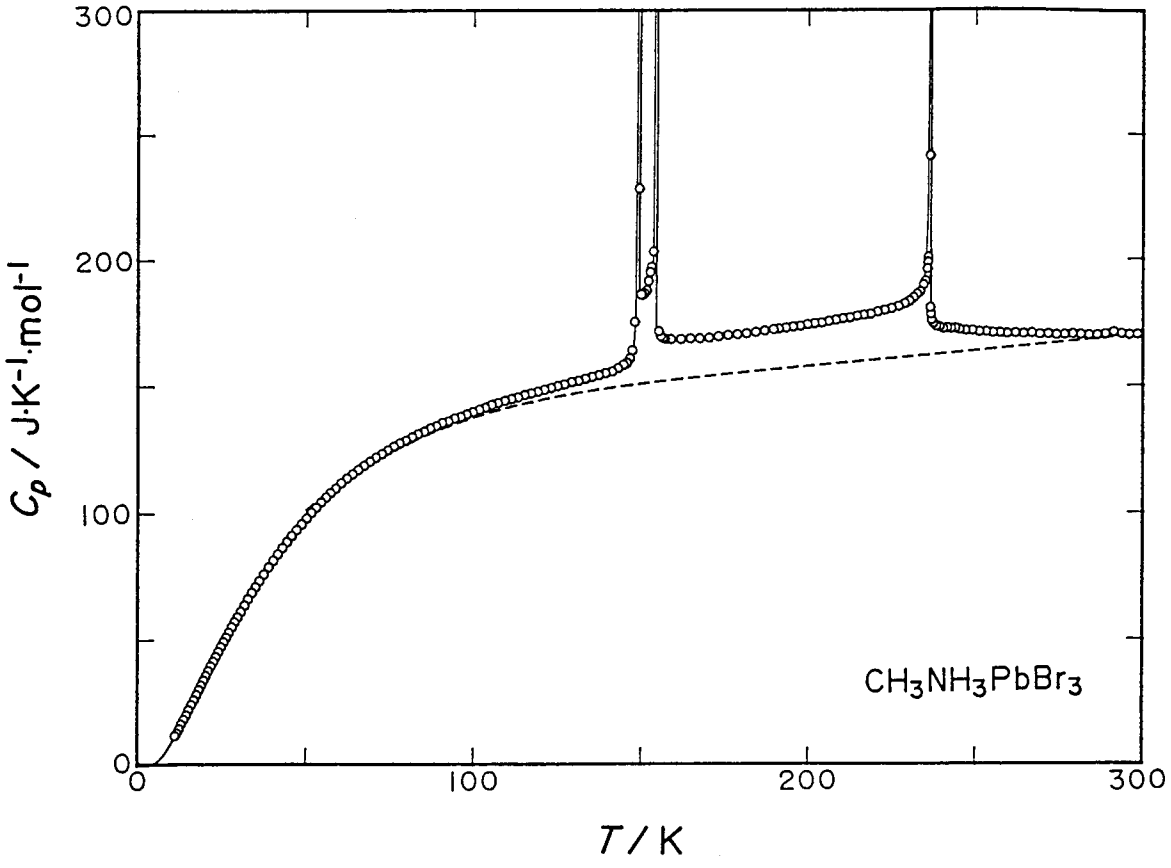

Fig. 3-5 Molar heat capacity of $CH_3NH_3PbBr_3$.

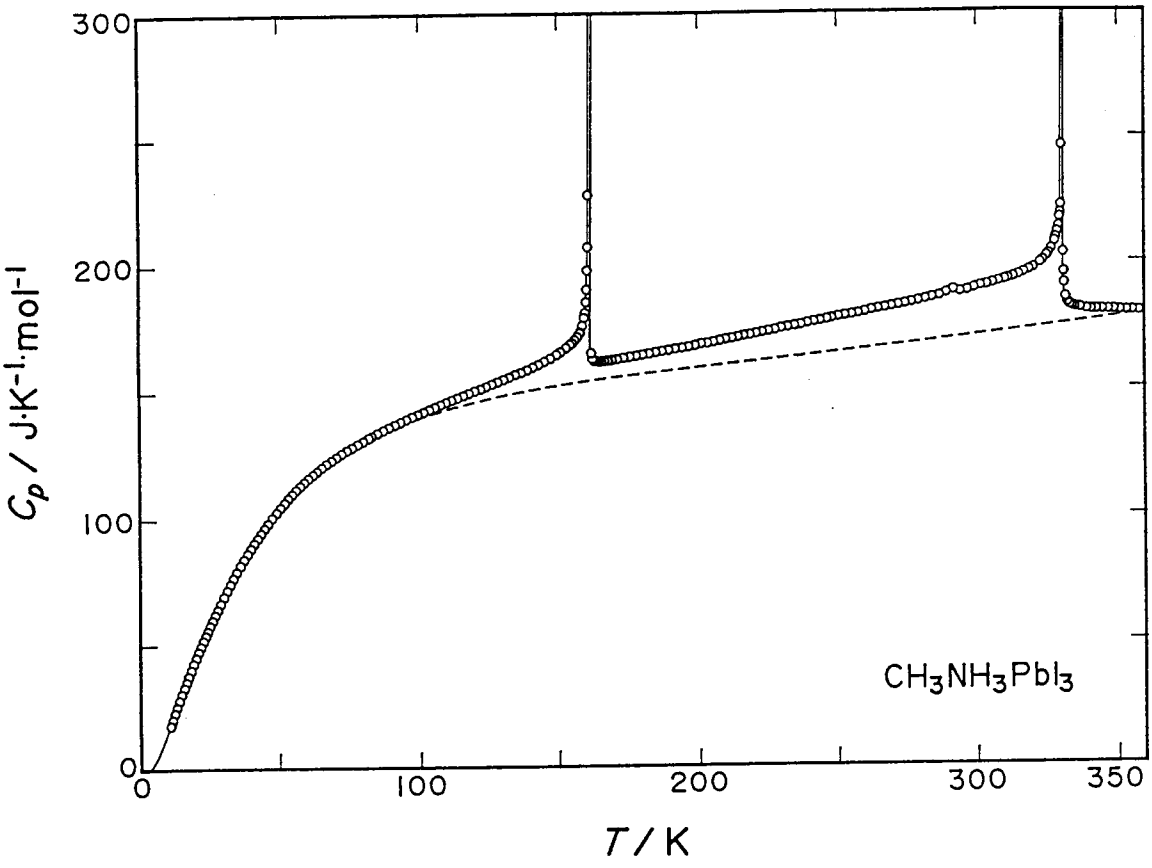

Fig. 3-6 Molar heat capacity of $CH_3NH_3PbI_3$.

Table 3-5 Thermodynamic functions of $CH_3NH_3PbCl_3$.

$\frac{T}{K}$	C_p / R	$(H-H_0)/RT$	S / R	$-(G-H_0)/RT$
10	(0.4544)	(0.1135)	(0.1512)	(0.03772)
20	2.542	0.7596	1.042	0.2827
30	5.113	1.781	2.557	0.7764
40	7.537	2.923	4.367	1.444
50	9.610	4.059	6.279	2.219
60	11.31	5.131	8.186	3.055
70	12.68	6.115	10.04	3.921
80	13.81	7.009	11.81	4.797
90	14.74	7.817	13.49	5.670
100	15.54	8.551	15.08	6.532
110	16.25	9.219	16.60	7.379
120	16.87	9.831	18.04	8.208
130	17.41	10.39	19.41	9.017
140	17.88	10.91	20.72	9.807
150	18.30	11.39	21.97	10.58
160	18.72	11.84	23.16	11.33
170	20.01	12.26	24.31	12.05
180	20.59	14.61	27.45	12.84
190	20.31	14.91	28.56	13.64
200	20.24	15.18	29.60	14.41
210	20.23	15.42	30.58	15.16
220	20.24	15.64	31.52	15.88
230	20.25	15.84	32.42	16.58
240	20.25	16.03	33.29	17.26
250	20.25	16.19	34.11	17.92
260	20.26	16.35	34.91	18.56
270	20.29	16.50	35.67	19.18
273.15	20.31	16.54	35.91	19.37
280	20.34	16.63	36.41	19.78
290	20.39	16.76	37.12	20.36
298.15	20.45	16.86	37.69	20.83
300	20.47	16.88	37.82	20.93

Table 3-6 Thermodynamic functions of $CH_3NH_3PbBr_3$.

$\frac{T}{K}$	C_p / R	$(H-H_0)/RT$	S / R	$-(G-H_0)/RT$
10	(0.9506)	(0.2151)	(0.2699)	(0.05477)
20	4.070	1.346	1.862	0.5163
30	7.142	2.777	4.107	1.330
40	9.713	4.201	6.527	2.326
50	11.78	5.518	8.925	3.407
60	13.40	6.702	11.22	4.520
70	14.61	7.749	13.38	5.633
80	15.52	8.666	15.40	6.729
90	16.26	9.470	17.27	7.797
100	16.85	10.18	19.01	8.832
110	17.38	10.81	20.64	9.833
120	17.84	11.38	22.17	10.80
130	18.24	11.89	23.62	11.73
140	18.71	12.36	24.99	12.63
150	22.41	13.87	27.38	13.50
160	20.28	14.58	29.01	14.42
170	20.35	14.92	30.24	15.32
180	20.52	15.23	31.41	16.18
190	20.73	15.51	32.52	17.01
200	20.97	15.78	33.59	17.81
210	21.22	16.03	34.62	18.59
220	21.54	16.27	35.61	19.34
230	22.07	16.51	36.58	20.07
240	20.83	16.78	37.55	20.78
250	20.66	16.93	38.40	21.47
260	20.55	17.08	39.21	22.13
270	20.51	17.20	39.98	22.78
273.15	20.50	17.24	40.22	22.98
280	20.48	17.32	40.73	23.41
290	20.44	17.43	41.45	24.02
298.15	20.49	17.51	42.01	24.50
300	20.52	17.53	42.14	24.61

Table 3-7 Thermodynamic functions of $CH_3NH_3PbI_3$.

$\frac{T}{K}$	C_p / R	$(H-H_0)/RT$	S / R	$-(G-H_0)/RT$
10	(1.863)	(0.5909)	(0.8044)	(0.2135)
20	5.317	2.094	3.159	1.065
30	8.299	3.682	5.900	2.217
40	10.68	5.146	8.626	3.481
50	12.51	6.443	11.21	4.771
60	13.89	7.575	13.62	6.049
70	14.92	8.553	15.84	7.292
80	15.72	9.401	17.89	8.490
90	16.39	10.14	19.78	9.641
100	17.00	10.80	21.54	10.74
110	17.55	11.39	23.19	11.80
120	18.06	11.92	24.74	12.82
130	18.58	12.41	26.20	13.79
140	19.12	12.87	27.60	14.73
150	19.80	13.31	28.94	15.63
160	22.15	13.76	30.26	16.50
170	19.51	15.81	33.25	17.44
180	19.72	16.03	34.37	18.35
190	19.95	16.23	35.45	19.22
200	20.18	16.42	36.48	20.06
210	20.43	16.60	37.47	20.86
220	20.69	16.78	38.42	21.64
230	20.94	16.96	39.35	22.39
240	21.20	17.13	40.24	23.11
250	21.46	17.30	41.12	23.82
260	21.71	17.46	41.96	24.50
270	21.97	17.62	42.79	25.16
273.15	22.05	17.68	43.04	25.37
280	22.23	17.78	43.59	25.81
290	22.52	17.94	44.37	26.43
298.15	22.77	18.07	45.00	26.93
300	22.83	18.10	45.14	27.04
310	23.18	18.26	45.90	27.64
320	23.71	18.42	46.64	28.22
330	27.82	18.60	47.40	28.79
340	21.71	18.76	48.11	29.35
350	21.67	18.85	48.74	29.89
360	21.63	18.92	49.35	30.43

vibrational freedom in $MAPbX_3$. Out of the 18 internal degrees of freedom for an MA ion, 17 fundamental vibrations were determined by infrared absorption spectroscopy, as shown in Table 3-1. The heat capacities of these vibrations were calculated by using the Einstein function. The remaining one is the torsional oscillation (*alias*, internal rotation, see below). The rotational motions of the MA ion about the C-N axis cannot be described by a harmonic potential, because the barriers hindering the motions are low. There are two such motions of an MA ion; *external* and *internal* hindered rotations, where the word *internal* means the independent reorientation of the CH_3 and the NH_3 groups and the word *external* means their in-phase reorientation. They are coupled together to form a complicated spectrum of the energy levels. However, they are approximated with two independent hindered rotations for the sake of simplicity of the calculation. Assuming that the MA ion has three-fold symmetry in the crystal field, we write the potential as

$$v = \frac{1}{2} v_0 (1 - \cos 3\theta), \tag{3-3}$$

where v_0 is the potential barrier and θ the angle of rotation about the C-N axis. The corresponding Hamiltonian is

$$H = - \frac{\hbar^2}{2I} \frac{\partial^2}{\partial \theta^2} + v, \tag{3-4}$$

where I is the reduced moment of inertia. Thus, the wave-equation is given by

$$[-\frac{\hbar^2}{2I}\frac{\partial^2}{\partial\theta^2} + \frac{V_0}{2}(1 - \cos 3\theta)]\psi(\theta) = E\,\psi(\theta). \qquad (3\text{-}5)$$

Here $\psi(\theta)$ and E are the eigenfunction and its eigenvalues. This can be related to the standard form of the Mathieu equation,

$$\frac{d^2M(x)}{dx^2} + (b - s\cos^2 x)\,M(x) = 0, \qquad (3\text{-}6)$$

for which the eigenvalues have been tabulated [14].

The moment of inertia I was calculated from the mass of the proton, and the known geometry of the MA ion. The calculated values are 2.501×10^{-47} kg m^2 for the internal rotation and 10.04×10^{-47} kg m^2 for the external rotation, respectively. Numerical value of V_0 was obtained from the activation energy E_a corrected for the zero-point motion. The barrier height to the internal rotation has been estimated to be 8.0 kJ mol^{-1} [15]. For the external rotation, the barriers obtained by Xu *et al.* by NMR measurement [6] were used. The barrier height derived from the IR line width could have been used but the NMR values were employed because the theoretical background is better established for the NMR T_1 than the IR line width. (However, there was only small difference between the resulting base lines calculated from the different barrier heights. For $MAPbCl_3$, the entropy change of the 171.5 K transition was 14.6 J K^{-1} mol^{-1} from the NMR barrier height and 15.2 J K^{-1} mol^{-1} from IR.) Energy levels of the hindered rotations were calculated using the tabulated eigenvalues of the Mathieu equation [14].

There remain 17 vibrational modes to be taken into account. They are 14 optical modes (2 librational modes of the MA ion and 12 translational modes) and 3 acoustic modes. Contributions from these modes to the heat capacities were approximated by the Debye and Einstein functions. The normal heat capacity C_p(normal) was thus decomposed as follows:

$$C_p(\text{normal}) = C(\text{internal vib., 17, } E) + C(\text{hindered rot., 2, } M) + C(\text{libration, 2, } E) + C(\text{acoustic, 3, } D) + \sum_{i=1}^{4} C(\text{optical, 3, } E_i) + AC_p^2T. \qquad (3\text{-}7)$$

In this expression, each term except the last is labeled by the respective mode, the corresponding number of degrees of freedom, and the model function used for the calculation (E = Einstein approximation, D = Debye approximation and M = the sum over states of the Mathieu levels). In the actual calculation, a better fitting was obtained when one of the Einstein function of the weight 3 was replaced with a Debye function. Two Einstein parameters each with the degeneracy of 3 converged to approximately equal values. They were combined to one Einstein temperature with the degeneracy of 6. Thus, the model heat capacity function contained two Debye temperatures θ_D, three Einstein temperatures θ_E, and the C_p - C_V correction coefficient A as the parameters to be determined by the least-squares method.

In the actual application of the interpolation function (3-7), one is often left with an arbitrariness as to the temperature intervals of the experimental data which are to be included in the least-squares fitting. This is particularly true below the

transition temperature where gradual increase of the heat capacity is appreciable. This situation can be coped with by adding to the interpolation function a term representing the gradual increase of the heat capacity below T_{trs}. For this purpose, the heat capacity of the spin 1/2 Ising model system solved by the mean field approximation was used. The heat capacity of the Ising system cannot be given in a closed form even in this simplest approximation. Therefore the self-consistency relation was solved numerically for the order parameter. The heat capacity is given by the temperature derivative of the squared order parameter, which was also evaluated numerically. The resulting heat capacity was expressed as a universal function of the temperature as follows:

$$\frac{C(\mathrm{Ising})}{R} = 6.13\ x - 5.04\ x^2 + 18.7\ x^3$$

$$x = \exp(-1.3899\ \frac{T_0}{T}), \qquad (3\text{-}8)$$

where T_0 is the transition temperature in the mean field approximation. The numerical factors in Eq. (3-8) were determined by the least-squares method to best reproduce the computed mean field heat capacity. The heat capacity function (3-8) was added to the model function, Eq. (3-7), for $T < T_{trs}$ of the lowest-temperature transition. For $T > T_{trs}$ Eq. (3-7) was used as it stands. By this modification, the experimental data closer to T_{trs} could be included in the least-squares calculation of the base line than was previously possible. The parameter values

thus determined are given in Table 3-8 together with the temperature regions of the heat capacity data used in the fitting.

3.3.3 Enthalpy and Entropy of Transition

The differences between the experimental and normal heat capacities are shown in Figs. 3-7, 3-8 and 3-9 for $MAPbCl_3$, $MAPbBr_3$ and $MAPbI_3$, respectively. Integration of the excess heat capacity and the addition of the discontinuous part at the phase transition gave the transition enthalpy and entropy. They are given in Table 3-9. Since the phase transitions were overlapped, as shown in Figs. 3-7, 3-8 and 3-9, they were divided at the temperatures where the excess heat capacities took the minimum values. The entropy values indicate that all the phase transitions in these compounds are of order-disorder type because they are of the order of R ln n with n in the range 2～10. They are shown graphically in Fig. 3-10 from which one sees that the high temperature limiting values of the transition entropies in these compounds are close to one another. It is concluded that these compounds have the same extent of disorder in the cubic phase. Figures 3-11, 3-12 and 3-13 show temperature dependence of the entropy of transition in $MAPbCl_3$, $MAPbBr_3$ and $MAPbI_3$, respectively. It should be noted that the discontinuous parts of the transition entropies of the highest temperature transitions in $MAPbBr_3$ and $MAPbI_3$ are much smaller than those of the other transitions. For $MAPbBr_3$, it is 0.3 J K^{-1} mol^{-1} which is only 3.7 % of the transition entropy (8.2 J K^{-1} mol^{-1}), compared with the discontinuities 9.0 J K^{-1} mol^{-1} (80 %) and 2.6 J K^{-1} mol^{-1} (62 %) of the two lower temperature transitions. For $MAPbI_3$, the corre-

Table 3-8 Temperature regions of the heat capacity data used in the fitting and optimized parameters of $CH_3NH_3PbX_3$ (X = Cl, Br, I).

	$CH_3NH_3PbCl_3$	$CH_3NH_3PbBr_3$	$CH_3NH_3PbI_3$
Temperature region	13 - 115 K	13 - 100 K	13 - 105 K
used in the fitting	295 - 300 K	295 - 300 K	360 - 365 K
Parameters optimized			
$\theta_D(3)$ / K	81.7	107.0	121.9
$\theta_D(3)$ / K	224.6	194.1	90.0
$\theta_E(2)$ / K	318.9	41.3	25.0
$\theta_E(3)$ / K	86.2	67.3	63.4
$\theta_E(6)$ / K	165.7	163.2	168.4
$A \times 10^{-7}$ / $molJ^{-1}$	8.86	8.20	6.48
T_{trs} / K	231.4	229.7	243.2

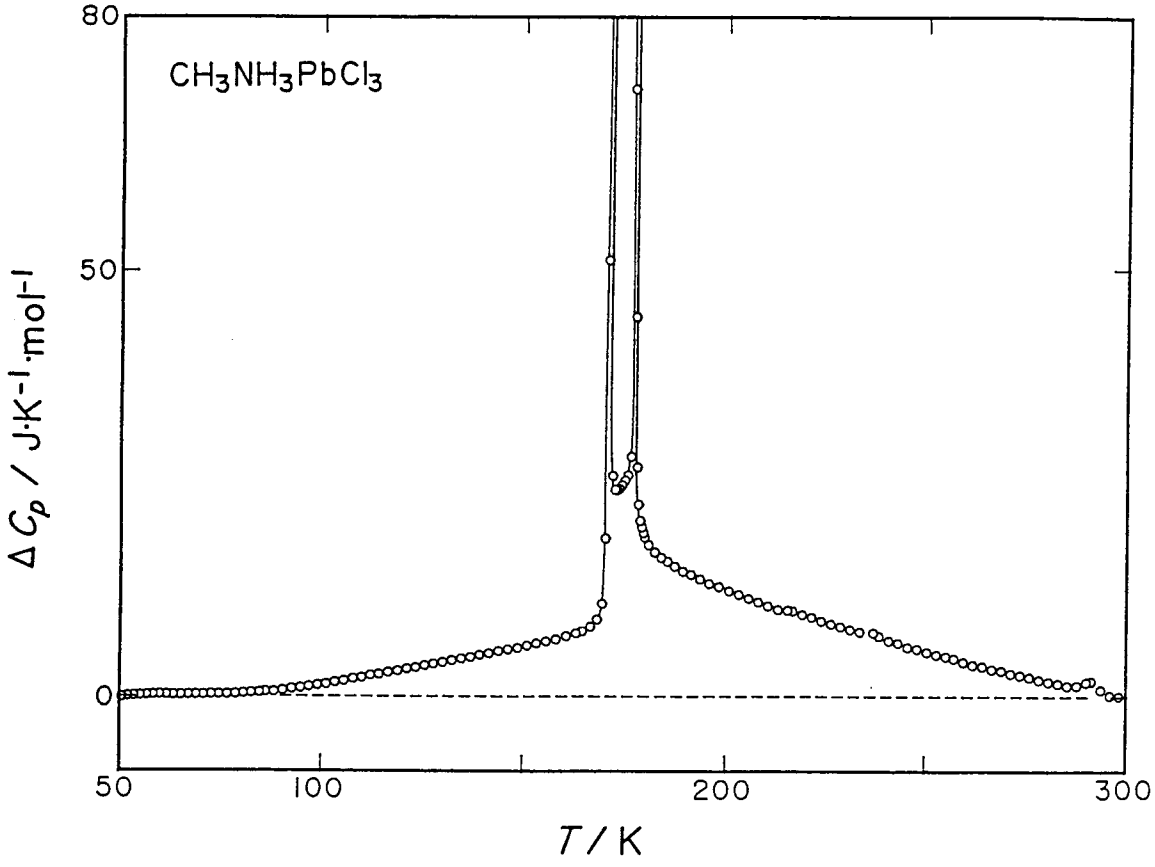

Fig. 3-7 Excess heat capacity of $CH_3NH_3PbCl_3$.

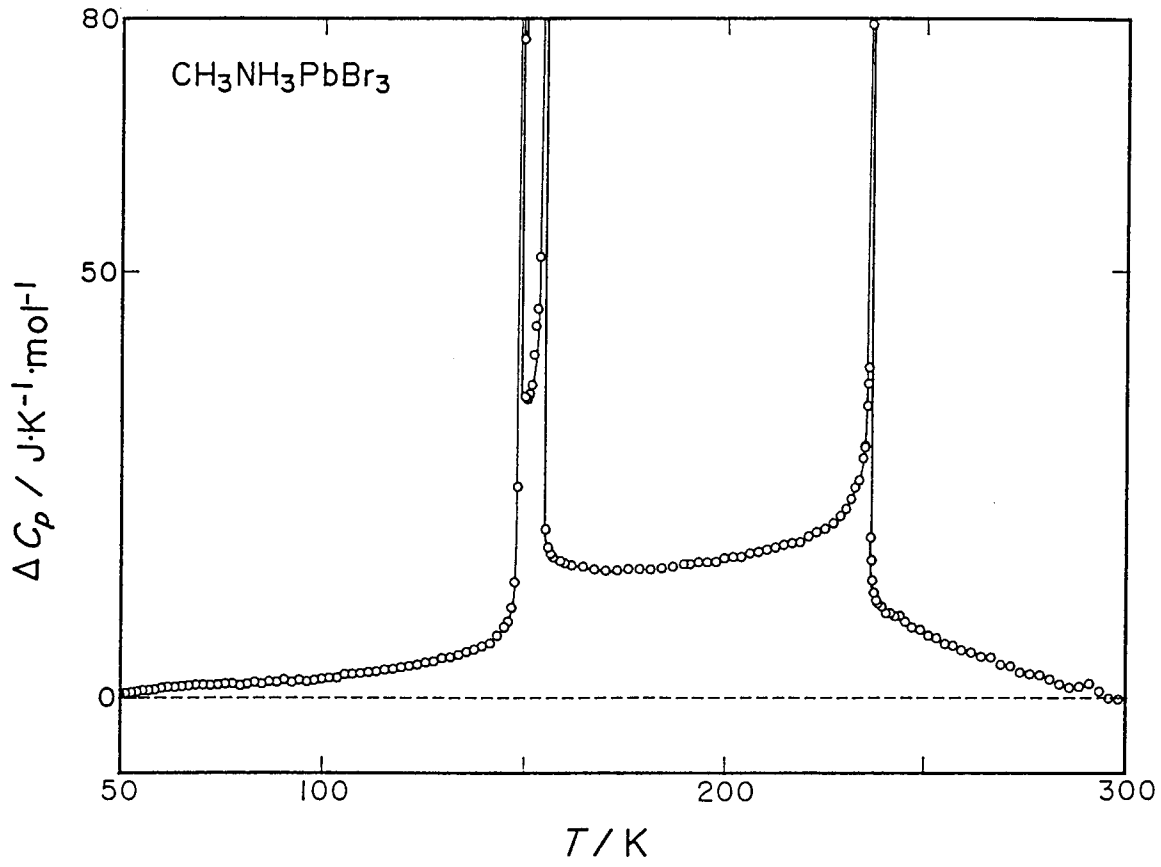

Fig. 3-8 Excess heat capacity of $CH_3NH_3PbBr_3$.

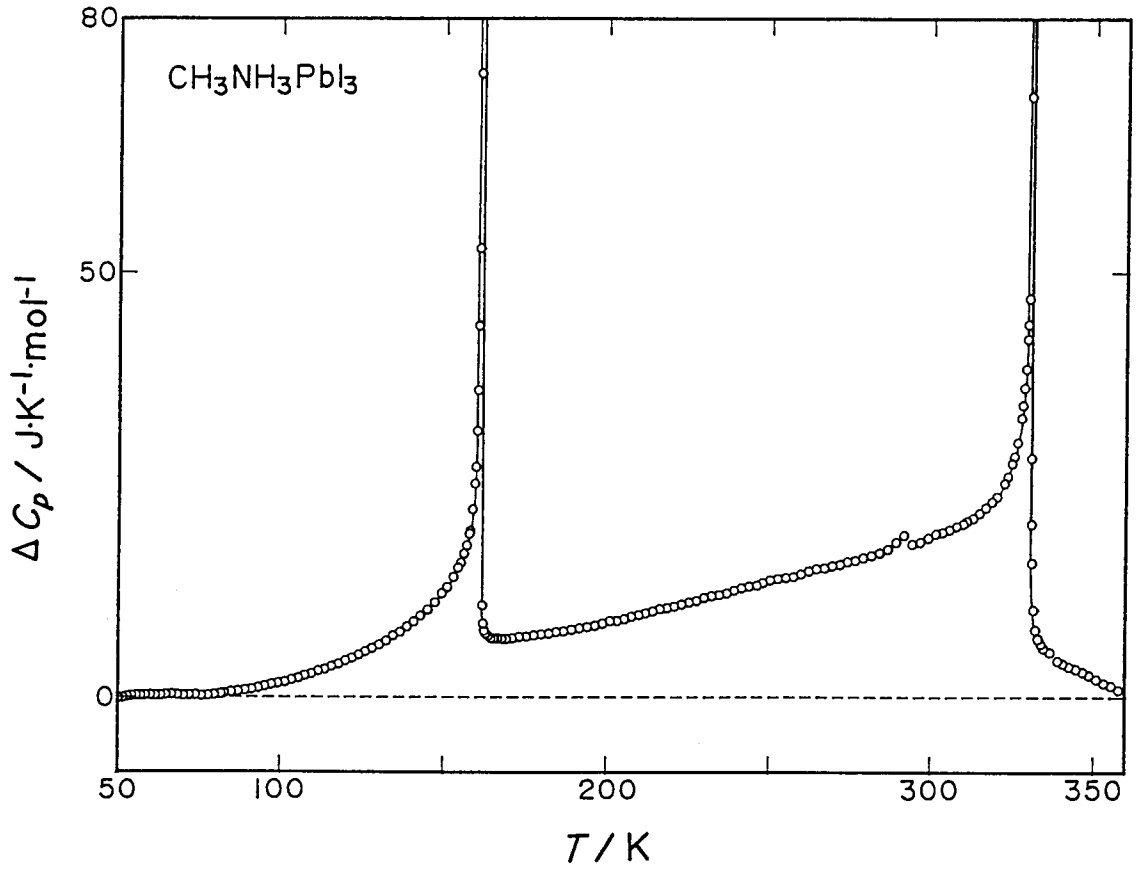

Fig. 3-9 Excess heat capacity of $CH_3NH_3PbI_3$.

Table 3-9 Temperatures, enthalpies and entropies of the phase transitions of $CH_3NH_3PbX_3$ (X = Cl, Br, I).

	T_{trs} / K	$\Delta_{trs}H$ / kJ mol^{-1}	$\Delta_{trs}S$ / J K^{-1}mol^{-1}
$CH_3NH_3PbCl_3$	171.5	2.40	14.6 (R ln 5.8)
	177.2	1.92	10.0 (R ln 3.3)
$CH_3NH_3PbBr_3$	148.8	1.59	11.2 (R ln 3.8)
	154.0	0.62	4.1 (R ln 1.7)
	236.3	1.71	8.2 (R ln 2.7)
$CH_3NH_3PbI_3$	161.4	2.98	19.0 (R ln 9.8)
	330.4	2.58	9.7 (R ln 3.2)

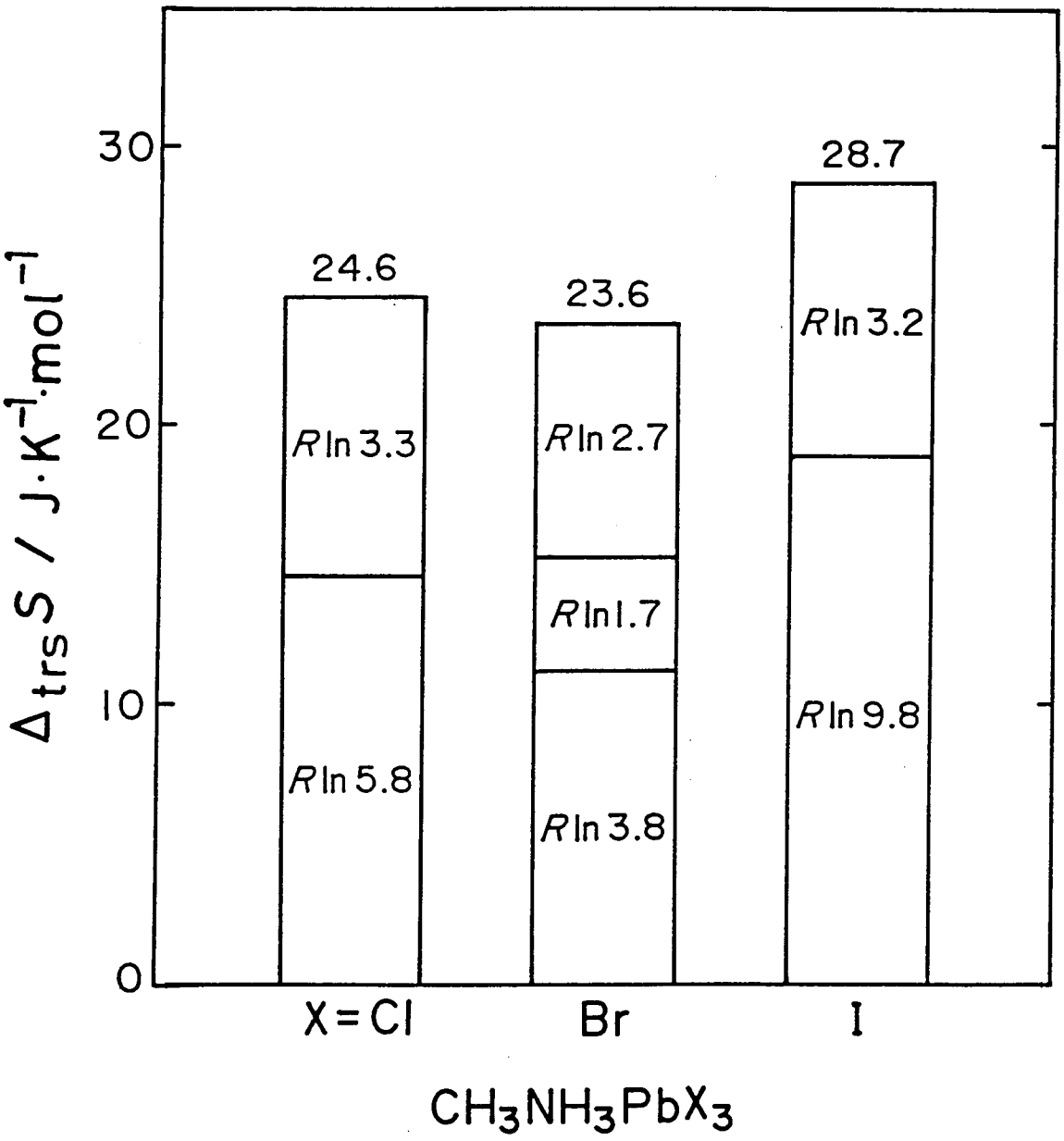

Fig. 3-10 Transition entropy of $CH_3NH_3PbX_3$ (X = Cl, Br, I).

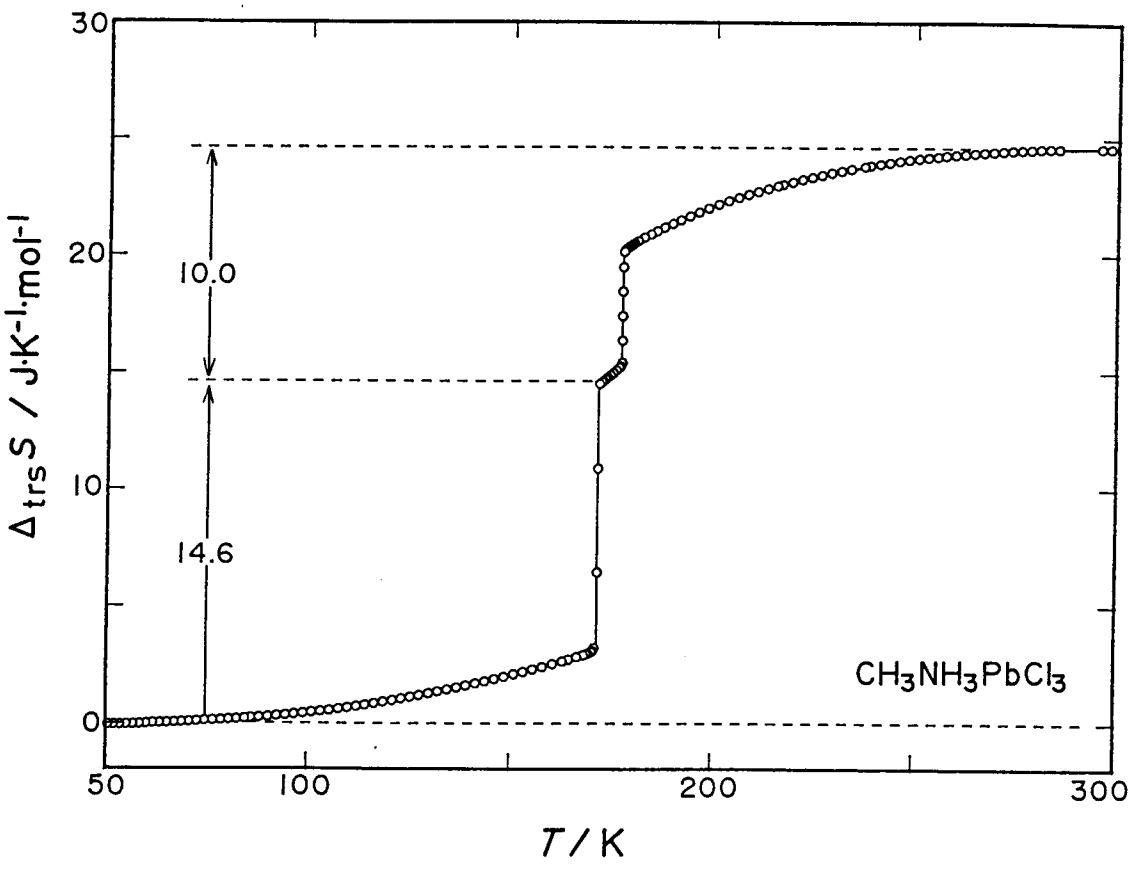

Fig. 3-11 Accumulated transition entropy of $CH_3NH_3PbCl_3$ as a function of temperature.

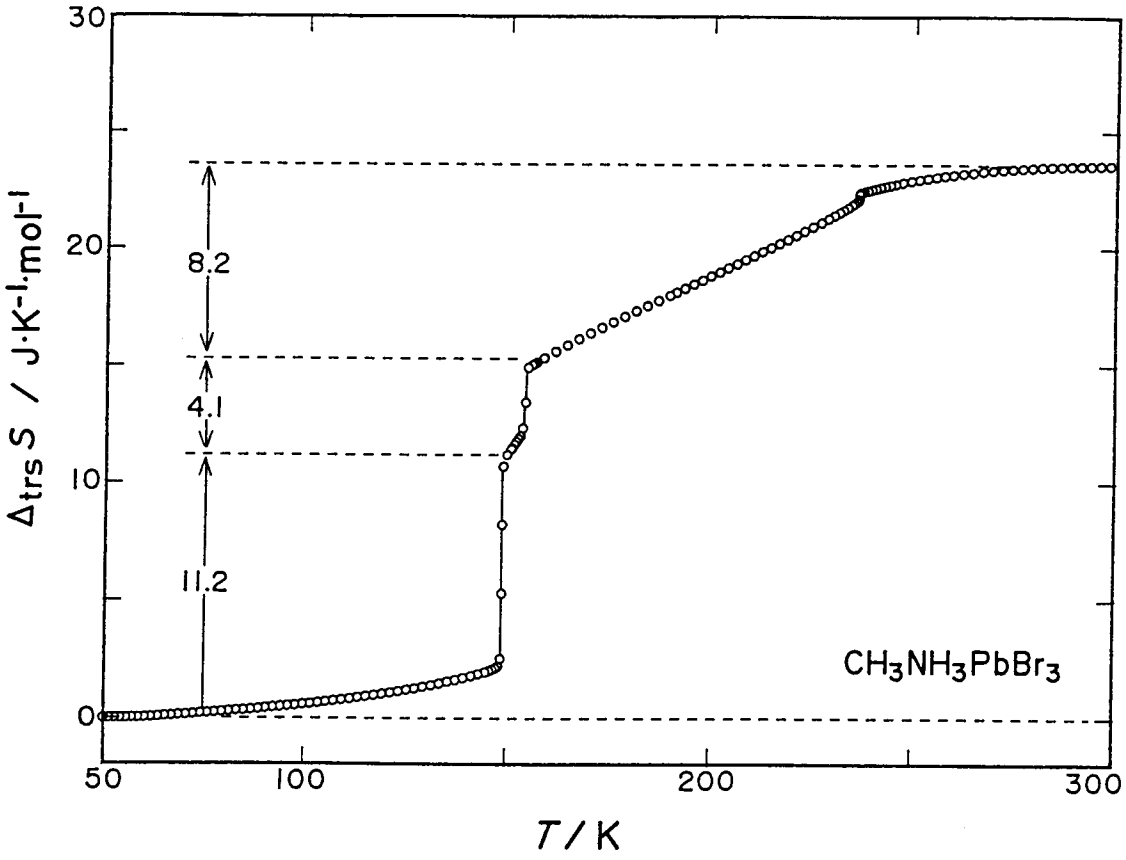

Fig. 3-12 Accumulated transition entropy of $CH_3NH_3PbBr_3$ as a function of temperature.

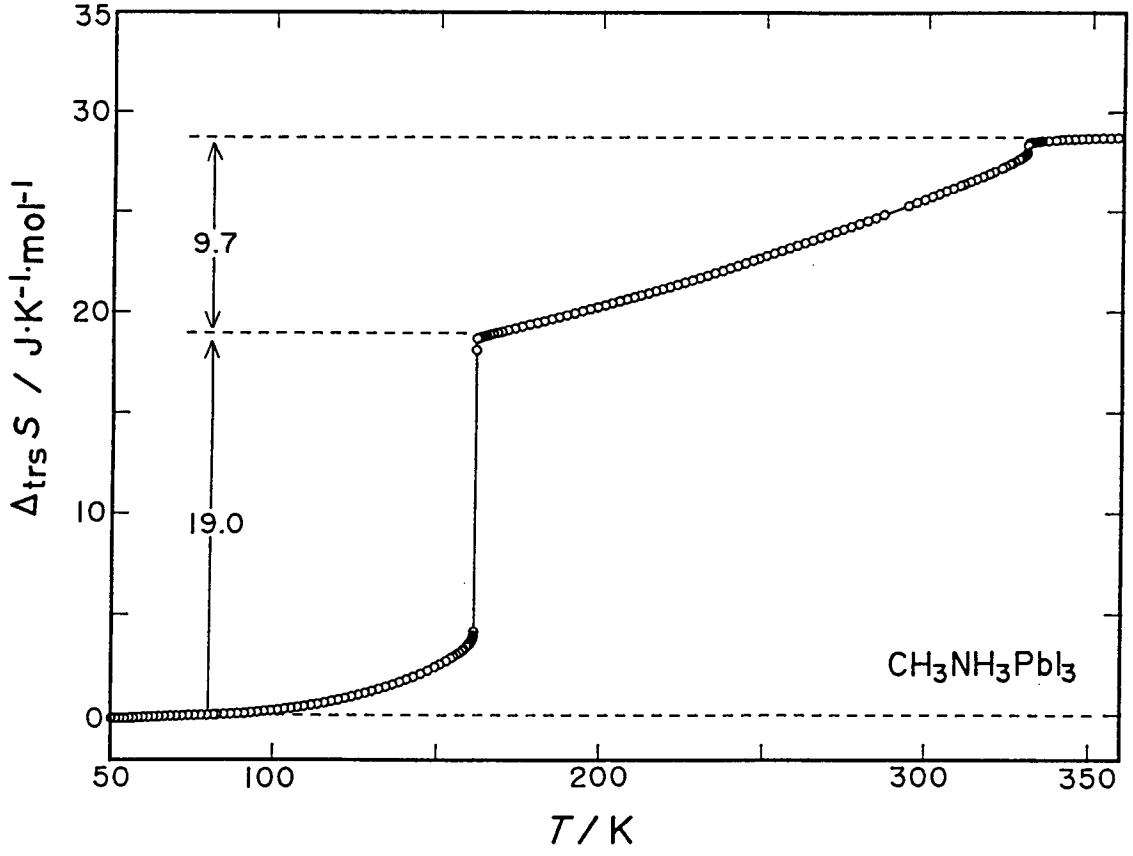

Fig. 3-13 Accumulated transition entropy of $CH_3NH_3PbI_3$ as a function of temperature.

sponding entropy 0.5 J K^{-1} mol^{-1} (5.5 %) is again a very small value compared with 14.8 J K^{-1} mol^{-1} (78 %) of the lower temperature transition. As shown in Figs. 3-11 and 3-12, the excess heat capacities of the tetragonal I-cubic transitions extend over a wide temperature range below the transition temperature. These results indicate that the tetragonal I-cubic transitions have a character of higher order transitions, even though they are first order transitions by the thermodynamic definition.

3.3.4 Mechanism of the Phase Transitions

In the cubic phase, the MA ion lies at the center of the regular cube formed by eight Pb^{2+} ions. This requires the MA ion to be disordered in a certain way. Several different sets of orientations are possible for an MA ion, each of which satisfies the cubic site symmetry. They are shown schematically in Fig. 3-14. Arrows in the cube indicate the orientations of the C-N axis of the MA ion. The MA ion points to the face centers (along the four-fold axes) in (A), the middle of the cube edge (along the two-fold axes) in (B) and the cube corner (along the three-fold axes) in (C). There are three of four-fold axes, six of two-fold axes and four of three-fold axes in the cube. If the MA ion is disordered with respect to head and tail, the number of equivalent orientations of the MA ion is (A) 6, (B) 12 and (C) 8, respectively. Since the MA ion possessing three-fold symmetry lies (A) on the four-fold axes and (B) on the two-fold axes, it must be disordered around the C-N axis as well. Therefore the MA ion has at least (A) four and (B) two equivalent orientations around the C-N axis. The number of equivalent orientations of

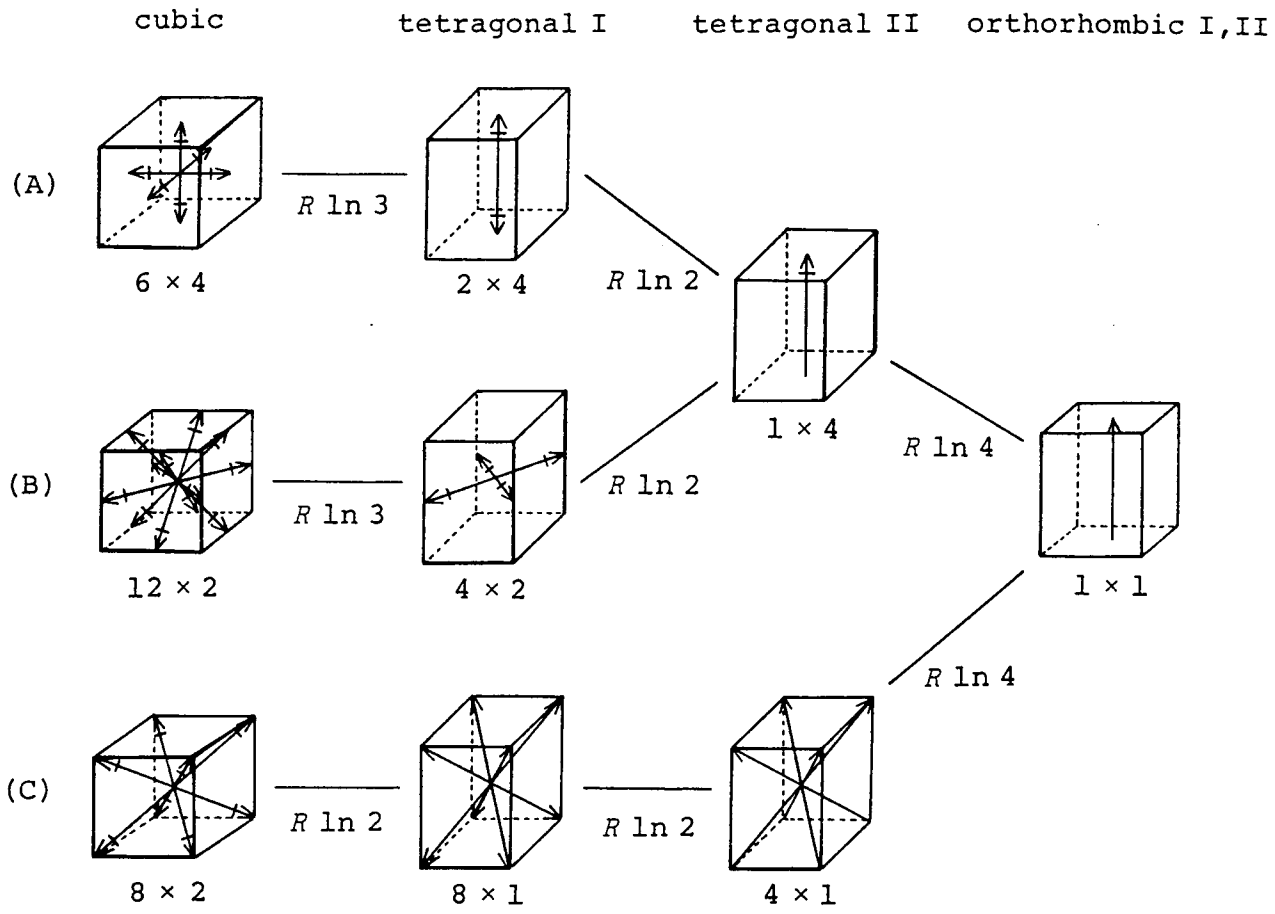

Fig. 3-14 Possible orientations and ordering processes of a $CH_3NH_3^+$ ion. Arrows indicate the orientations of a C-N axis.

↟: disordered around the C-N axis.

↑: ordered around the C-N axis.

the MA ion is (A) 6 x 4 = 24 and (B) 12 x 2 = 24, respectively. Assuming that the MA ion is completely ordered in the orthorhombic phase, the entropy change associated with the orientational ordering is R ln 24 = 26.4 J K^{-1} mol^{-1} in both cases. It is close to the experimental values 24～29 J K^{-1} mol^{-1}. In (C) which was suggested by Poglitsch and Weber[2], it is not required from the symmetry that the MA ion be disordered around the C-N axis because the symmetries of the site and the MA ion are the same. However the entropy of this orientational disorder (R ln 8) is much smaller than the experimental value. Therefore one must assume that the MA ion is disordered around the axis also in this model, even though it is not forced by the symmetry. If the hydrogen atoms are on the general positions, the MA ion has two equivalent orientations around the C-N axis. The number of equivalent orientations of the MA ion is 8 x 2 = 16. The entropy change R ln 16 = 23.1 J K^{-1} mol^{-1} is also close to the experimental values. In the following, the mechanisms of the phase transitions of the three compounds are discussed based on the above three types (A, B and C) of the orientational disorder.

$MAPbBr_3$

The experimental values of transition entropies, R ln 2.7, R ln 1.7 and R ln 3.8 for the three phase transitions in the decreasing order of temperature, are very close to R ln 3, R ln 2 and R ln 4, respectively.

In the model (A), the MA ion has six equivalent orientations along the cube edges. Assuming that the orientation of the MA ion is restricted to two of them along the four-fold axis in the tetragonal I phase and that the head-to-tail disorder of the MA

ion is further removed in the tetragonal II phase, the entropy change associated with each ordering is expected to be R ln 3 and R ln 2, respectively. If the remaining disorder of the MA ion around the C-N axis is removed in the orthorhombic II phase, the entropy change associated with it should be R ln 4.

In the model (B), the MA ion has twelve equivalent orientations of the C-N axis. Assuming that four orientations in which the C-N axis lies normal to the four-fold axis of the tetragonal cell are allowed in the tetragonal I phase, the entropy associated with the cubic-tetragonal I transition will be R ln 3. However there is no further ordered pattern of the tetragonal symmetry which can be derived from this partially ordered model and which one may identify with the tetragonal II phase. If the MA ion chooses another orientation along the four-fold axis of the tetragonal lattice in the tetragonal II phase, which is the same as (A), the tetragonal symmetry is of course satisfied. Considering that the equivalent orientations around the C-N axis change from two to four, the entropy change associated with it is R ln (4 x 2) - R ln (1 x 4) = R ln 2. The tetragonal I-tetragonal II transition is of the first order in this model whereas it can be of a higher order in the model (A).

In the model (C), the MA ion has eight equivalent orientations along the body diagonals of the cube and two equivalent orientations around each body diagonal. If one assumes that the two equivalent orientations around the C-N axis is removed in the tetragonal I phase, the expected entropy change of this orientational ordering, R ln 2, is close to the experimental value. The orientational disorder of the MA ion is preserved through the

cubic-tetragonal I transition in this model as originally suggested by Poglitsch and Weber. If the head-to-tail disorder of the MA ion is removed in the tetragonal II phase and the fourfold disorder of the orientation of the C-N axis is removed in the orthorhombic II phase, the entropy changes associated with the sequence of ordering are R ln 2 and R ln 4.

It should be pointed out that the site symmetry of the MA ion in the tetragonal II phase of the above models is 4mm rather than 4/mmm of the space group P4/mmm. The latter requires the head-to-tail disorder of the C-N axis. However, the entropies of transition support the 4mm models. It was also suggested in the ^{2}H NMR study [4].

$MAPbI_3$

The highest temperature phase of this crystal has the same symmetry as $MAPbBr_3$ and the symmetry of the tetragonal phase is the same as that of the high temperature tetragonal phase of $MAPbBr_3$. The experimental entropy of tetragonal I-cubic transition is 9.7 J K^{-1} mol^{-1} (R ln 3.2), which agrees well with the model entropy of tetragonal I-cubic transition of $MAPbBr_3$. The structure of the orthorhombic phase is also the same as that of $MAPbBr_3$. Since $MAPbBr_3$ has one more phase in the temperature range between the orthorhombic II and the tetragonal I phases, the entropy of orthorhombic II-tetragonal I transition in $MAPbI_3$ should be compared with the sum of the entropies of orthorhombic II-tetragonal II transition and tetragonal II-tetragonal I transition in $MAPbBr_3$. The sum of the model entropies of these transitions is R ln 8 = 17.3 J K^{-1} mol^{-1}. The experimental value is 19.0 J K^{-1} mol^{-1} (R ln 9.8) in good

agreement with the model entropy.

$MAPbCl_3$

The tetragonal phase of $MAPbCl_3$ has the same symmetry as the low temperature tetragonal phase of $MAPbBr_3$. Therefore the experimental entropy of tetragonal II-cubic transition of $MAPbCl_3$ is expected to be close to the sum of the entropies of tetragonal II-tetragonal I and tetragonal I-cubic transitions of $MAPbBr_3$. The sum of these model entropies is R ln 6. The experimental entropy is 10.0 J K^{-1} mol^{-1} (R ln 3.3), which is rather closer to that of tetragonal I-cubic transition than to the sum of the two entropies. Poglitsch and Weber suggested the persistence of the head-to-tail disorder of the MA ion in the orthorhombic phase [2]. However, no transitions have been observed between 13 K (the lowest temperature of the measurement) and 171.5 K (the temperature of orthorhombic I-tetragonal II transition) in $MAPbCl_3$. This fact indicates strongly that the head-to-tail disorder has already been removed. The entropy of orthorhombic I-tetragonal II transition is 14.6 J K^{-1} mol^{-1}. One expects the same entropy change for this transition as for the orthorhombic II-tetragonal II transition of the $MAPbBr_3$ crystal. However, this is not the case; the latter amounts to 11.2 J K^{-1} mol^{-1}. The sum of the transition entropies of $MAPbCl_3$ is very close to that of $MAPbBr_3$, even though there is no obvious correspondence between the steps by which the disordering proceeds in the two crystals.

In contrast to ABO_3-type oxides and ABF_3-type fluorides, only a few ABX_3-type halides are known to crystallize in the perovskite structures. $CsPbCl_3$ takes the cubic perovskite struc-

ture at high temperature and undergoes three successive phase transitions at 310, 315 and 320 K [16-19]. The phase transitions have been accounted for by the soft mode concept [20]. The small entropies, 1.0 J K^{-1} mol^{-1} for the transition at 320 K and 1.5 J K^{-1} mol^{-1} for the sum of the entropies of the transitions at 310 and 315 K [21] are characteristic of displacive transitions. A similar amount of vibrational entropy may be involved in the transition entropies discussed here. However, it is a tiny correction to the entropy arising from the orientational disorder in $MAPbX_3$. The entropies of the tetragonal-cubic transition in the perovskite crystals $RbCaF_3$ and $TlCdF_3$ [22] are also the same order of magnitude as those of $CsPbCl_3$. The three disordered models concerning the orientation of the MA ion in the cubic phase of $MAPbX_3$ crystals cannot be distinguished from the entropy consideration alone. There is little distinction among them in the preference of packing, because MA ions and halogen ions form the cubic closest packing in the cubic phase.

3.4 Dielectric Permittivity

3.4.1 Temperature Dependence of the Dielectric Permittivity

Temperature dependence of the real part of the dielectric permittivity is shown in Figs. 3-15, 3-16 and 3-17 for $MAPbCl_3$, $MAPbBr_3$ and $MAPbI_3$, respectively. Since no frequency dependence was found except in the lowest temperature phases of $MAPbBr_3$ and $MAPbI_3$ (see below), only the 1 kHz data are shown. Symbols ● and ○ denote the data obtained on cooling and heating, respectively. Arrows in the figures indicate the transition temperatures determined by the heat capacity measurement (see Table 3-9

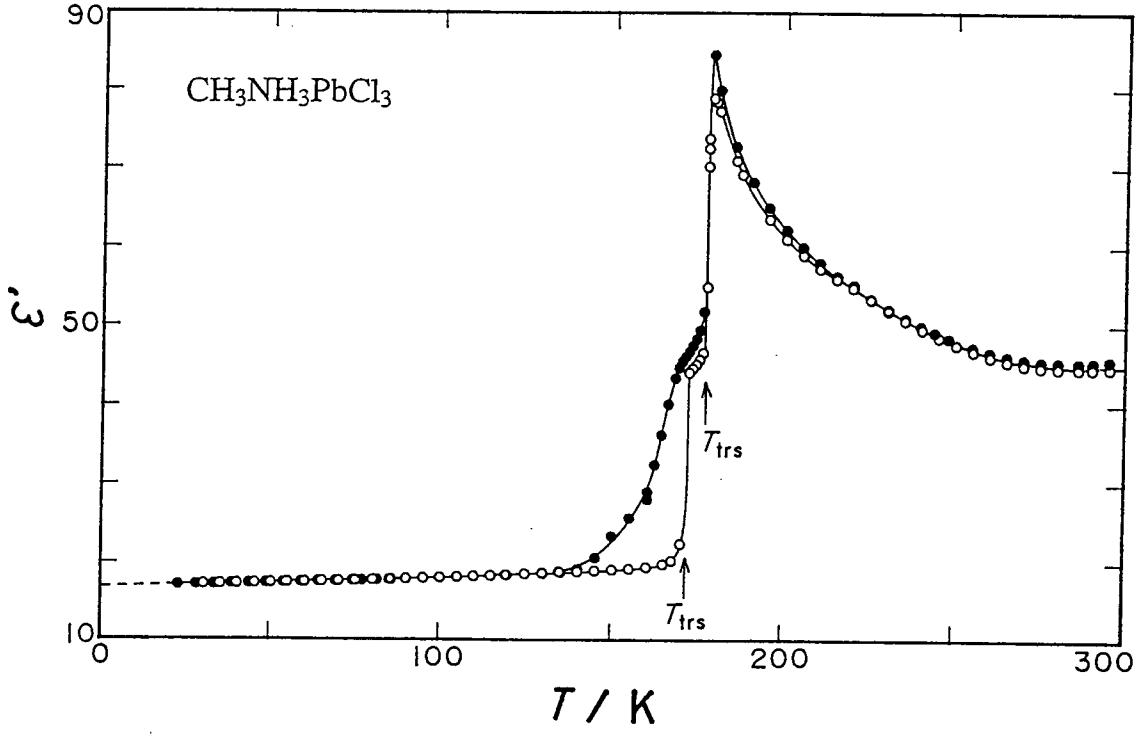

Fig. 3-15 Temperature dependence of the real part of the dielectric permittivity of $CH_3NH_3PbCl_3$ taken at 1 kHz in heating (open symbols) and cooling (closed symbols).

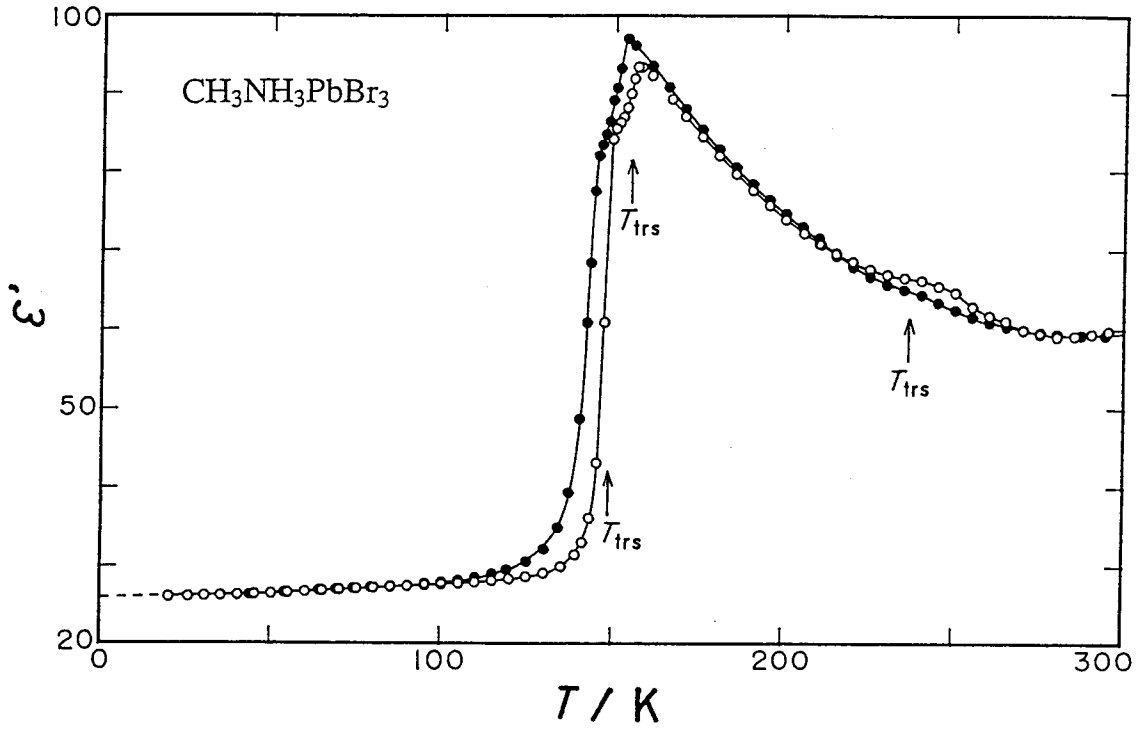

Fig. 3-16 Temperature dependence of the real part of the dielectric permittivity of $CH_3NH_3PbBr_3$ taken at 1 kHz in heating (open symbols) and cooling (closed symbols).

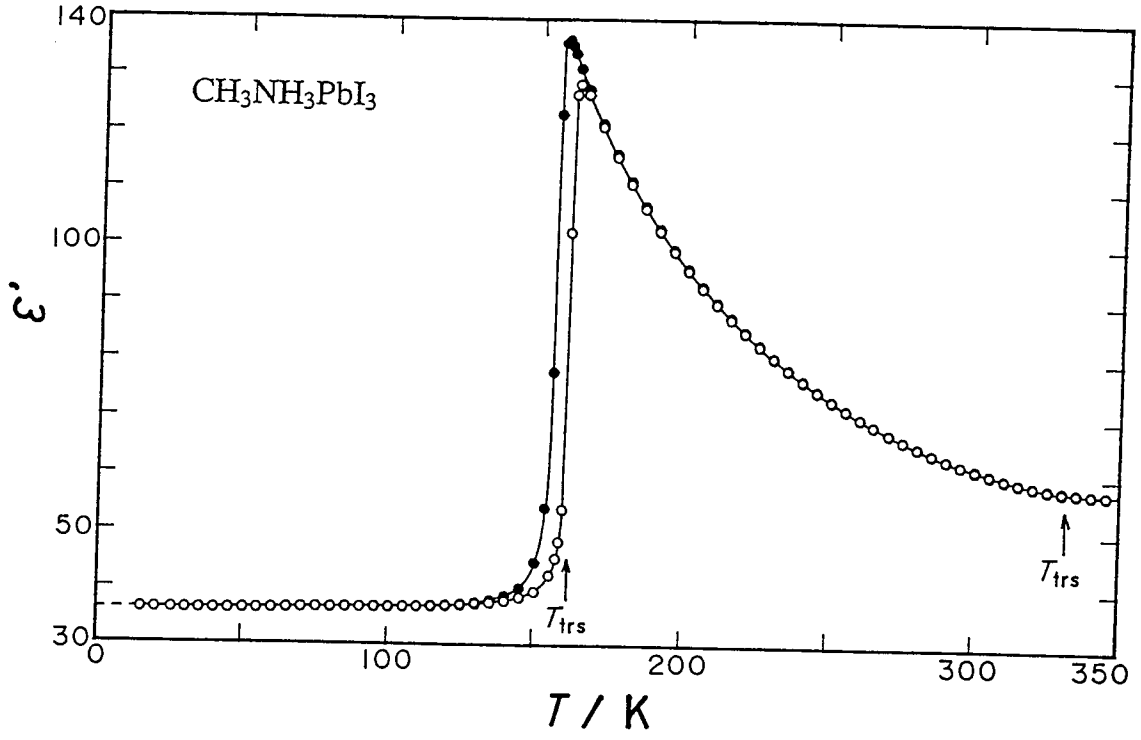

Fig. 3-17 Temperature dependence of the real part of the dielectric permittivity of $CH_3NH_3PbI_3$ taken at 1 kHz in heating (open symbols) and cooling (closed symbols).

in Section 3.3). The small hump around 240 K and the slight increase above 290 K where a decrease is expected are due to a small amount of water which was caught in the sample disks or adsorbed on the sample surface and grain boundary. The values ε' and ε'' were frequency dependent in these temperature range and the effect of the water decreased in magnitude with increasing frequency.

With decreasing temperature, the ε' values of $MAPbCl_3$ increased with an increasing slope and dropped at the cubic-tetragonal II phase transition and further at the tetragonal II-orthorhombic I transition. For $MAPbBr_3$, the ε' values increased with decreasing temperature in the cubic and tetragonal I phases. No obvious change occurred at the transition between these two phases. A sharp bend and discontinuous decrease were observed at the tetragonal I-tetragonal II and the tetragonal II-orthorhombic II transitions, respectively. For $MAPbI_3$, the dielectric permittivity of the cubic phase continued without break onto that of the tetragonal I phase, following a Curie-Weiss type temperature dependence down to the transition temperature, 161 K, where ε' showed discontinuity at the tetragonal I-orthorhombic II transition.

3.4.2 Cubic and Tetragonal I Phases

In these phases, the ε' curves show $1/T$ [or $1/(T-T_c)$] like temperature dependence. It indicates that the dipoles are disordered in these phases. Static permittivity ε_0 of a pure polar liquid is described by the Kirkwood-Fröhlich equation [23],

$$\frac{(\varepsilon_0 - \varepsilon_\infty)(2\varepsilon_0 + \varepsilon_\infty)}{\varepsilon_0(\varepsilon_\infty + 2)^2} = \frac{1}{9\varepsilon_v} \cdot g \cdot \frac{N\mu^2}{k_B T}, \qquad (3\text{-}9)$$

where ε_∞ denotes the permittivity at the high frequency limit, ε_v the permittivity of free space (= 8.854×10^{-12} F m^{-1}), N the number density of the dipoles, μ the permanent dipole moment, k_B the Boltzmann constant (= 1.381×10^{-23} J K^{-1}) and g the Kirkwood correlation factor. The equation has been rewritten in the SI unit. The factor g is a measure of the short range order which is equal to 1 when no specific interactions exist between neighboring molecules. This equation was applied to the present data, because the dielectric behavior of the orientationally disordered solid is expected to resemble that of the polar liquid to a considerable extent. Since the temperature dependence of ε' is Curie-Weiss like rather than Curie like for all the compounds, as shown in the figures, the term T was replaced by $(T - T_C)$ [24] where T_C is the Curie-Weiss temperature. For simplicity, no specific correlation between MA ions was supposed (therefore g = 1). The N values (5.47, 4.85 and 3.95×10^{27} m^{-3} for $MAPbCl_3$, $MAPbBr_3$ and $MAPbI_3$, respectively) were calculated from their molar volumes in the cubic phases reported by Poglitsch and Weber [2]. The ε' data measured at 100 kHz were used in the fitting, since they were not affected by the adsorbed water. Moreover the data which were deemed free from the influence of the transitions were used. As noted above, the cubic-tetragonal I transition caused no apparent change in the permittivity. However, good fits were not achieved if the experimental data for the fitting involved both the tetragonal I and cubic phases. Therefore, the functions

were fitted separately for the two phases. For $MAPbI_3$, only the tetragonal phase was analyzed in this way because the data set on the cubic phase was limited to a narrow temperature interval. Good fit was not achieved for the tetragonal phase of the $MAPbBr_3$, even though the general temperature dependence was similar for the three compounds. The results of the fitting are shown in Fig. 3-18. Parameters determined by the least-squares method are given in Table 3-10.

The dipole moment thus determined is $1.5 \sim 3.0 \times 10^{-30}$ C m. Comparable values were reported by Poglitsch and Weber[2]. According to an ab-initio calculation of the electronic structure of the MA ion, the CH_3 group carries +0.340 e and NH_3 group +0.660 e where e is the positive elementary charge [25]. This may be regarded as $(0.5 - 0.160)e$ on CH_3 and $(0.5 + 0.160)e$ on NH_3, giving rise to a dipole moment of $0.160e\,l = 3.98 \times 10^{-30}$ C m = 1.193 D, where $e = 1.602 \times 10^{-19}$ C and l = 0.1553 nm, the C-N distance [25].

3.4.3 Tetragonal II Phase

Both $MAPbCl_3$ and $MAPbBr_3$ have tetragonal II phase over a narrow temperature range. Discontinuities of the dielectric constant occur at the tetragonal II-orthorhombic (I or II) transitions. The ε' values in this phase are much larger than those in the orthorhombic I or II phase. This indicates that a substantial fraction of the dipoles are disordered in the tetragonal II phase. The increase of ε' with increasing temperature indicates that there exist a long range order of the dipole moments in this phase [26]. The heat capacities of the

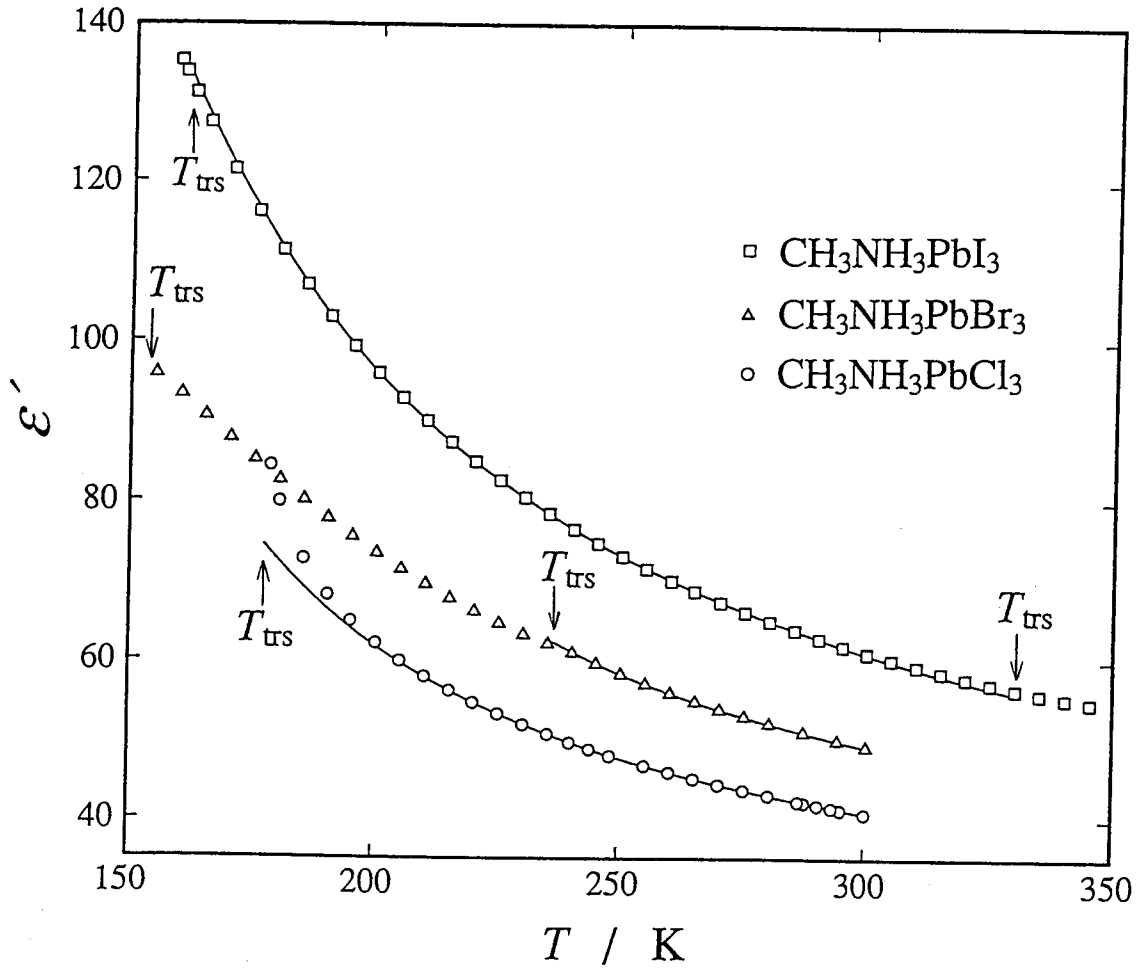

Fig. 3-18 Temperature dependence of the dielectric constant of the tetragonal I4/mcm (tetragonal I) phase and cubic phases of $CH_3NH_3PbX_3$ (X = Cl, Br, I) taken at 100 kHz. The best fit curves representing the modified Kirkwood-Fröhlich equation (Eq. 3-9) are shown as solid lines.

Table 3-10 Temperature regions of the dielectric constant data used in the fitting and optimized parameters in the modified Kirkwood-Fröhlich equation (Eq. 3-9) for $CH_3NH_3PbX_3$ (X = Cl, Br, I).

	$CH_3NH_3PbCl_3$	$CH_3NH_3PbBr_3$	$CH_3NH_3PbI_3$
Temperature region used in the fitting	210 - 300 K	250 - 300 K	180 - 300 K
Parameters optimized			
T_C / K	96.9	123.4	78.4
μ / 10^{-30} C m	1.83	1.50	2.94
μ / D	0.549	0.450	0.881
ε_∞	22.1	28.7	23.3

tetragonal II phase of $MAPbBr_3$ and $MAPbCl_3$ are considerably larger than the normal vibrational heat capacity (see Fig. 3-4 and 3-5). The excess heat capacities may be related to the disordering of this (partial) long range order.

In the previous paragraph (section 3.4), two models of orientational disorder of the MA ion in this phase were presented on the basis of the transition entropy; One is that the MA ion is disordered over four equivalent orientations along the body diagonals of the tetragonal lattice but is ordered as to the C-N exchange and around the C-N axis. The other is that the MA ion is orientationally ordered along the tetragonal axis but is disordered as to the rotation about the C-N axis. The present experimental data showing a substantial orientational component in the permittivity in this phase are more in line with the first model, because one cannot expect an orientational dielectric response in the second model in which the MA ions are disordered only about the C-N axis. However, the second model cannot be totally ruled out if one considers additional motion of the MA ion such as precession of the C-N axis about the tetragonal axis [5,6], or partial disorder of the head-to-tail ordering. Some motion of the C-N axis was also supported by the ^2H NMR study in this phase [4].

3.4.4 Orthorhombic I and II Phases

In these phases, the ε' values are practically temperature independent. Their magnitude (ε' =17 for $MAPbCl_3$, 26 for $MAPbBr_3$, and 36 for $MAPbI_3$) is consistent with what one expects from electronic and ionic polarizations.

Weak dielectric dispersion and loss were found in $MAPbBr_3$ and $MAPbI_3$. Figures 3-19 and 3-20 show the real (upper) and imaginary (lower) parts of the dielectric permittivity for $MAPbBr_3$ and $MAPbI_3$, respectively. Symbols ○△□▽◇ denote the data taken at frequencies of 100 Hz, 1 kHz, 10 kHz, 100 kHz and 1 MHz, respectively. The ε'' values at 100 Hz and 1 MHz contain a constant value of instrumental origin and thus should be shifted downward. As one can see in Figs. 3-19 and 3-20, the dielectric dispersion and loss occurred in the same temperature range for the two compounds.

The temperatures at which the ε'' curves take the maximum were read off from the figure. The relaxation time τ of the motion related to the dielectric dispersion was calculated by using the relation,

$$\tau = 1/(2\pi f). \qquad (3\text{-}10)$$

Figure 3-21 shows the Arrhenius plot of the relaxation time. The activation energies obtained from the plot are 9.8 and 9.7 kJ mol^{-1} for $MAPbBr_3$ and $MAPbI_3$, respectively.

As discussed above on the basis of the experimental transition entropy (Section 3.4), the MA ion is ordered both with respect to the orientation of the C-N axis itself and around the C-N axis in the orthorhombic I or II phases. It was therefore unexpected to find the dielectric dispersions in $MAPbBr_3$ and $MAPbI_3$ in these phases. The temperatures at which the relaxation time becomes comparable with the calorimetric experimental time ($\sim 10^3$ s) are 33.7 K and 34.4 K for $MAPbBr_3$ and $MAPbI_3$, respectively. These temperatures were estimated by extrapolation of

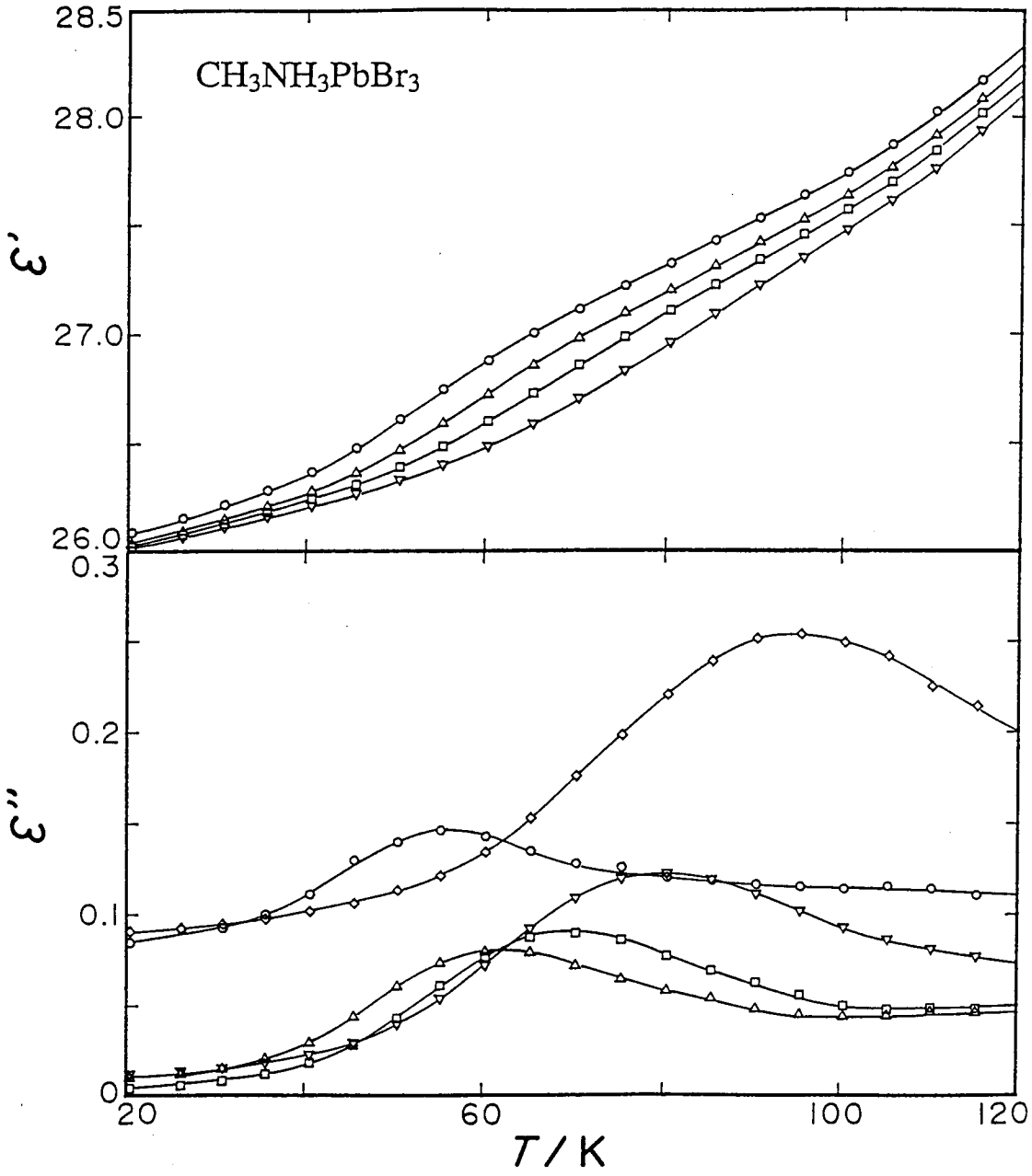

Fig. 3-19 Temperature dependence of the real (upper) and imaginary (lower) parts of the dielectric permittivity of $CH_3NH_3PbBr_3$ in the orthorhombic phase.

○: 100 Hz, △: 1 kHz, □: 10 kHz, ▽: 100 kHz, ◇: 1 MHz.

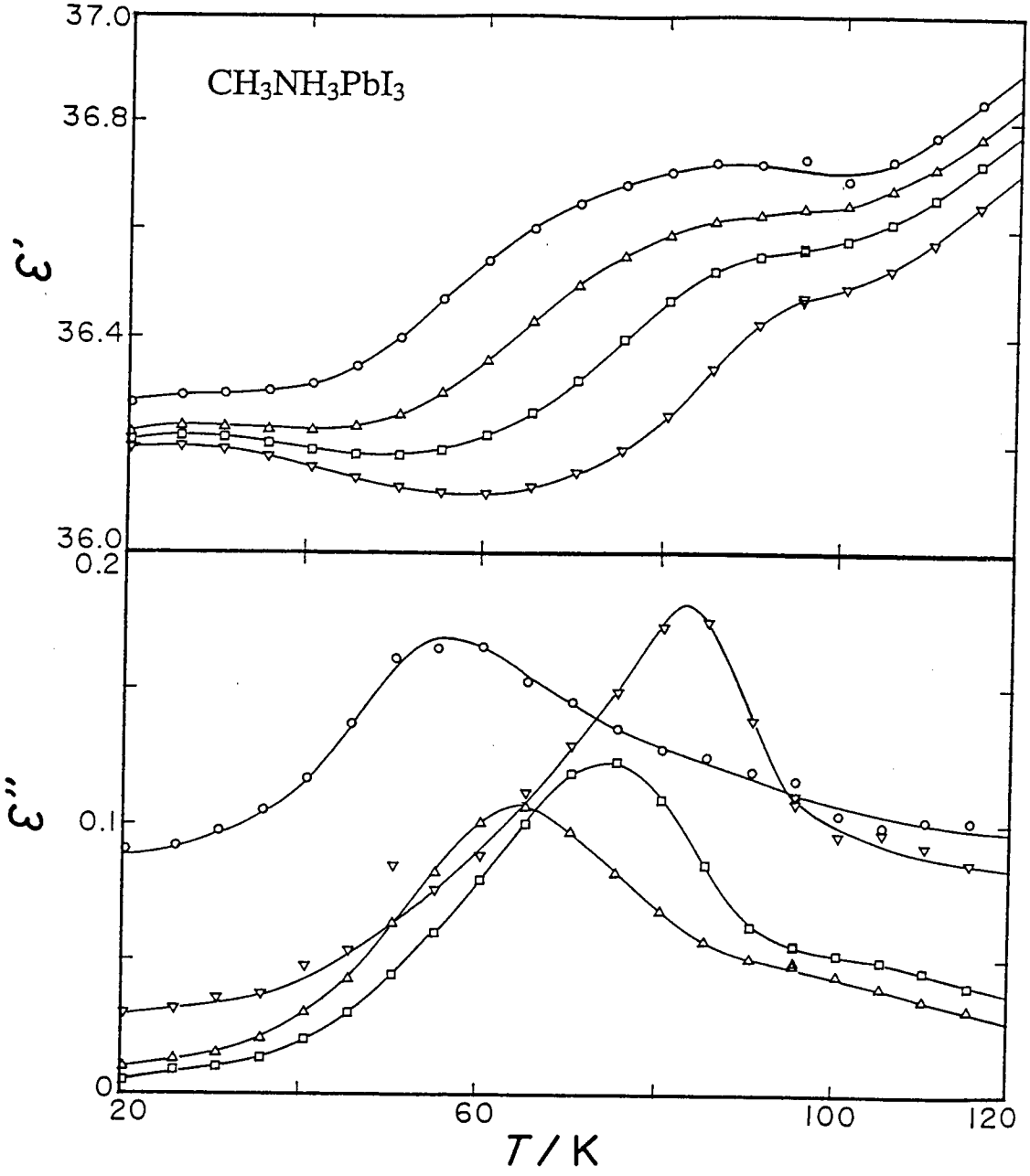

Fig. 3-20 Temperature dependence of the real (upper) and imaginary (lower) parts of the dielectric permittivity of $CH_3NH_3PbI_3$ in the orthorhombic phase.

○: 100 Hz, △: 1 kHz, □: 10 kHz, ▽: 100 kHz.

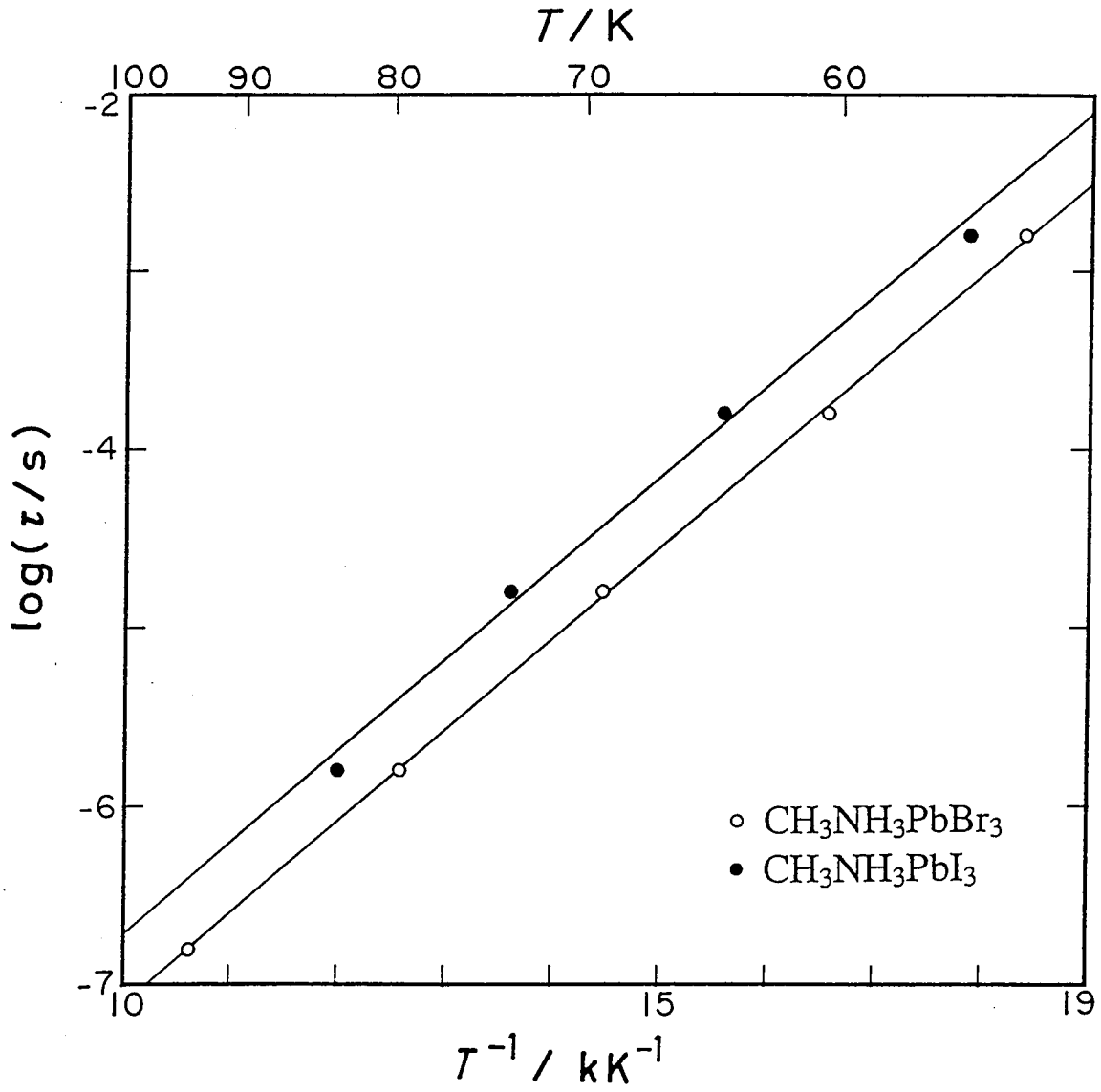

Fig. 3-21 Arrhenius plots of the dielectric relaxation time for $CH_3NH_3PbBr_3$ and $CH_3NH_3PbI_3$.

the Arrhenius plot. However, no glass transition was found at these temperatures in the actual heat capacity measurement. The orthorhombic II-tetragonal I transition is of the first order but it has a precursory effect below the transition temperature (see Figs. 3-12 and 3-13). The dielectric dispersion may be related to the partial disorder represented by the precursory effect. The magnitude of the dielectric dispersions is very small in comparison with the dielectric permittivity coming from the orientational effect at the orthorhombic II-tetragonal II transition. They are only about 1 % and 0.5 % for $MAPbBr_3$ and $MAPbI_3$, respectively. The activation energies 9.8 and 9.7 kJ mol^{-1} may represent the barriers which an MA ion experiences as it reorients in the crystal. However, the type of molecular motion responsible for the dispersion cannot be identified at present because of the small magnitude of the effect.

3.5 High Pressure DTA

3.5.1 High Pressure DTA Curves

Figure 3-22 shows the experimental DTA curves of $MAPbCl_3$ at several pressures up to 75.0 MPa. The heating rate was 0.3-0.4 K min^{-1}. At atmospheric pressure (0.1 MPa), two endothermic peaks corresponding to the orthorhombic I-tetragonal II and tetragonal II-cubic transitions were observed at 171.4 K and 177.2 K, respectively. With increasing pressure, the peak at 171.4 K shifted to higher temperatures and the one at 177.2 K to lower temperatures. The two peaks merged into one at 75.0 MPa, above which only a single peak was observed. This indicates the existence of a triple point around 75 MPa in $MAPbCl_3$.

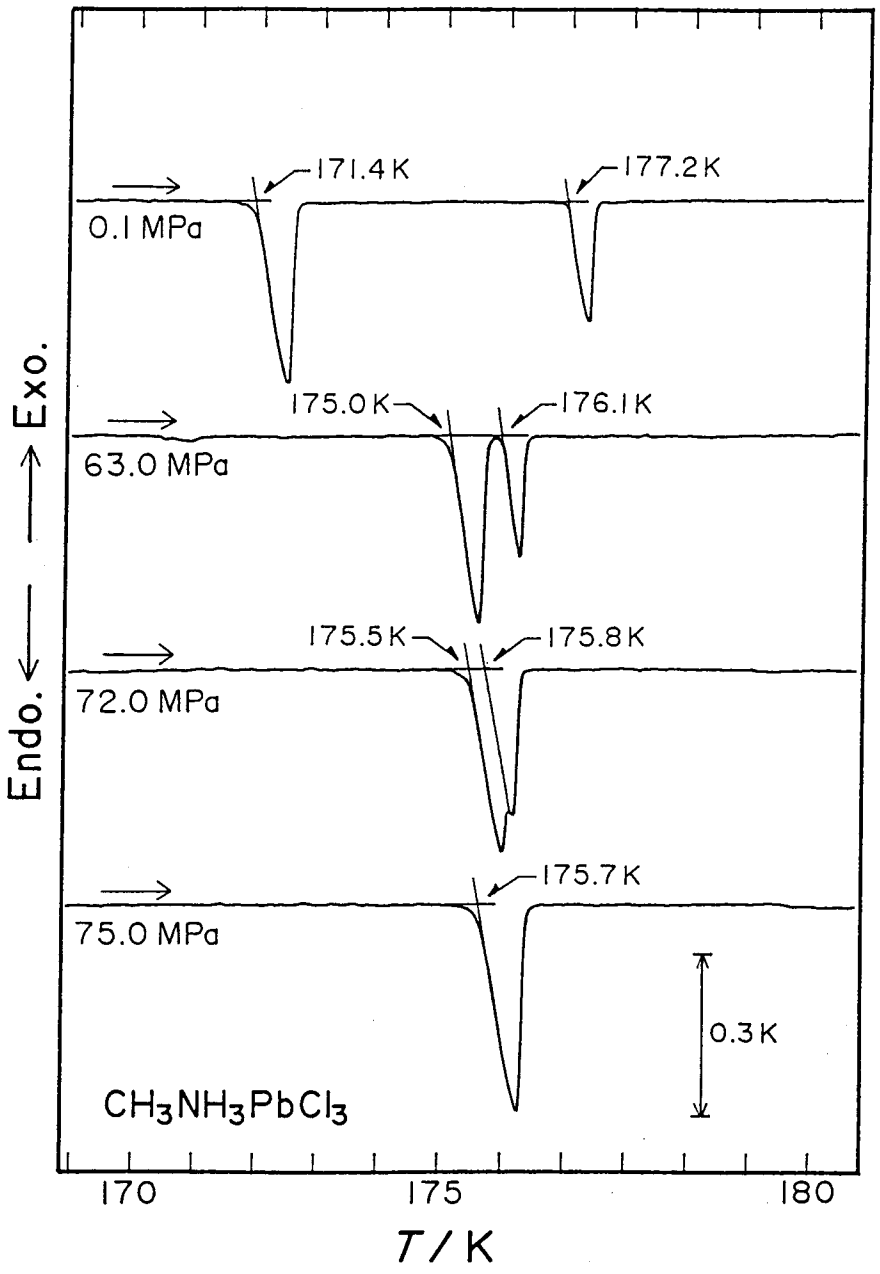

Fig. 3-22 DTA curves of $CH_3NH_3PbCl_3$ under various pressures.

Figure 3-23 shows the experimental DTA curves of $MAPbBr_3$ in the low temperature range. The heating rate was 0.3-0.4 K min^{-1}. The triple point among the orthorhombic II, tetragonal II, and tetragonal I phases of $MAPbBr_3$ crystal was located around 43 MPa. Figure 3-24 shows the experimental DTA curves of $MAPbI_3$ in the low temperature region. The heating rate was 0.6-0.9 K min^{-1}. The orthorhombic II-tetragonal I transition of the crystal occurred at higher temperatures with increasing pressure. On further pressurization, the peak split into two around 85 MPa. The two peaks separated further at higher pressures. This indicates that the triple point exists at about 85 MPa, above which a new phase appears. Thus, the triple points were found in all of the three $MAPbX_3$ (X = Cl, Br, I) crystals below 100 MPa.

The experimental DTA curves of $MAPbBr_3$ and $MAPbI_3$ in the high temperature region are shown in Figs. 3-25 and 3-26, respectively. The heating rates were 0.7-1.0 and 0.7-0.8 K min^{-1} for $MAPbBr_3$ and $MAPbI_3$, respectively. An endothermic peak due to the tetragonal I-cubic transition was observed in both samples. As indicated by the scales (and by the increased noise level in the base line of the curves) in Figs. 3-25 and 3-26, the peak heights of these transitions are much smaller than those of the other transitions shown before. This is because the tetragonal I-cubic transitions of both crystals are of a gradual type and the first-order component of the transition entropy is only 4-6 % of the total (see Section 3.3). The peak temperature decreased monotonically and the peak shape became broader with increasing pressure for $MAPbBr_3$. For $MAPbI_3$, however, the transition line had a maximum around 110 MPa, below which the slope dT_{trs}/dp was

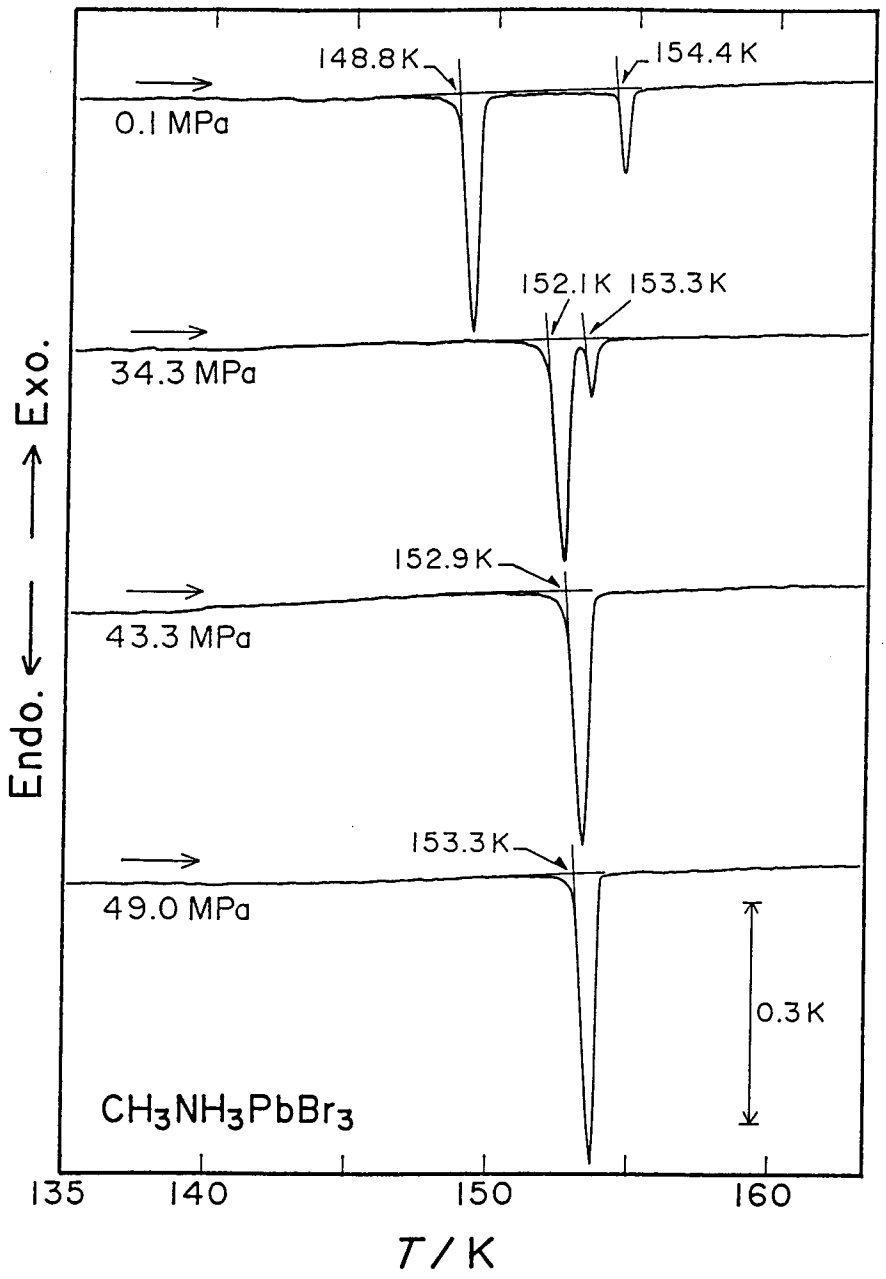

Fig. 3-23 DTA curves of $CH_3NH_3PbBr_3$ under various pressures in the low temperature range.

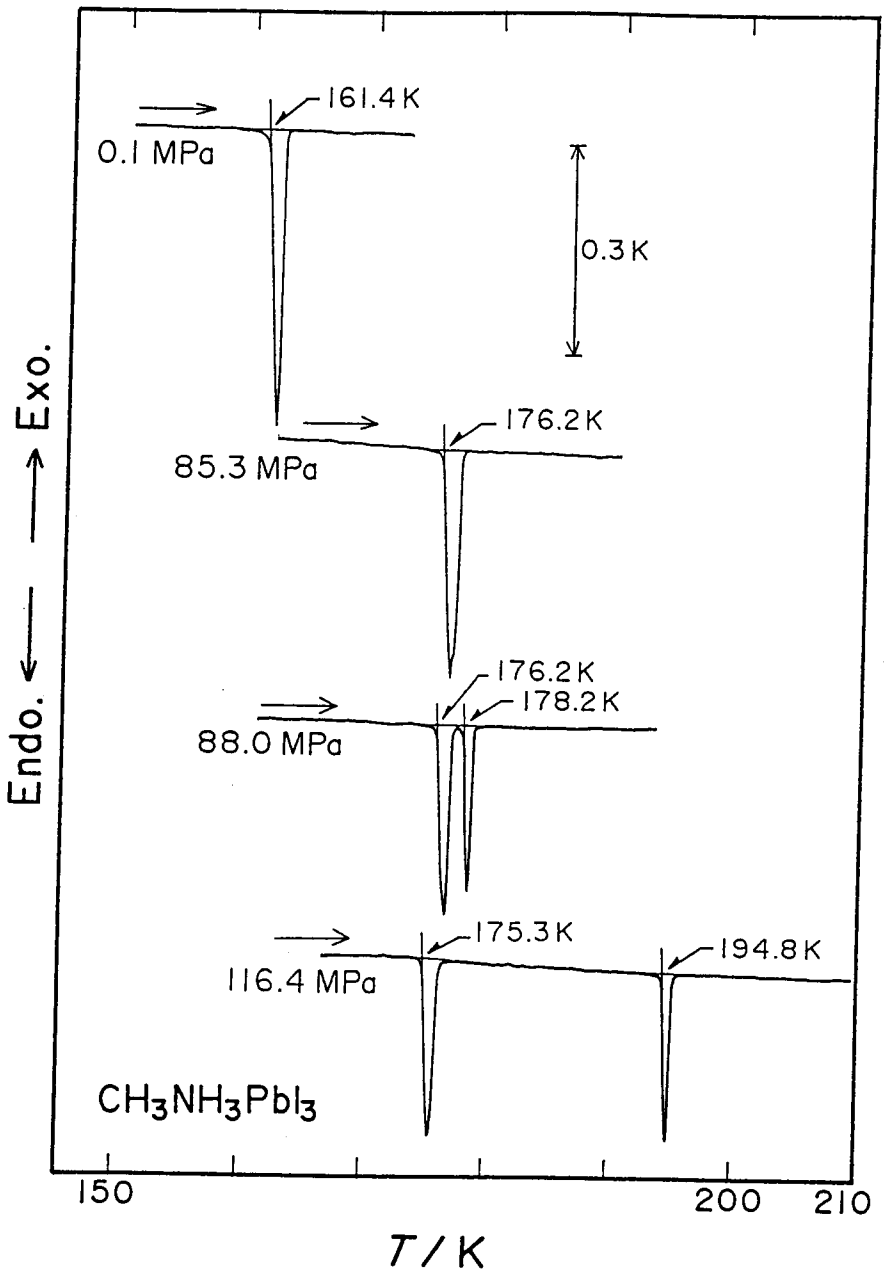

Fig. 3-24 DTA curves of $CH_3NH_3PbI_3$ under various pressures in the low temperature range.

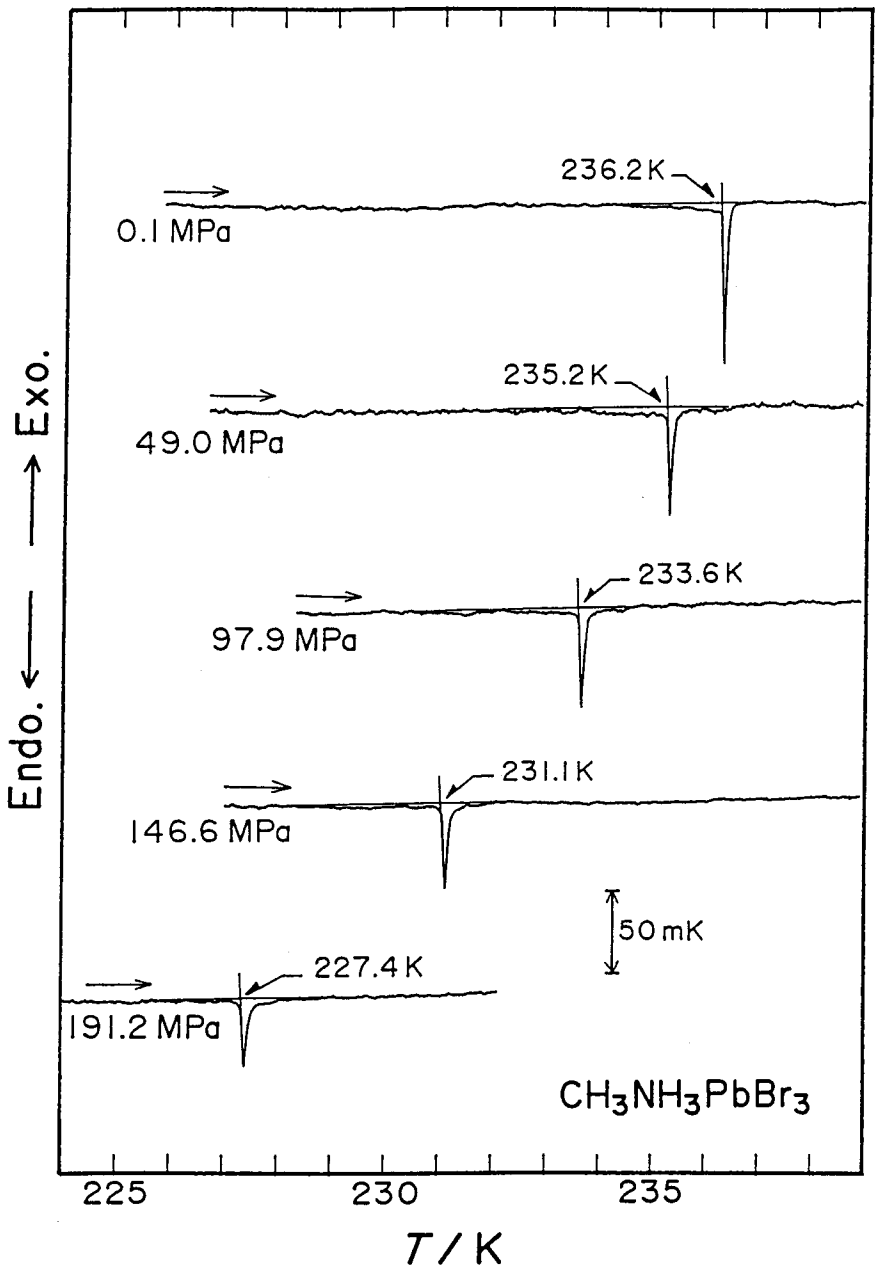

Fig. 3-25 DTA curves of $CH_3NH_3PbBr_3$ under various pressures in the high temperature range.

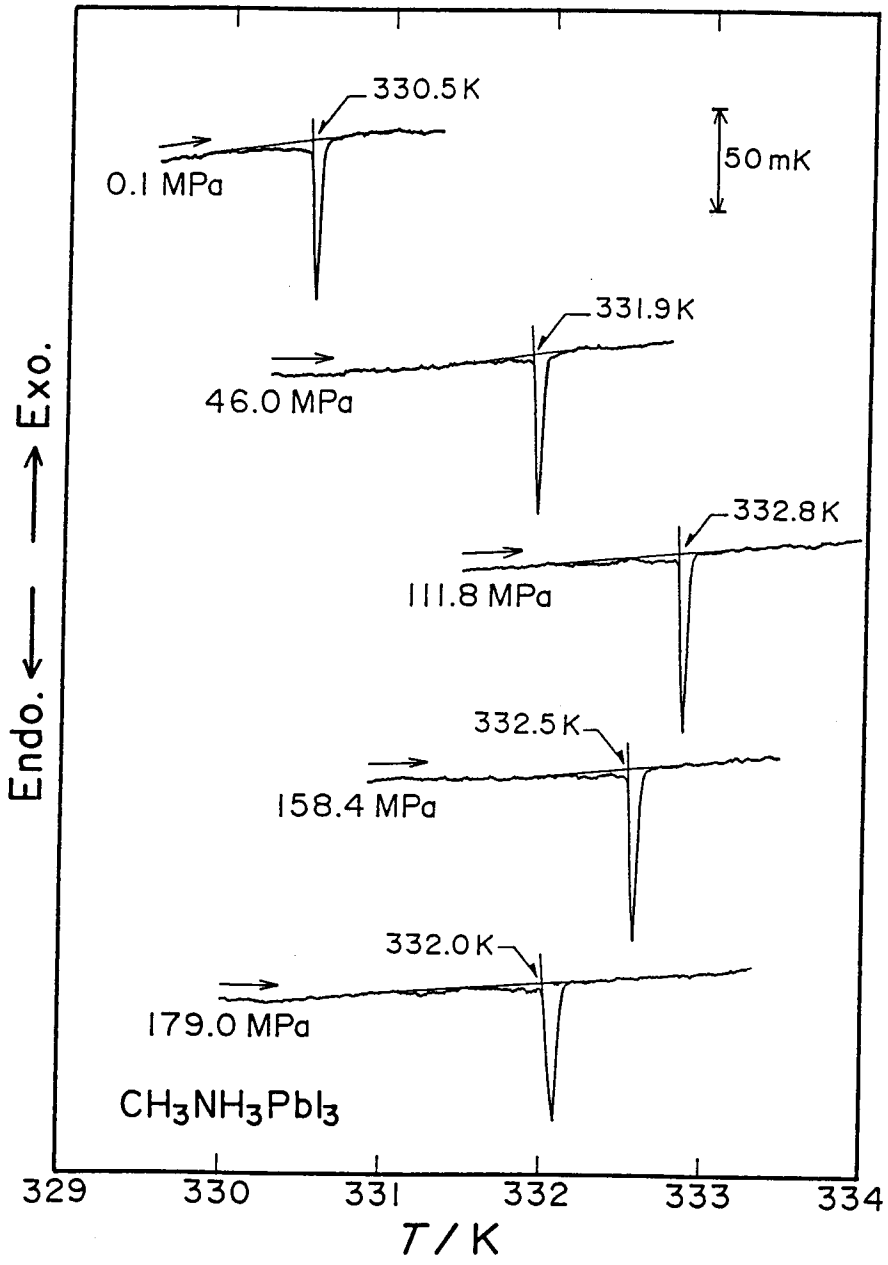

Fig. 3-26 DTA curves of $CH_3NH_3PbI_3$ under various pressures in the high temperature range.

positive and above which negative. The peak shape and area did not change significantly in the whole pressure range.

3.5.2 Pressure-Temperature Phase Relation

Table 3-11 summarizes the transition temperature T_{trs}, its pressure dependence dT_{trs}/dp, the transition entropy $\Delta_{trs}S$, and the transition volume $\Delta_{trs}V$. Here, $\Delta_{trs}S$ is the value determined from the calorimetry at atmospheric pressure (from Table 3-9). The quantity includes the contribution from the gradual part of the transition. The volume change associated with the transition $\Delta_{trs}V$ was derived from the dT_{trs}/dp and $\Delta_{trs}S$ values combined with the Clausius-Clapeyron equation,

$$\frac{dT_{trs}}{dP} = \frac{\Delta_{trs}V}{\Delta_{trs}S} . \qquad (3\text{-}11)$$

All the values of the transition volume are quite small; less than 2 % of the molar volume of $MAPbX_3$ (Cl: 110 $cm^3\ mol^{-1}$, Br: 124 $cm^3\ mol^{-1}$, I: 153 $cm^3\ mol^{-1}$). This indicates that the structural disorder discussed in Section 3.4 in relation to the transition entropies is such that the MA ions are packed as efficiently in the disordered phases as in the ordered phases.

Figure 3-27 depicts the pressure-temperature phase diagram of the three $MAPbX_3$ (X = Cl, Br, I) crystals. The triple points are found in all of these compounds at rather low pressures compared with those of other ammonium and methylammonium compounds [27, 29, 30]. The precise locations of the triple point were determined as the intersections of the extrapolated transition lines. They are as follows;

Table 3-11 Thermal quantities related to the phase transitions of $CH_3NH_3PbX_3$ (X = Cl, Br, I).

compound	transition	dT_{trs}/dP / 10^{-2} K MPa^{-1}	T_{trs} / K	$\Delta_{trs}S$ a) / J K^{-1} mol^{-1}	$\Delta_{trs}V$ b) / cm^{3}mol^{-1}
$CH_3NH_3PbCl_3$	tet II - cubic	-0.61*	177.2(177.2)	14.6	-0.09
	ortho I - cubic	3.2	——	—	—
	ortho I - tet II	5.7	171.4(171.5)	10.0	0.57
$CH_3NH_3PbBr_3$	tet I - cubic	-0.57*	236.2(236.3)	8.2	-0.05
	tet II - tet I	-3.2	154.4(154.0)	4.1	-0.13
	ortho II - tet II	9.6	148.8(148.8)	11.2	1.08
	ortho II - tet I	7.1	——	—	—
$CH_3NH_3PbI_3$	tet I - cubic	3.5*	330.5(330.4)	9.7	0.34
	ortho II - tet I	17.5	161.4(161.4)	19.0	3.3
	? - tet I	58.1	——	—	—
	ortho II - ?	-3.6	——	—	—

cubic : Pm3m, tet I : tetragonal I4/mcm, tet II : tetragonal P4/mmm

ortho I : orthorhombic $P222_1$, ortho II : orthorhombic $Pna2_1$.

? : a new high pressure phase.

* : gradient at 0.1 MPa (atmospheric pressure).

( ): value determined by the heat capacity measurement (Table 3-9).

a) : from reference [2].

b) : calculated by the Clausius-Clapeyron equation.

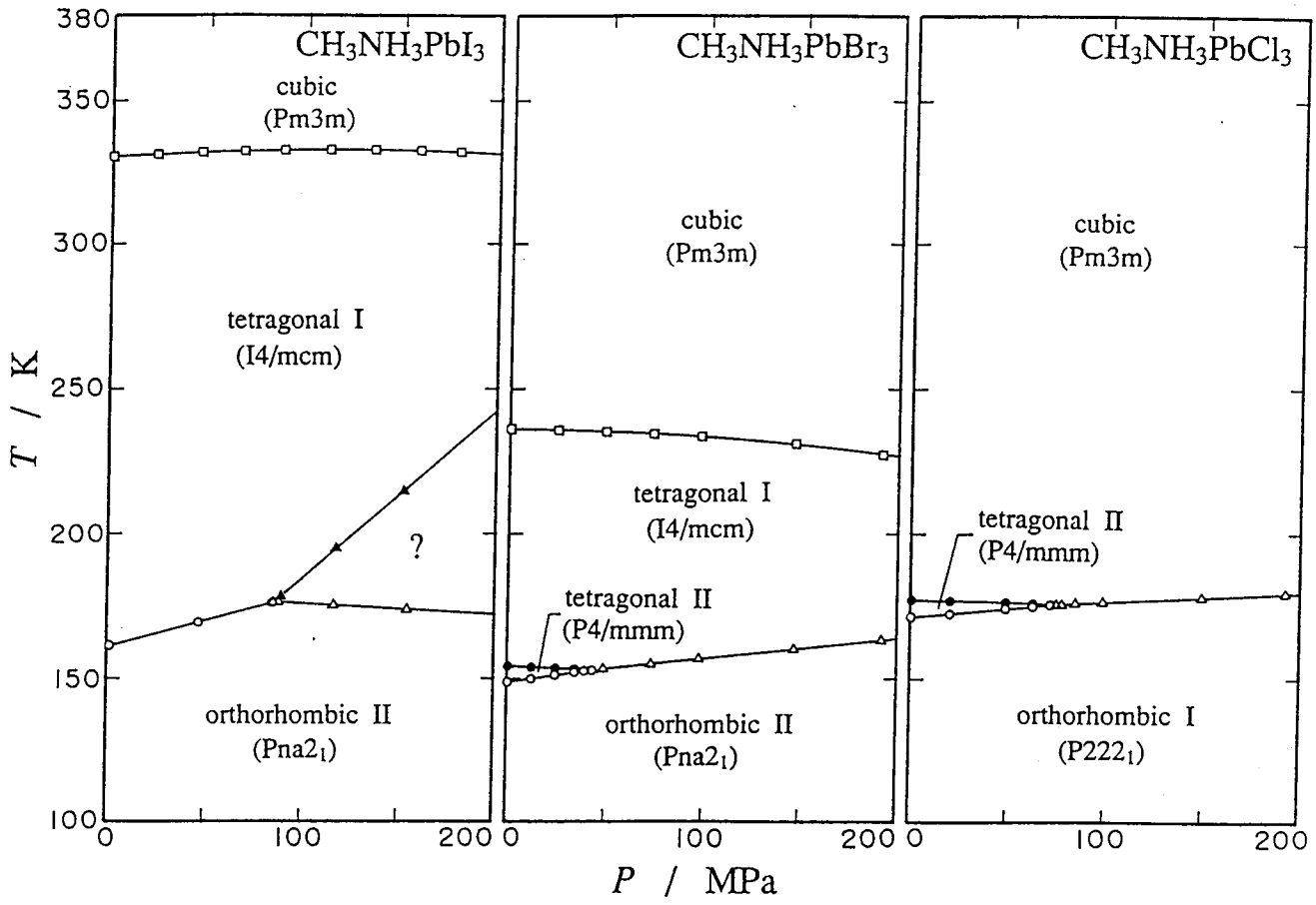

Fig. 3-27 *P-T* phase diagrams of $CH_3NH_3PbX_3$ (X = Cl, Br, I) crystals. Space groups are determined by Poglitsch and Weber [2].

$MAPbCl_3$: 75.1 MPa, 175.7 K,

$MAPbBr_3$: 43.2 MPa, 152.9 K,

$MAPbI_3$: 84.8 MPa, 176.2 K.

The high pressure phase of $MAPbI_3$ was found for the first time in the present work. By analogy with the phase relations of $MAPbBr_3$ and $MAPbCl_3$, this phase may have the same structure as the tetragonal II phase of $MAPbBr_3$ and $MAPbCl_3$. Structural study of this new phase under pressure is highly desirable.

All the boundaries between the cubic and tetragonal phases are upward convex while the other phase boundaries are essentially straight lines in the pressure and temperature ranges studied here. It is noteworthy that the transition line from the tetragonal to cubic phase in the iodide has a maximum around 120 MPa. This means that the transition volume $\Delta_{trs}V$ changes its sign from positive to negative according to the Clausius-Clapeyron equation. The transition entropy $\Delta_{trs}S$ should be positive for the thermodynamic stability condition, and in fact is practically constant in the whole pressure region studied as revealed by the shape and area of the DTA peaks (Fig. 3-26).

An elegant systematic relation between the pressure and the ionic size of the halogen ion is known to hold in ammonium halides [30]: Ammonium chloride under atmospheric pressure corresponds to ammonium iodide under a high pressure while ammonium bromide corresponds to a situation in between with respect to the relative stability of three crystalline phases differing from each other in the relative orientations of the ammonium ions. No such simple relation has been found so far for the present sub-

stances. This is probably due to the complexity of the interionic interaction and the manner in which the orientational disorder takes place in the present compounds as compared with ammonium halides. However, we can make a general statement from the phase diagram given in Fig. 3-27: the stability domain of the tetragonal phase narrows at higher pressure both from below and above. Thus the molar volume of the tetragonal phase is larger than those of the cubic and orthorhombic phases (in the iodide, for $p > 120$ MPa). It is unexpected that the molar volume decreases as the crystal undergoes the phase transition from the partially ordered tetragonal phase to the fully disordered cubic phase, even though the change in the molar volume is rather small as noted above. It is more common to find an increase of the molar volume accompanying a phase transition from an ordered to a disordered phase. However, molar volume reduction has also been found in methylammonium iodide as it undergoes a phase transition from a partially ordered tetragonal phase to the fully disordered cubic phase [29]. Significance at the molecular level of these uncommon properties shared by the crystals containing methylammonium ions is still to be investigated. In particular, numerical calculation of the interionic interactions among three ions (MA^+, Pb^{2+}, X^-) taking various types of orientational disorder into account is a subject for a future study.

References to Chapter 3

1. D. Weber, *Z. Naturforsch.*, 33b, 1443 (1978).
2. A. Poglitsch and D. Weber, *J. Chem. Phys.*, 87, 6373 (1987).
3. R. E. Wasylishen, O. Knop and J. B. MacDonald, *Solid State Commun.*, 56, 581 (1985).
4. O. Knop, R. E. Wasylishen, M. A. White, T. S. Cameron and M. J. M. V. Oort, *Can. J. Chem.*, 68, 412 (1990).
5. Y. Furukawa and D. Nakamura, *Z. Naturforsch.*, 44a, 1122 (1989).
6. Q. Xu, T. Eguchi, H. Nakayama, N. Nakamura and M. Kishita, *Z. Naturforsch.*, 46a, 240 (1991).
7. T. Sandius and N. Meinander, *J. Molec. Structure*, 76, 227 (1981).
8. I. A. Oxton, O. Knop and J. L. Duncan, *J. Molec. Structure*, 38, 25 (1977).
9. T. Matsuo, M. Ueda and H. Suga, *Chem. Phys. Lett.*, 82, 577 (1981).
10. Y. H. Cho, M. Kobayashi and H. Tadokoro, *J. Chem. Phys.*, 84, 4643 (1986).
11. N. Onoda, T. Matsuo and H. Suga, *J. Phys. Chem. Solids*, 47, 211 (1986).
12. W. G. Rothschild, *Dynamics of Molecular Liquids*, Chaps 1 and 2. John-Wiley, New York (1984).
13. D. A. Ramsay, *J. Am. Chem. Soc.*, 74, 72 (1952).
14. *Tables Relating to Mathieu Functions*, Columbia University Press, New York (1951).
15. R. Ikeda, Y. Kume and D. Nakamura, *J. Magn. Reson.*, 24, 9 (1976).
16. C. K. Møller, *Mat. Fys. Medd. Danske Vindensk Selsk.*, 32,

No. 2 (1959).

17. T. Sakudo , H. Unoki, Y. Fujii, J. Kobayashi and M. Yamada, *Phys. Lett.*, A28, 542 (1969).
18. S. Hirotsu and S. Sawada, *Phys. Lett.*, A28, 762 (1969).
19. N. T. Jensen, *J. Chem. Phys.*, 50, 559 (1969).
20. Y. Fujii, S. Hoshino, Y. Yamada and G. Shirane, *Phys. Rev.*, B9, 4549 (1974).
21. S. Hirotsu, *J. Phys. Soc. Jpn.*, 31, 552 (1971).
22. J. C. Ho and W. P. Unruh, *Phys. Rev.*, B13, 447 (1976).
23. C. J. F. Böttcher, *Theory of Electric Polarization*, Scientific Publishing Company, Amsterdam, 1973.
24. R. Bohmer and A. Loidl, *J. Chem. Phys.*, 89, 4981 (1988).
25. M. Masamura, *Chem. Phys. Lett.*, 162, 329 (1989).
26. H. Fröhlich, *Theory of Dielectrics*, Oxford University Press, London, 1958.
27. C. W. F. T. Pistorius, *Prog. Solid State Chem.*, 11, 1 (1976).
28. O. Yamamuro, M. Oguni, T. Matsuo and H. Suga, *Thermochim. Acta*, 99, 67 (1986).
29. O. Yamamuro, M. Oguni, T. Matsuo and H. Suga, *Thermochim. Acta*, 98, 327 (1986).
30. Y. Yamada, M. Mori and Y. Noda, *J. Phys. Soc. Jpn.*, 32, 1565 (1972).

Chapter 4

$CH_3NH_3SnBr_3$

4.1 Introduction

The compound $MASnBr_3$ crystallizes in the cubic perovskite structure and possesses semiconducting conductivity [1]. Occurrence of the phase transitions was shown by DTA and NQR studies [2]. Two large peaks were found at 189 K and 233 K and a small peak at 214 K in the DTA measurement. The former two were confirmed by the NQR study, but the latter was not confirmed because the NQR signal faded out in the limited temperature interval covering 214 K. Considerably large splitting of the NQR frequency [2] and appearance of a quadrupole splitting in the Sn Mössbauer spectra in the lowest temperature phase [1,2] suggested a large distortion of the $SnBr_6$ octahedron from the regular O_h symmetry.

Molecular motion of the MA ion has been investigated by ^1H NMR spectroscopy [2]. The second moment values of 8 G^2 and 0.5 G^2 obtained for the lowest and highest temperature phases were explained by the onset of the reorientational motion of the MA ion around its C-N axis and the overall rotation of the MA ion, respectively.

The electrical property at low temperatures has been studied by dc conductivity measurement using a pressed powder sample [3]. Semiconducting behavior was observed in the room temperature phase. However, no detectable conductivity was found below 229 K. The color change from dark red to yellow associated with this

phase transition also indicates the significant change in the electronic structure.

In this chapter, the results of adiabatic calorimetry (Section 2), ac conductivity (Section 3), dielectric measurement (Section 4) and high pressure DTA (Section 5) are reported and discussed in relation to the phase transitions and molecular motions.

4.2 Heat Capacity

4.2.1 Heat Capacity

The numerical values of the heat capacity are given in Table 4-1 and plotted in Fig. 4-1. Four anomalies were found at 46.0 K, 188.2 K, 213.0 K and 229.4 K. The first one is reported here for the first time. The temperatures of the others agree satisfactorily with those which have been reported [2]. It is obvious from Fig. 4-1 that the anomaly at 46.0 K is much smaller than those of the others. Figure 4-2 shows the heat capacity around the anomaly at 213.0 K in a magnified scale. The heat capacity increases gradually and decreases with a finite gap at this transition. The phase transitions at 46.0 K and 213.0 K are of higher order and the other two are of first order. It is interesting that the heat capacities of the highest temperature phase are almost independent of temperature. Constant heat capacities with temperature were also found in the cubic phases of $MAPbX_3$ (X = Cl, Br, I) (see Fig. 3-4, 3-5 and 3-6).

Table 4-1 Molar heat capacity of $CH_3NH_3SnBr_3$.

T_{av} / K	C_P / J K^{-1}mol^{-1}	T_{av} / K	C_P / J K^{-1}mol^{-1}	T_{av} / K	C_P / J K^{-1}mol^{-1}	T_{av} / K	C_P / J K^{-1}mol^{-1}	T_{av} / K	C_P / J K^{-1}mol^{-1}
11.50	12.25	47.72	89.67	116.67	142.6	191.10	170.3	226.18	252.5
12.39	14.06	48.04	89.78	118.59	143.4	191.65	170.1	226.53	259.4
13.17	15.79	48.35	90.01	120.54	144.2	192.20	170.4	226.87	269.2
13.91	17.47	48.72	90.38	122.49	144.9	192.96	170.5	227.30	285.9
14.64	19.16	49.16	90.89	124.47	145.7	193.92	170.9	227.81	319.3
15.36	20.76	49.63	91.51	126.48	146.3	194.87	171.4	228.27	406.8
16.12	22.52	50.15	92.24	128.48	147.1	195.83	172.1	230.68	241.4
16.87	24.22	50.76	93.05	130.52	147.8	196.78	172.8	231.27	180.3
17.58	25.91	51.66	94.27	132.60	148.5	197.73	173.6	231.89	176.3
18.31	27.73	52.90	95.95	134.66	149.3	198.68	174.5	232.52	174.7
19.05	29.49	54.18	97.70	136.73	150.1	199.62	175.3	233.17	173.5
19.80	31.37	55.45	99.31	138.82	150.8	200.56	176.3	233.84	172.6
20.54	33.19	56.76	101.0	140.95	151.5	201.50	177.4	234.50	171.9
21.28	34.94	58.10	102.7	143.12	152.3	202.43	178.4	235.17	172.0
22.02	36.64	59.48	104.3	145.34	153.1	203.37	179.7	235.94	171.9
22.76	38.46	60.89	105.9	147.53	153.8	204.30	180.9	236.87	171.7
23.49	40.21	62.29	107.4	149.72	154.5	205.22	182.4	237.88	171.5
24.22	41.98	63.71	108.9	151.90	155.2	206.14	184.0	238.90	171.2
24.96	43.71	64.84	110.1	154.08	156.0	207.06	185.7	241.22	170.8
25.70	45.48	66.13	111.4	156.25	156.7	207.97	187.8	243.47	170.6
26.45	47.28	67.32	112.5	158.41	157.5	208.88	190.0	245.68	170.3
27.20	49.01	68.43	113.5	160.56	158.4	209.79	192.9	247.84	169.9
27.96	50.75	69.66	114.7	162.70	159.2	210.49	195.3	250.00	169.7
28.73	52.49	71.18	116.1	164.83	160.0	211.01	197.6	252.16	169.4
29.51	54.32	72.74	117.5	167.00	160.9	211.52	199.6	254.32	169.4
30.31	56.16	74.31	118.7	169.20	162.0	212.03	202.3	256.47	169.3
31.11	57.97	75.91	120.1	171.57	162.9	212.54	204.4	258.63	169.2
31.93	59.77	77.50	121.3	172.64	163.4	213.04	205.5	260.78	169.1
32.76	61.66	79.11	122.5	173.70	164.0	213.55	201.8	262.93	169.1
33.61	63.49	80.75	123.7	174.76	164.4	214.06	193.7	265.08	169.1
34.47	65.33	82.41	124.9	175.82	165.0	214.58	191.0	267.22	169.1
35.37	67.29	84.09	126.1	176.88	165.6	215.10	191.4	269.36	169.1
36.32	69.28	85.77	127.1	177.93	166.3	215.62	192.1	271.50	169.2
37.27	71.24	87.47	128.2	178.98	167.0	216.14	193.1	273.63	169.3
38.23	73.18	89.19	129.3	179.91	167.6	216.83	194.7	275.76	169.4
39.19	75.03	90.93	130.3	180.68	168.3	217.70	197.0	277.89	169.4
40.16	76.94	92.69	131.4	181.37	168.8	218.57	199.5	280.02	169.5
41.13	78.79	94.45	132.3	182.06	169.4	219.43	202.3	282.14	169.5
42.10	80.60	96.23	133.2	182.75	171.7	220.28	205.3	284.26	169.7
43.20	82.61	98.04	134.2	183.44	173.3	221.13	209.0	286.38	169.9
43.75	83.70	99.83	135.2	184.12	175.9	221.86	212.3	288.49	170.0
44.38	84.85	101.63	136.0	184.80	179.2	222.47	215.7	290.60	170.0
44.99	85.87	103.45	136.9	185.47	185.7	223.07	219.3	292.70	170.1
45.53	86.88	105.31	137.8	186.13	199.1	223.62	223.1	294.81	170.3
46.00	87.67	107.16	138.6	186.75	230.4	224.10	226.7	296.91	170.4
46.45	88.34	109.05	139.5	188.90	199.3	224.58	231.3	299.01	170.5
46.81	88.72	110.96	140.4	189.44	171.7	225.05	236.0	301.11	170.6
47.10	89.14	112.87	141.1	189.99	170.6	225.47	241.2		
47.40	89.47	114.78	141.9	190.54	170.5	225.82	246.3		

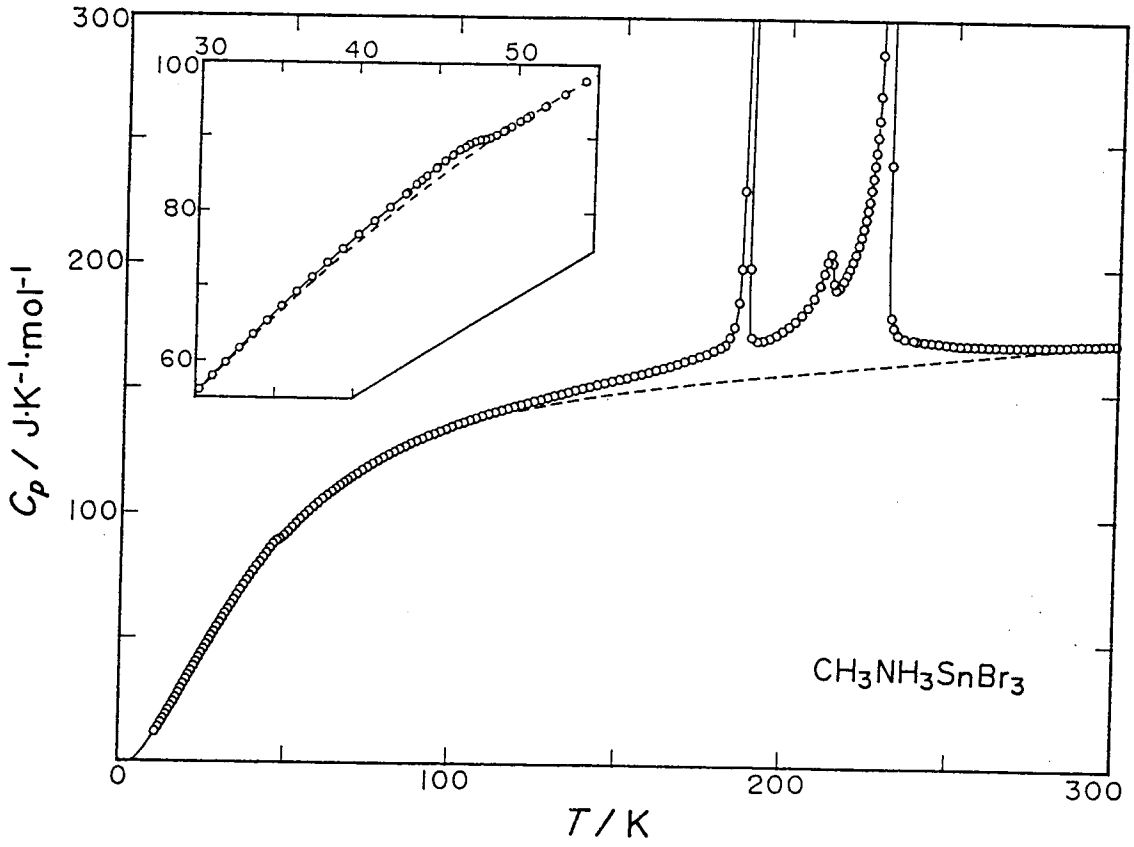

Fig. 4-1 Molar heat capacity of $CH_3NH_3SnBr_3$.

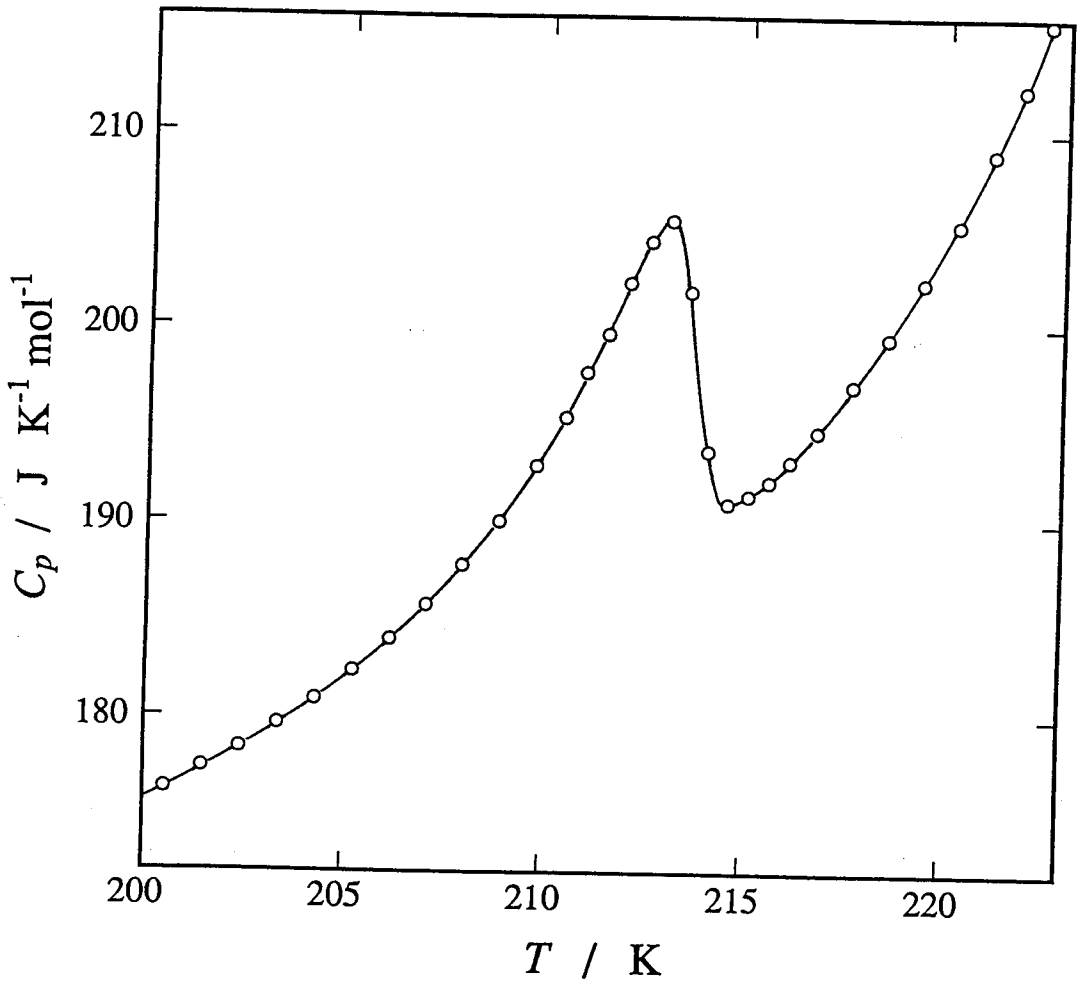

Fig. 4-2 Molar heat capacity of $CH_3NH_3SnBr_3$ around the phase transition at 213.0 K.

4.2.2 Enthalpy and Entropy of Transition

The experimental heat capacity is decomposed additively into the normal and transitional parts. A computational method for evaluating the normal heat capacity of $MAPbX_3$ was described in Chapter 3 (Section 3.2). The same method is used here. In the lack of spectroscopic data on $MASnBr_3$, experimental vibrational frequencies of the MA ion in $MAPbBr_3$ were employed (see Table 3-1 in Chapter 3). For the external rotation of MA ion, a barrier height of 3.9 kJ mol^{-1} determined by NMR study [4] was adopted. The barrier height of the internal rotation has been estimated to be 8.0 kJ mol^{-1} [5]. At the beginning of the calculation, parameters to be optimized to reproduce the normal heat capacity were exactly the same as for $MAPbX_3$: five Einstein temperatures, one Debye temperature, the $(C_p - C_v)$ correction coefficient A included in the expression $C_p - C_v = A C_p^2 T$, and the transition temperature T_0 in the mean field approximation (see section 3.2 in Chapter 3). It was found, however, that a better fitting was obtained if the fitting function was modified as follows. One of the Einstein function of weight 3 was replaced with a Debye function and two Einstein parameters each with weight 3 were combined to one Einstein temperature with weight 6. Parameters determined by the least-squares method are as follows:

$\theta_D^1(3)$ = 100.3 K, $\theta_D^2(3)$ = 311.2 K,
$\theta_E^1(2)$ = 34.4 K, $\theta_E^2(3)$ = 81.4 K, $\theta_E^3(6)$ = 157.0 K,
$A = 9.14 \times 10^{-7}$ mol J^{-1}, T_0 = 268.0 K.

Here, the numbers in the parentheses give the degrees of freedom

and the superscripts distinguish different modes. The heat capacity data used in the least-squares determination of the above parameters are those in 13 - 30 K and 50 - 126 K for the low temperature region and 296 - 300 K for the high temperature region. To eliminate the effect of the 46.0 K transition, the heat capacity data between 30 and 50 K were left out. For the low temperature region, a term representing a mean field solution of a phase transition was added to the model function. The normal heat capacity thus calculated is shown in Fig. 4-1 by the broken curve. Heat capacities below 12 K were also calculated in the same way. The difference between the experimental and normal heat capacities is shown in Fig. 4-3. The anomaly at 46.0 K has a typical temperature dependence of a higher order phase transition. The maximum value of the excess heat capacity was 1.72 J K^{-1} mol^{-1}.

The molar values of the heat capacity, entropy, enthalpy function and Gibbs energy function are listed in Table 4-2 at selected temperatures. These values are based on the present calorimetric data along with the extrapolated fitting curve to zero kelvin. The estimated probable error in the thermodynamic functions is less than 0.1 percent above 100 K.

The enthalpy and entropy of the phase transition were calculated by integration of the excess heat capacity and the excess heat capacity divided by T, respectively. For first order transitions, integration of the excess heat capacity and the addition of the discontinuous part at the phase transition give the transition enthalpy and entropy. The temperature dependence of the transition entropy thus calculated is shown in Fig. 4-4. The transition at 213.0 K is barely perceptible in Fig. 4-4 on ac-

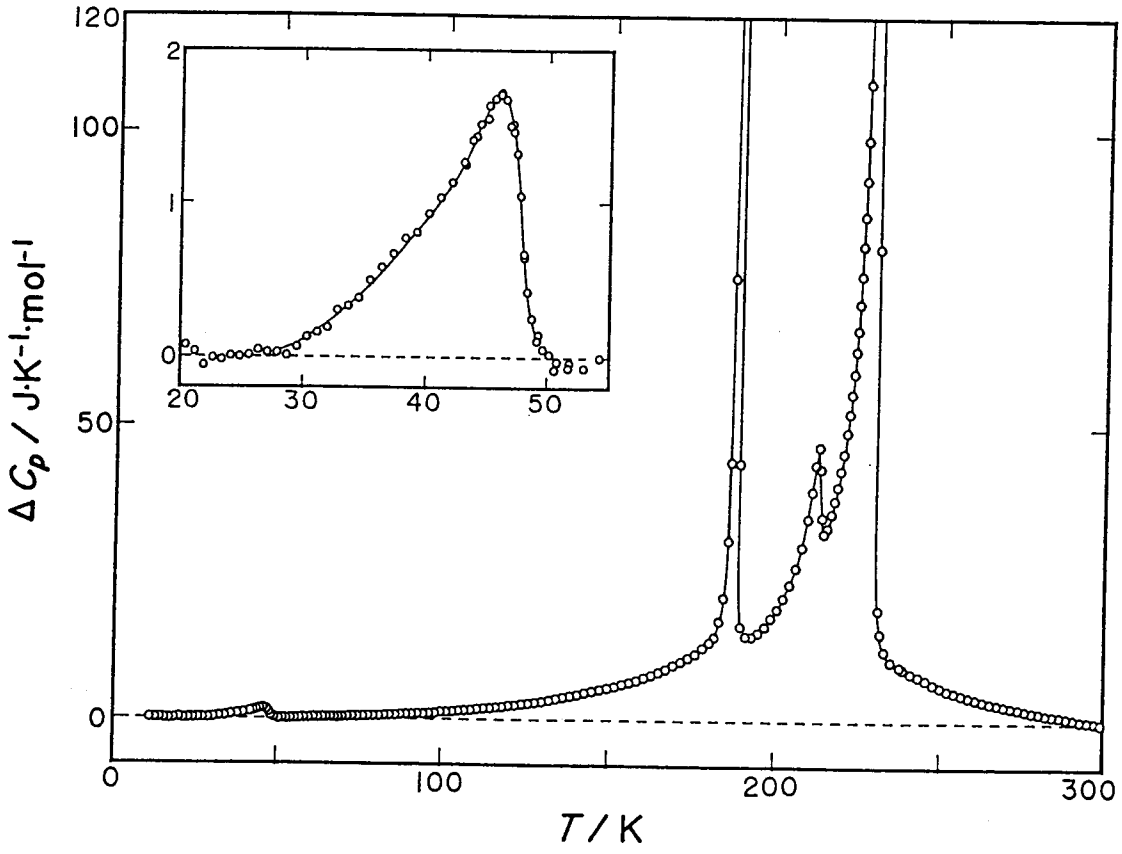

Fig. 4-3 Excess heat capacity of $CH_3NH_3SnBr_3$.

Table 4-2. Thermodynamic functions of $CH_3NH_3SnBr_3$.

$\frac{T}{K}$	C_p/R	$(H-H_0)/RT$	S/R	$-(G-H_0)/RT$
10	(1.103)	(0.2949)	(0.3811)	(0.08621)
20	3.823	1.357	1.950	0.5927
30	6.671	2.659	4.044	1.386
40	9.219	3.989	6.322	2.333
50	11.09	5.243	8.603	3.360
60	12.60	6.347	10.76	4.416
70	13.83	7.332	12.80	5.469
80	14.82	8.208	14.72	6.507
90	15.61	8.988	16.51	7.520
100	16.26	9.684	18.19	8.503
110	16.82	10.31	19.76	9.456
120	17.31	10.87	21.25	10.38
130	17.76	11.38	22.65	11.27
140	18.18	11.86	23.98	12.13
150	18.59	12.29	25.25	12.96
160	19.02	12.70	26.47	13.77
170	19.51	13.08	27.63	14.55
180	20.16	13.46	28.77	15.31
190	20.59	14.08	30.13	16.05
200	21.14	14.41	31.19	16.78
210	23.29	14.77	32.27	17.49
220	24.58	15.18	33.37	18.19
240	20.57	17.19	36.79	19.61
250	20.41	17.32	37.63	20.31
260	20.34	17.43	38.43	20.99
270	20.35	17.54	39.20	21.65
273.15	20.36	17.57	39.43	21.86
280	20.39	17.64	39.94	22.29
290	20.45	17.74	40.65	22.92
298.15	20.50	17.81	41.22	23.41
300	20.51	17.83	41.35	23.52

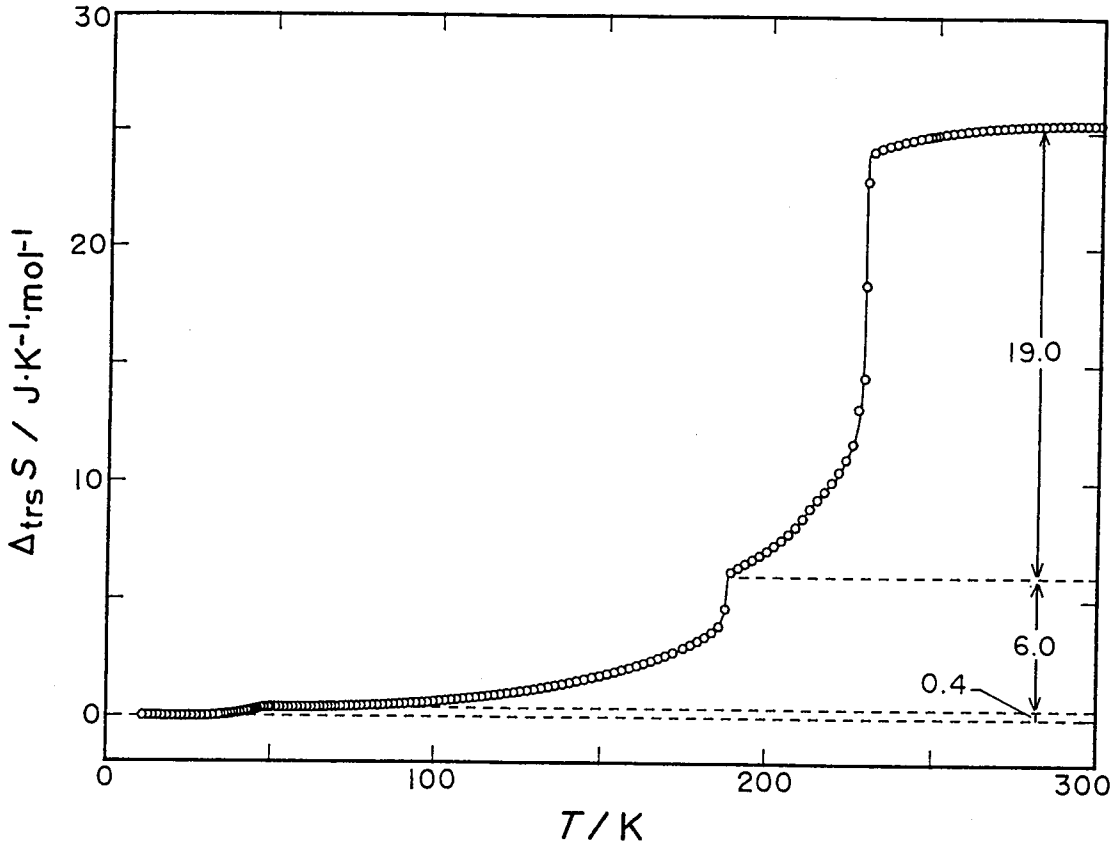

Fig. 4-4 Accumulated transition entropy of $CH_3NH_3SnBr_3$ as a function of temperature.

count of the small magnitude. The thermodynamic quantities associated with the phase transitions are given in Table 4-3. In the table, the enthalpy and entropy of the 213.0 K transition are included in those of the 229.4 K transition. The phase transitions at 188.2 K and 229.4 K overlap each other as shown in Fig. 4-3. The values given in Table 4-3 were calculated by dividing them at 191.1 K where the excess heat capacity took the minimum. The entropies of the 188.2 K and 229.4 K transitions correspond to R ln 2.1 and R ln 9.8, respectively. These values ($\geq R$ ln 2) indicate that both of the transitions are of order-disorder type. On the other hand, the small entropy value of the 46.0 K transition suggests that the phase transition is of a displacive type. The total entropy of the phase transitions is 25.4 J K^{-1} mol^{-1}. Corresponding entropy values for $MAPbX_3$ (X = Cl, Br, I) are 24 ~ 29 J K^{-1} mol^{-1}. Thus $MASnBr_3$ and $MAPbX_3$ have the same extent of disorder in the highest temperature phases.

Transition entropies of $MAPbX_3$ were accounted for with the models of orientational disorder of an MA ion assuming that the MA ion is completely ordered with respect to both the C-N axis itself and around the C-N axis in the lowest temperature phases (see Section 3.4 in Chapter 3). The model entropy R ln 24 was divided into R ln 3, R ln 2 and R ln 4 in the successive ordering models. However, the steps by which the ordering proceeds in $MASnBr_3$ are different from those in the $MAPbX_3$, as indicated by the different sequences of the transition entropy (shown in Table 3-9). The higher order transition at 46.0 K is also specific to $MASnBr_3$ without a counterpart in any of the $MAPbX_3$ family. It may be related with a slight change of ionic packing in the

Table 4-3 Temperatures, enthalpies and entropies of the phase transitions of $CH_3NH_3SnBr_3$.

T_{trs} / K	$\Delta_{trs}H$ / kJ mol^{-1}	$\Delta_{trs}S$ / J K^{-1} mol^{-1}
46.0	0.016	0.37
188.2	1.00	6.02 (R ln 2.1)
213.0	4.28	18.98 (R ln 9.8)
229.4		

crystal with a concomitant change of the lattice vibrational frequencies.

4.3 AC Conductivity

Figure 4-5 shows the frequency dependence of the conductivity measured at 295 K. Experimental values of the ac conductivity depended on the frequency. The observed conductivity increased with increasing frequency. To compare the magnitude of ac and dc conductivities, the low frequency limiting value was needed. However, the appropriate function to express the frequency dependence of the ac conductivity data could not be found. The frequency dependence was in fact very weak below 1 kHz. Therefore, the value at the lowest frequency in this measurement was compared with the dc data. The reported value of the dc conductivity is 2×10^{-3} S m^{-1} at 295 K [3]. The experimental value measured by the ac method at 20 Hz, 2.4×10^{-2} S m^{-1}, is one order of magnitude larger than that of the dc method. DC and AC measurements of the conductivity often give different values. They may well be measuring different processes such as those involving electric contact potentials and grain boundary effects [6].

The temperature dependence of the ac conductivity at 20 Hz is shown in Fig. 4-6. In the room temperature phase, positive slope of the conductivity with increasing temperature can be accepted as an indication of semiconductivity. A drastic change occurred at the 229.4 K phase transition. The conductivity decreased by about four orders of magnitude. The observed behavior agreed with the results of the dc conductivity measurement [3].

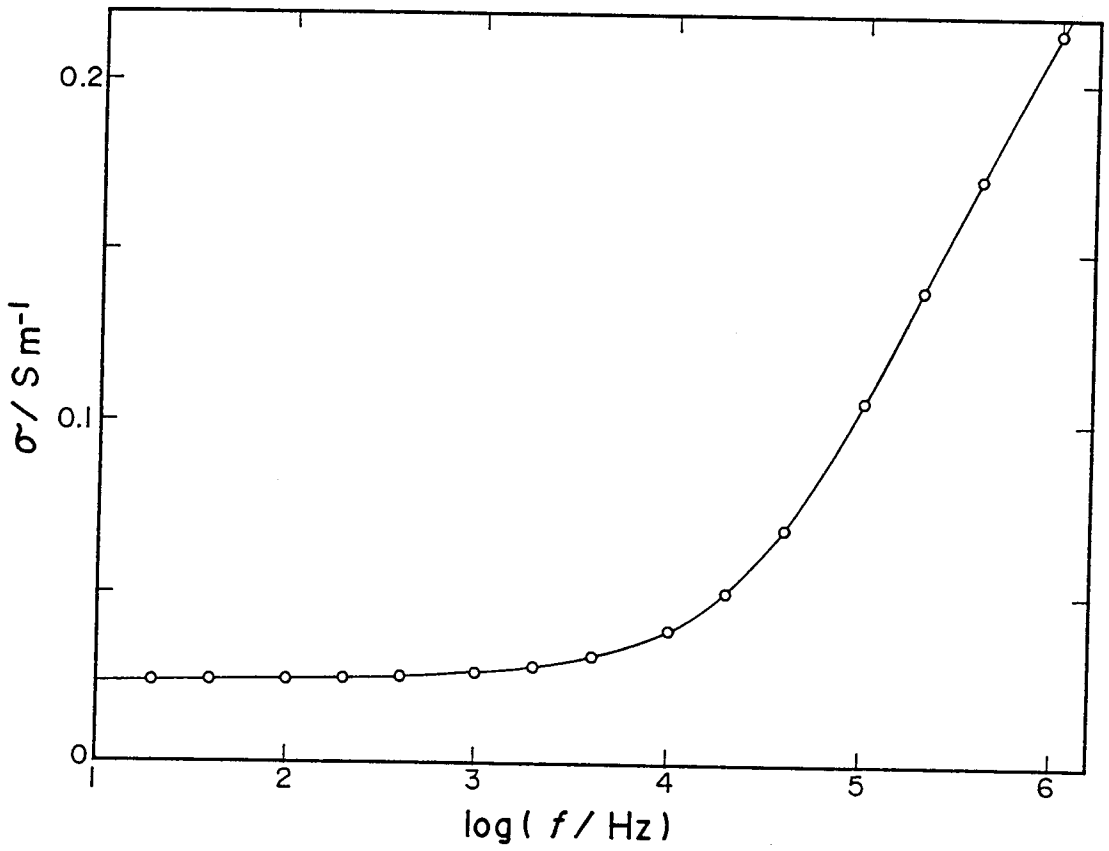

Fig. 4-5 Frequency dependence of the ac conductivity of $CH_3NH_3SnBr_3$ at 295 K.

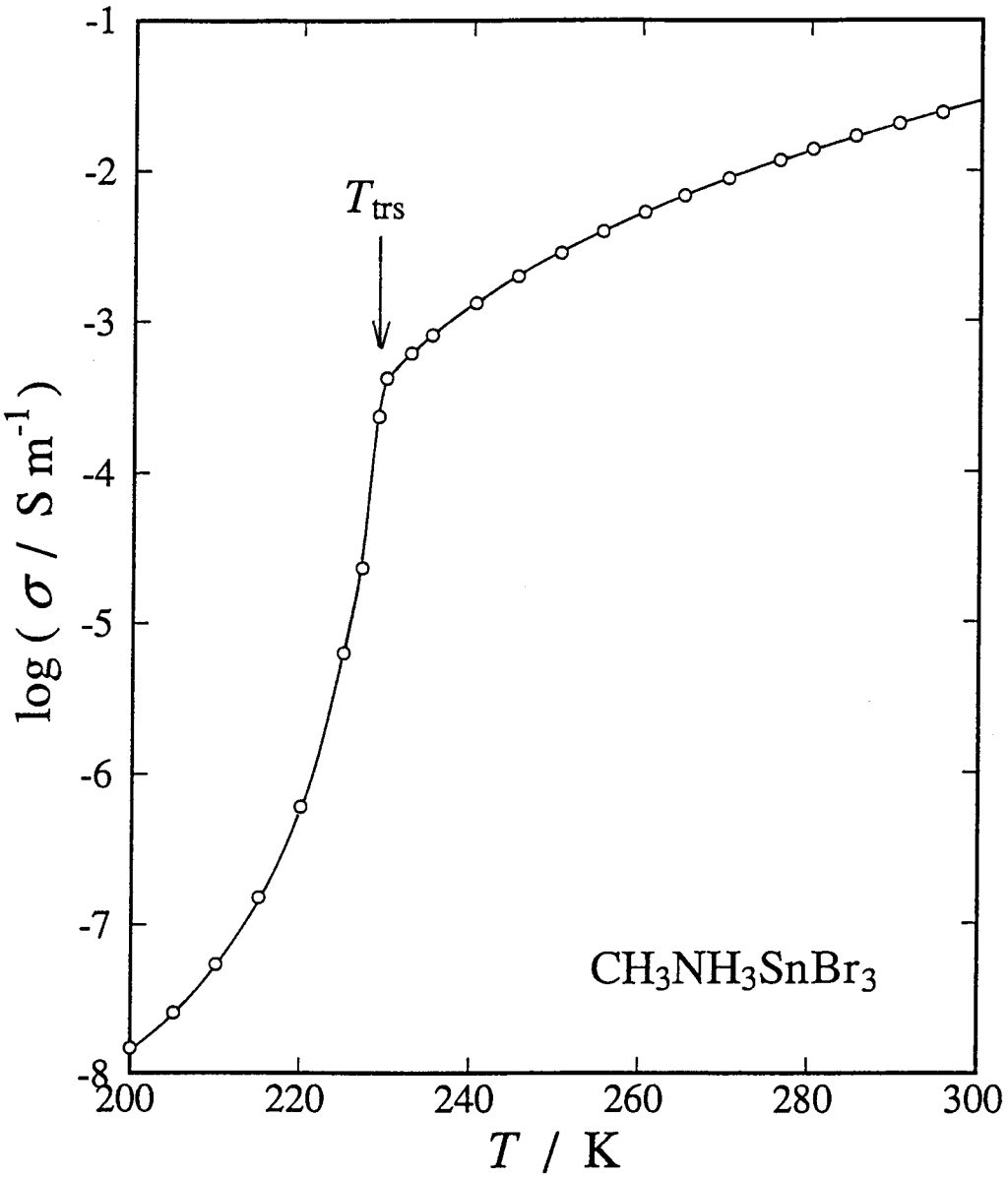

Fig. 4-6 Temperature dependence of the ac conductivity of $CH_3NH_3SnBr_3$ at 20 Hz.

Figure 4-7 shows the Arrhenius plot of the ac conductivity measured at 20 Hz in the highest temperature phase. The activation energy of 29.1 kJ mol^{-1} was obtained by linear approximation using the experimental data above 245 K. It agrees very well with that derived from the dc measurement, 0.31 eV (= 30 kJ mol^{-1}) [3].

4.4 Dielectric Permittivity

4.4.1 Complex Permittivity

Figure 4-8 shows the real(upper) and imaginary(lower) parts of the dielectric permittivity below 170 K measured in the heating direction. Symbols ○△□▽◇ denote the data taken at frequencies of 40 Hz, 1 kHz, 10 kHz, 100 kHz and 1 MHz, respectively. The arrow represents the temperature of the phase transition. As seen in the figure, a dielectric dispersion occurred below 150 K. The dielectric loss peaks shifted toward lower temperature and became smaller with decreasing frequency. The rapid increases in ε' and ε'' which were observed in the high temperature range ($T \geq 140$ K) can be regarded as a precursory effect of the phase transition at 229.4 K. The dielectric behavior was not influenced by the phase transition at 46.0 K.

4.3.2 Dielectric Dispersion

The relaxation time of the motion related to the dielectric dispersion was calculated by using the relation

$$\tau = 1 / (2\pi f_{max}), \qquad (4\text{-}1)$$

where f_{max} is the frequency of the maximum ε'' at each tempera-

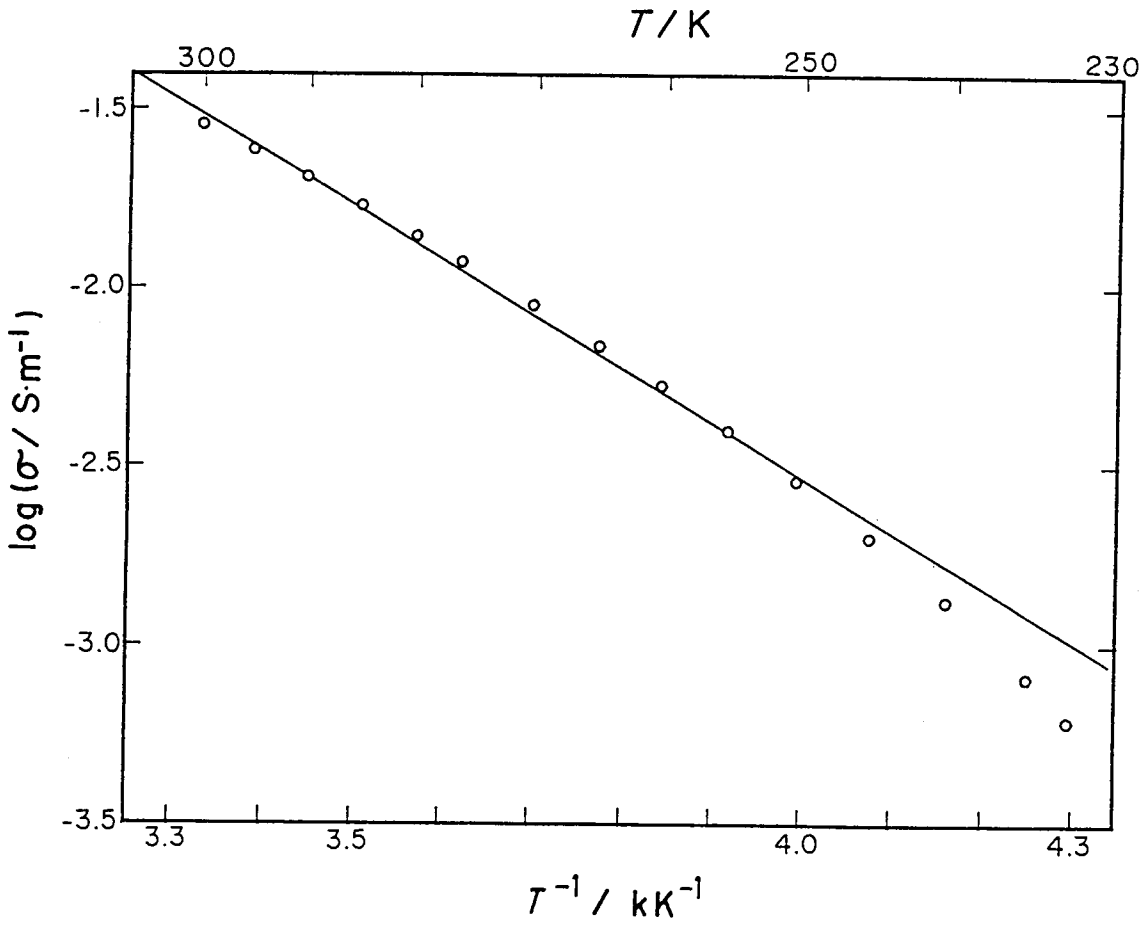

Fig. 4-7 Arrhenius plots of the ac conductivity of $CH_3NH_3SnBr_3$.

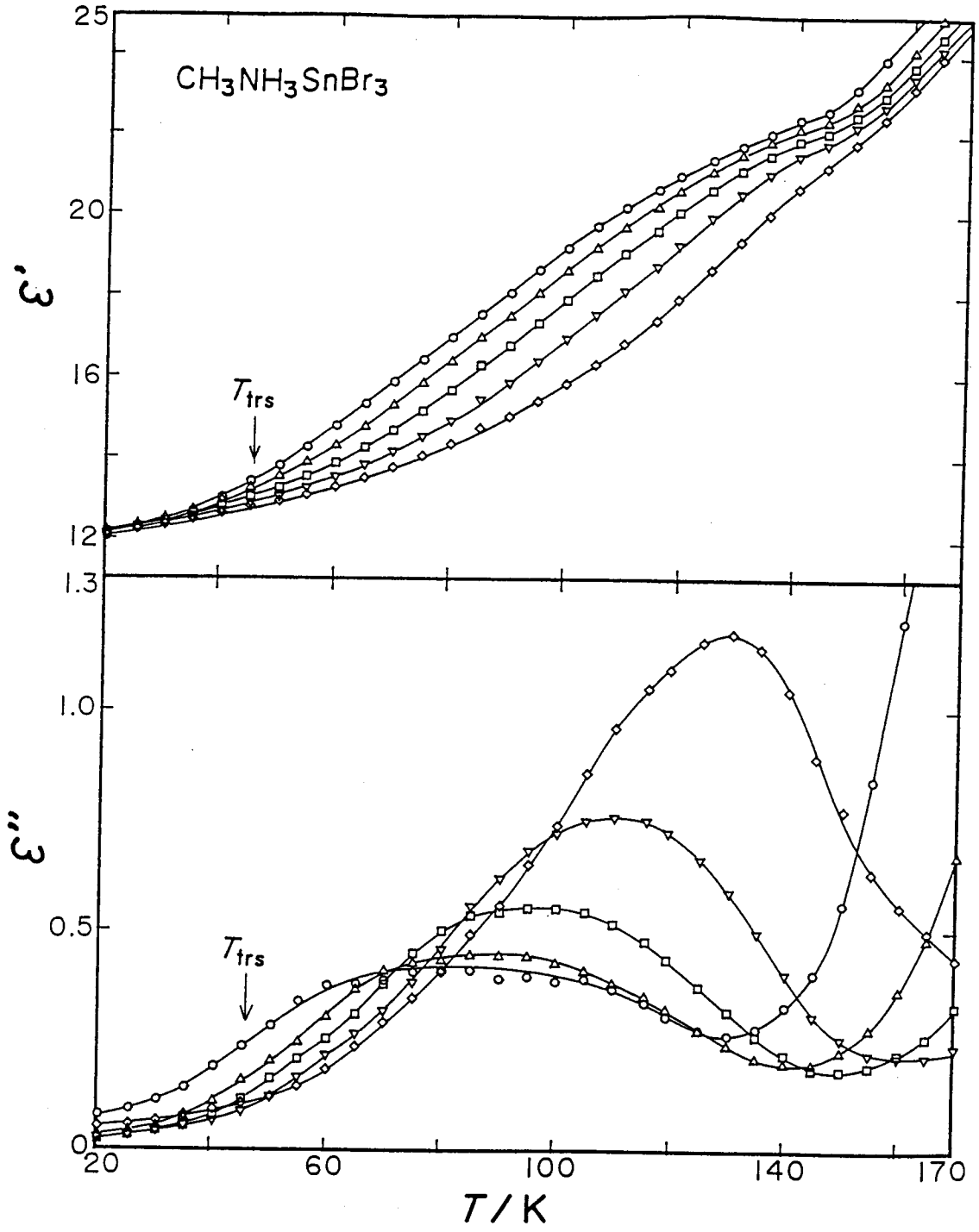

Fig. 4-8 Temperature dependence of ε′ (upper) and ε″ (lower) of $CH_3NH_3SnBr_3$.

○: 40 Hz, △: 1k Hz, □: 10k Hz, ▽: 100k Hz, ◇: 1M Hz.

ture. Figure 4-9 shows the Arrhenius plot of the relaxation time. The activation energy obtained from the plot is 10.5 kJ mol^{-1}. The temperature at which the relaxation time becomes comparable with the calorimetric experimental time ($\sim 10^3$ s) was estimated to be 37.0 K. However, no glass transition was found at the temperature in the heat capacity measurement. The magnitude of the enthalpy relaxation associated with the molecular motion may be too small to be detected as a glass transition in the heat capacity measurement. The dielectric dispersion may be related to the phase transitions at higher temperatures. As one can see in Figures 4-1 and 4-3, the phase transition at 188.6 K is of the first order but it has a precursory effect of considerable magnitude below the transition temperature. If the molecular disorder associated with the transition involves movement of the polar cation, which is likely to be the case, then one should expect a temperature-dependent dielectric response in the temperature region where $\Delta_{trs}S$ increases gradually with increasing temperature (see Fig. 4-3).

Figure 4-10 shows the complex permittivity loci at three different temperatures. The curves in the figure show the Cole-Cole arcs determined by the non-linear least squares method using the following equation. The complex permittivity ε is described by the Cole-Cole equation

$$\varepsilon = \varepsilon_\infty + \frac{\varepsilon_0 - \varepsilon_\infty}{1 + (i\omega\tau)^{\alpha}} \quad . \qquad (4\text{-}2)$$

Here, ε_0 and ε_∞ are the permittivities at zero and infinite frequencies and α the distribution factor of the relaxation

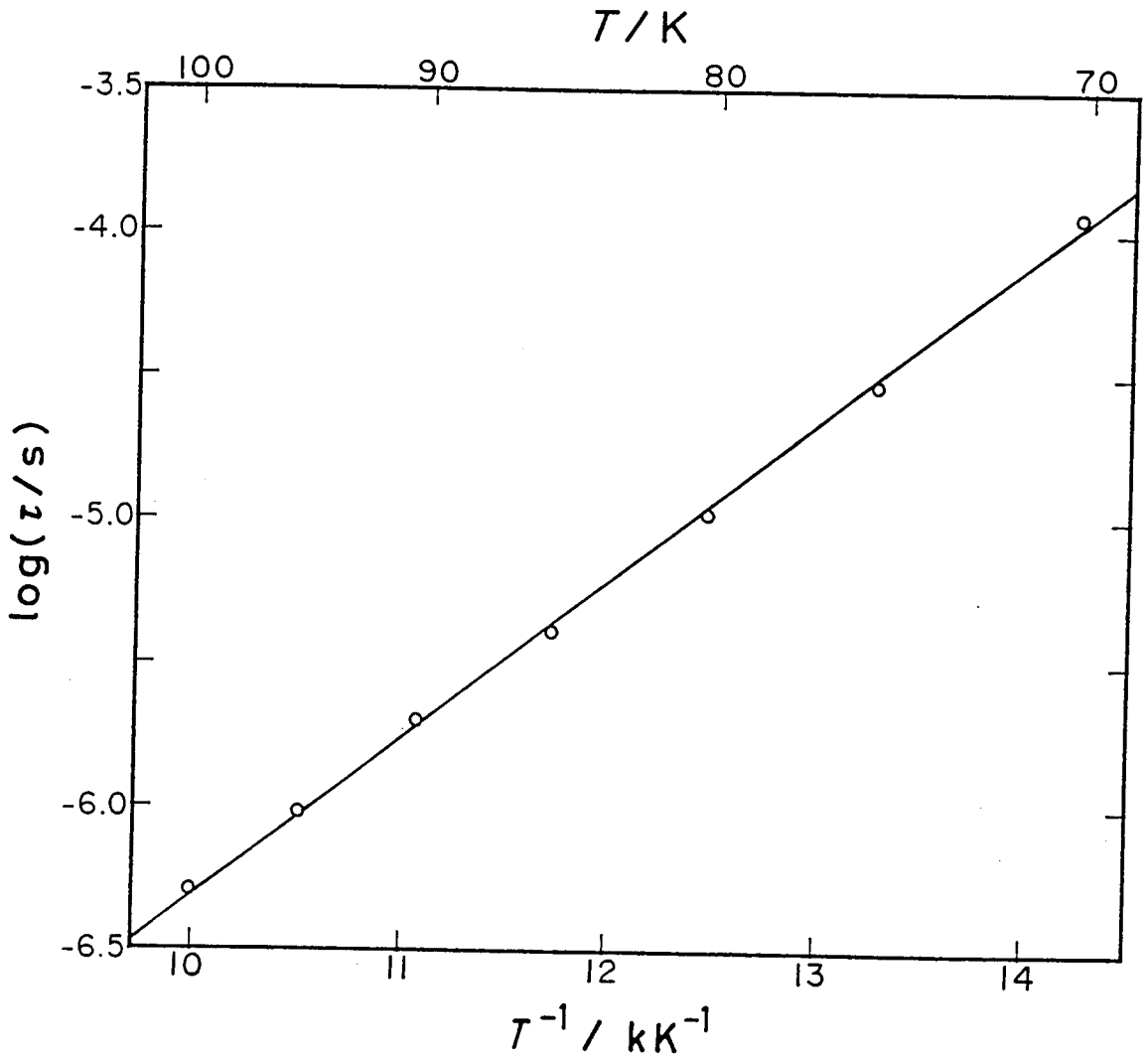

Fig. 4-9 Arrhenius plots of the dielectric relaxation time.

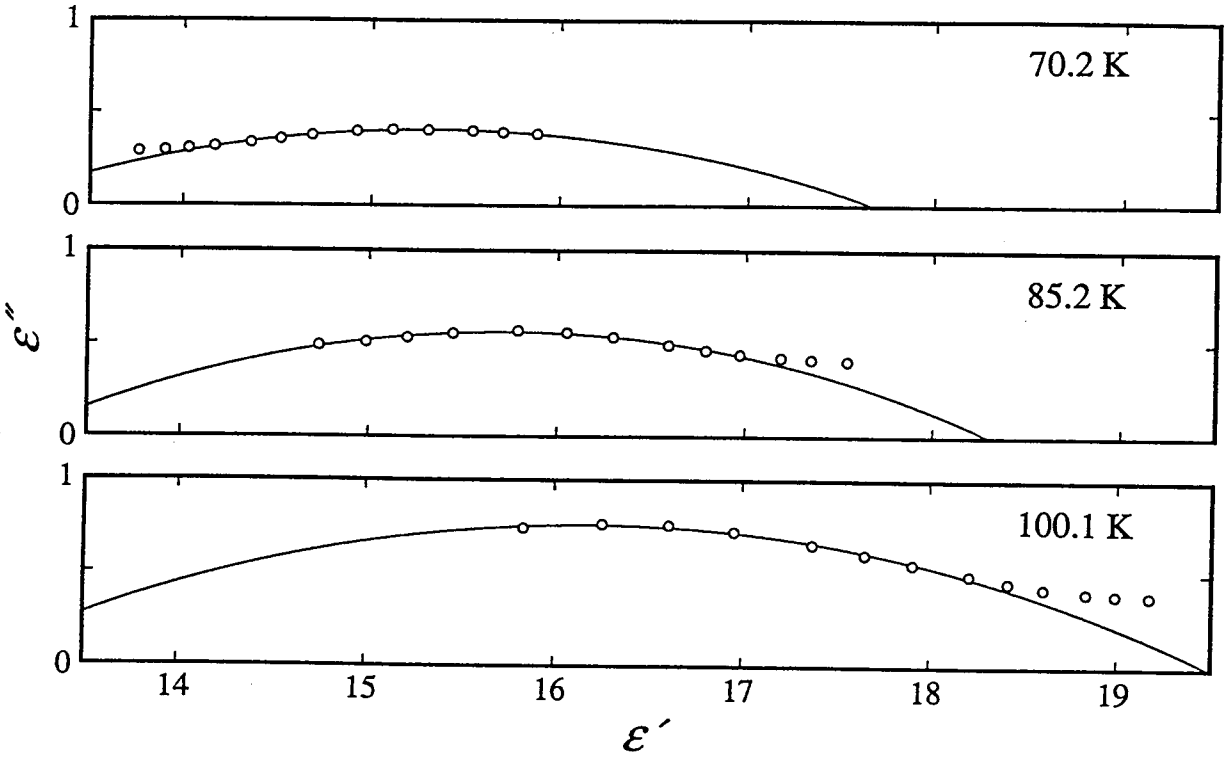

Fig. 4-10 Complex permittivity loci of $CH_3NH_3SnBr_3$.

times. The parameter α is equal to one for a system characterized by a single relaxation time. The loci deviate markedly from ideal Debye semicircles. The temperature dependence of α and $(\varepsilon_0 - \varepsilon_\infty)$ is shown in Fig. 4-11. The value of α (0.2 ~ 0.3) indicates that the present system departs considerably from a single relaxation process and that, if one attaches a significance to the slight decrease of α at the lower temperatures, the departure becomes stronger as the temperature is lowered. The values of $(\varepsilon_0 - \varepsilon_\infty)$ decrease with decreasing temperature. This indicates that the number of dipoles which are able to respond to the external electric field decreases with decreasing temperature. The result supports the mechanism of the dielectric dispersion discussed above that the dielectric dispersion is related to the partial disorder which persists widely below the transition temperature. Broad complex permittivity loci have also been found in some clathrate compounds including manganese squarate clathrate compound $(MnC_4O_4 \cdot 2H_2O)_3 \cdot CH_3COOH \cdot H_2O$ [7], zinc squarate clathrate compound $(ZnC_4O_4 \cdot 2H_2O)_3 \cdot CH_3COOH \cdot H_2O$ (in the triclinic form) [7], and tetrahydrofuran clathrate hydrate $THF \cdot 17H_2O$ [8].

4.5 High Pressure DTA

4.5.1 Pressure Dependence of the DTA Curves

Figure 4-12 shows the experimental DTA curves of $MASnBr_3$ observed at atmospheric (0.1 MPa) and high pressures (74.0 and 71.0 MPa). The curves (A) and (B) were obtained by using helium gas as the pressure medium and the curve (C) by nitrogen gas. The heating rate was 1.0-1.2 K min^{-1} for the low temperature transition region and 1.8-2.0 K min^{-1} for the one at the higher

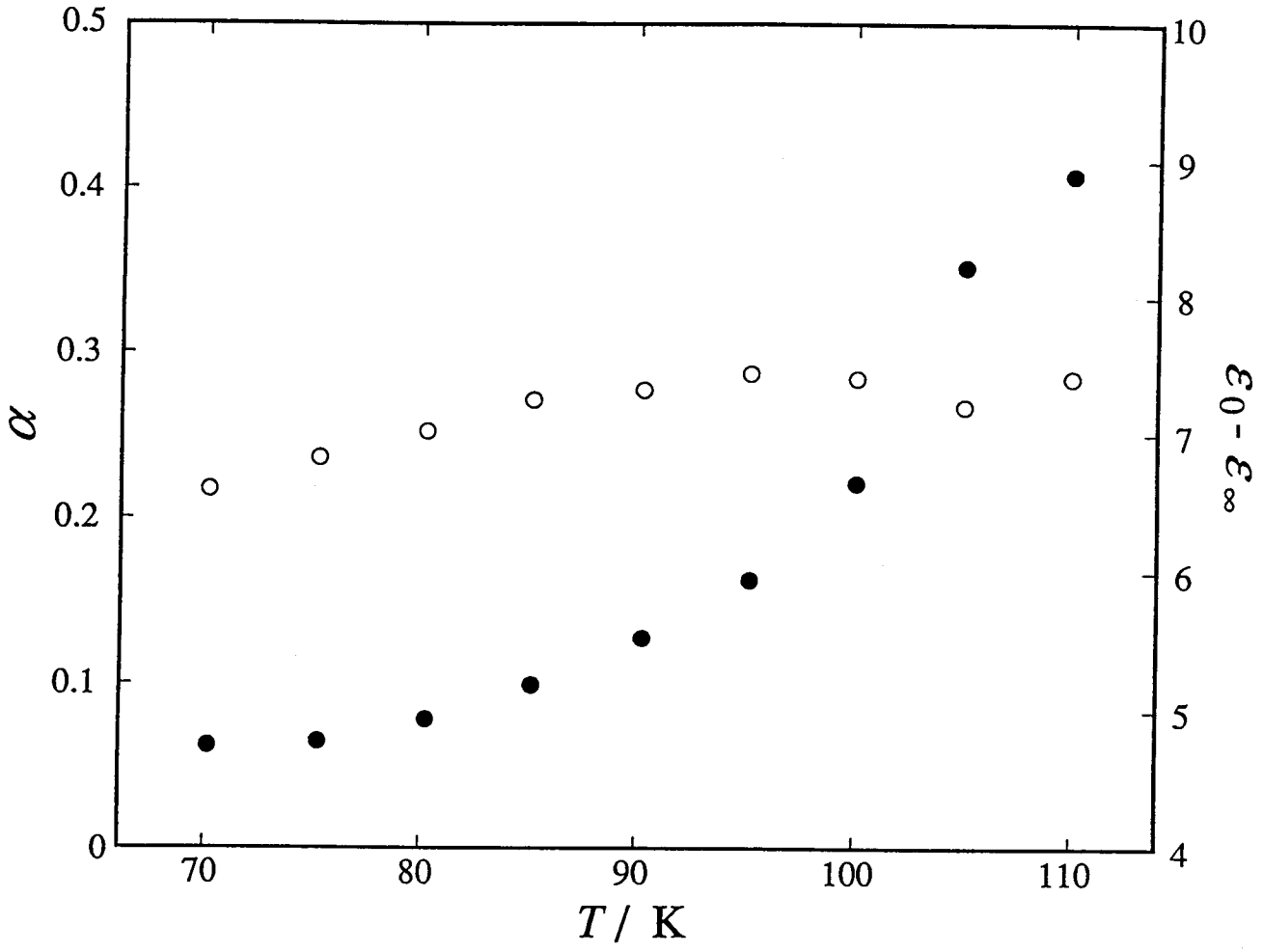

Fig. 4-11 Temperature dependences of the distribution factor α of the dielectric relaxation times and the difference between the permittivities at zero and infinite frequencies $\varepsilon_0 - \varepsilon_\infty$.

○: α, ●: $\varepsilon_0 - \varepsilon_\infty$.

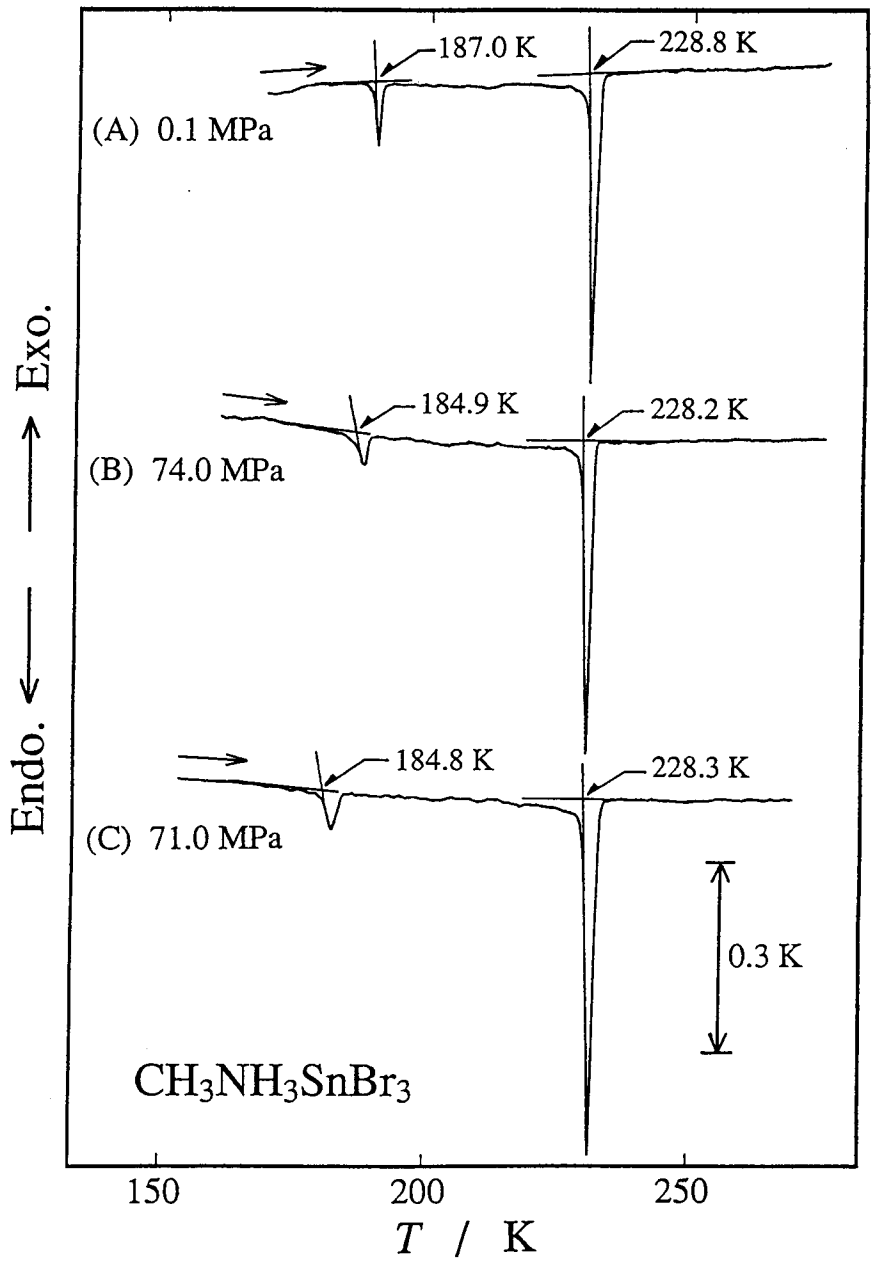

Fig. 4-12 DTA curves of $CH_3NH_3SnBr_3$ under pressures. The curves (A) and (B) were obtained by using He gas as the pressure transmitting medium and (C) by N_2 gas.

temperature. At atmospheric pressure (0.1 MPa), two endothermic peaks were observed at 187.0 K and 228.7 K. These temperatures agreed satisfactory with those obtained in the heat capacity measurement (188.2 K and 229.4 K). The phase transition observed at 213.0 K in the heat capacity measurement at 0.1 MPa was not observed in the DTA experiment. With increasing pressure, the peak at the higher temperature shifted slightly to lower temperatures. The one at the lower temperature also shifted to lower temperatures with increasing pressure upto ~50 MPa. Above the pressure, the peak occurred at the same temperature to within ± 0.3 K. The shape and area of both peaks did not change significantly in the whole pressure range. Effect of the He gas that might dissolve in the sample was suspected for the non-linear behavior. However, the same result was obtained with nitrogen as the pressure medium, as indicated by the curves (B) and (C). This indicates that the behavior is inherent to the sample property. The peak areas in the curve (C) are larger than those in the curve (B). This is due to the higher thermal conductivity of He than N_2 gas.

4.5.2 Pressure-Temperature Phase Relation

The volume changes associated with the transition were derived from the pressure dependence of the transition temperature dT_{trs}/dp determined in this measurement and the transition entropy $\Delta_{trs}S$ determined from the calorimetry at atmospheric pressure (from Table 4-3) by using the Clausius-Clapeyron's equation (Eq. 3-11). They are -0.123 $cm^3\ mol^{-1}$ and -0.698 $cm^3\ mol^{-1}$ for the high and low temperature transitions, respectively. Here the

gradient at 0.1 MPa was used as the dT_{trs}/dp value. These values are quite small (0.1 % for the former and 0.6 % for the latter) as compared with the molar volume (124 cm^3).

Figure 4-13 depicts the pressure-temperature phase diagram of the $MASnBr_3$ crystal. Open symbols represent the data obtained by using helium gas medium and closed ones by nitrogen gas. The phase boundary between the high and intermediate temperature phases is essentially a straight line with negative slope (-6.5×10^{-3} K MPa^{-1}). The one at the lower temperature is downward convex below 50 MPa and essentially horizontal above that as noted already. The horizontal phase boundary indicates no volume change at the phase transition. It is interpreted that the phase boundary is parallel to the *p*-axis above 50 MPa in three-dimensional space with pressure *p*, temperature *T* and free energy *G* as coordinate axes. As the phase boundary is traversed from the low temperature side, the molar volume decreases at both the phase transitions (below 50 MPa for the lower temperature one). The molar volume reduction was also found in $MAPbX_3$ (X = Cl, Br, I) as the crystal undergoes the phase transition from the partially ordered tetragonal phase to the fully disordered cubic phase (see Section 5.2 in Chapter 3). For $MASnBr_3$, the crystal structure is known only for the cubic phase. Structural study of the low temperature phases is desirable.

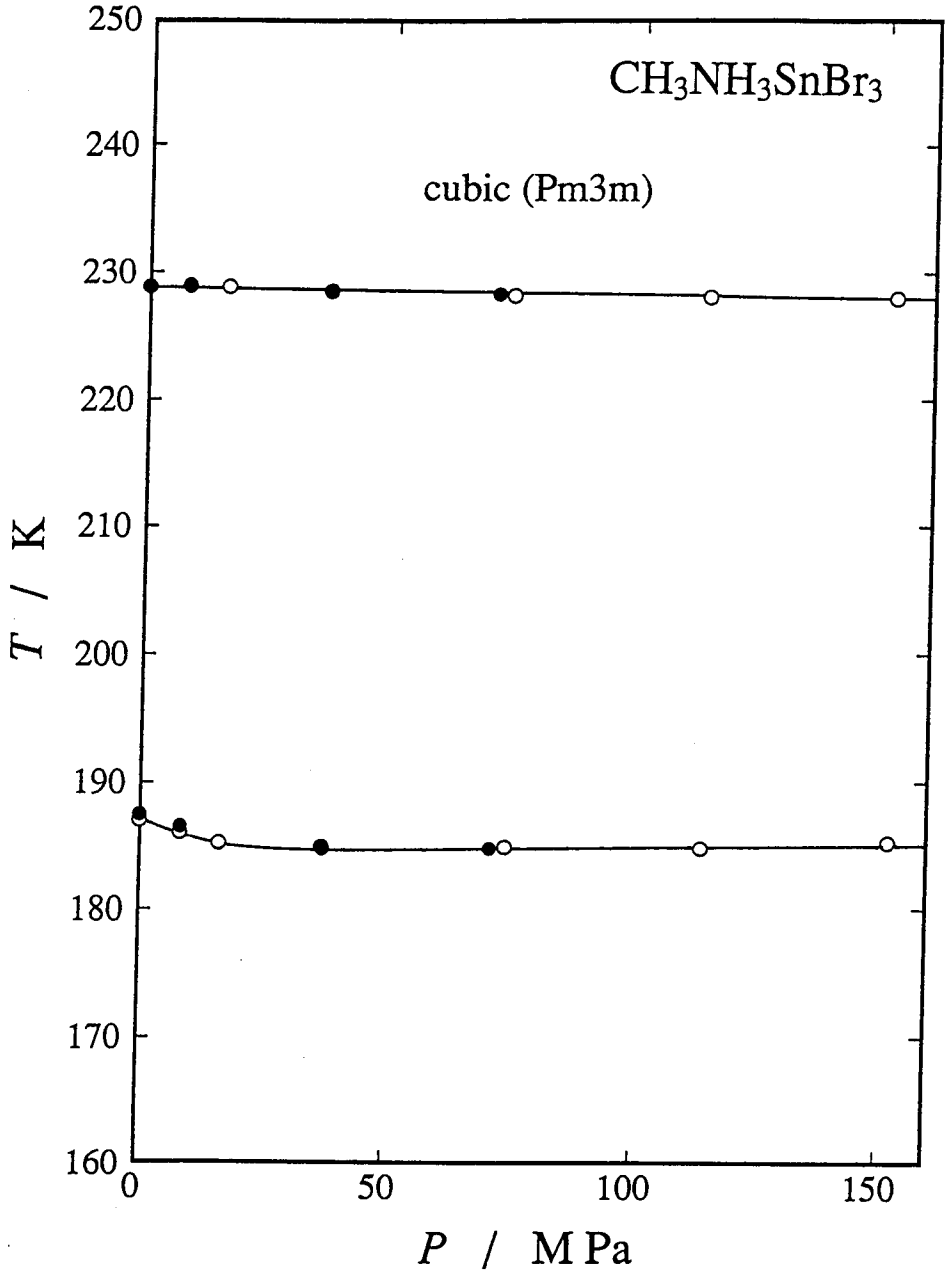

Fig. 4-13 *P-T* phase diagram of $CH_3NH_3SnBr_3$ crystals.

References to Chapter 4

1. D. Weber, *Z. Naturforsch.*, 33b, 862 (1978).
2. K. Yamada, S. Nose, T. Umehara, T. Okuda and S. Ichiba, *Bull. Chem. Soc. Jpn.*, 61, 4265 (1988).
3. K. Yamada, H. Kawaguchi, T. Matsui, T. Okuda and S. Ichiba, *Bull. Chem. Soc. Jpn.*, 63, 2521 (1990).
4. Y. Furukawa and D. Nakamura, *Z. Naturforsch.*, 44a, 1122 (1989).
5. R. Ikeda, Y. Kume and D. Nakamura, *J. Magn. Reson.*, 24, 9 (1976).
6. A. Hamnett, *Solid State Chemistry*, A. K. Cheetham and P. Day, editors. Oxford Science Publication, Chapt. 8 (1988).
7. Y. Miyazaki, Master's Thesis. Osaka University (1990).
8. S. R. Gough, R. E. Hawkins, B. Morris and D. W. Davidson, *J. Phys. Chem.*, 77, 2969 (1973).

Chapter 5

$CH_3NH_3SnI_3$

5.1 Introduction

$MASnI_3$ crystallizes in the cubic perovskite structure [1]. The crystal is black with metallic luster and metallic in its conductivity [1,2]. A phase transition was found at 273 K by DTA study [2]. However, absence of a quadrepole splitting at 85 K in the Mössbauer spectra of tin [1] suggested another possibility that the crystal retains cubic symmetry down to 85 K. This result raises an interesting question of whether the cubic crystal becomes ordered at low temperature by way of phase transitions with associated entropy decrease or remains cubic and become ultimately glassy at the lowest temperature.

The color and high conductivity can be interpreted by assuming a partly filled band structure [3]. The band model was proposed for $CsSnBr_3$ [4,5]. This perovskite type crystal is metallic in its conductivity and its tin Mössbauer spectrum shows a much smaller isomer shift than expected for an octahedrally coordinated Sn(II) ion [4]. The small isomer shift indicated low s-electron density at the Sn(II) nucleus. Donaldson *et al.* suggested that one or more of the nominally unfilled electron bands were populated from the Sn(II) $5s^2$ electrons [4,6]. For $MASnI_3$, a small isomer shift in the tin Mössbauer spectra was also found, and the donation of 0.07 s-electron into a conduction band was suggested [3].

The electrical property at the low temperature should be

noted. $CsSnBr_3$ shows metallic behavior over a wide temperature range [3]. No observable discontinuity was found in the conductivity though phase transitions occured at 85 K and 292 K [7]. In contrast, the conductivity of $CsSnI_3$ drastically changes from semiconducting to metallic at the 425 K phase transition where the structural change from orthorhombic to slightly distorted tetragonal perovskite occurs [2,3]. On the other hand, the conductivity of $MASnBr_3$ which is semiconducting in the room temperature phase drastically decreases at the 233 K phase transition where ordering of orientationally disordered MA ion occurs (see Chapter 4). DC conductivity of $MASnI_3$ has already been measured at temperatures between 85 and 300 K [3]. The conductivity slightly increases with decreasing temperature. No apparent discontinuity was found in the observed temperature range.

As was described in Chapter 2, two types of $MASnI_3$ samples were accidentally obtained in this study, although the reaction condition responsible for the formation of each sample cannot be identified. One sample underwent a phase transition at 272 K ($MASnI_3$(T)) and the other a glass transition at around 130 K ($MASnI_3$(G)) (see Section 3.1 in this chapter).

The purpose of this work is to investigate the ordering process of orientationally disordered MA ion and electrical property at low temperatures, based on the new experimental observiation on the two types of samples. For this purpose, powder X-ray diffraction (Section 2), adiabatic calorimetry (Section 3), and dc conductivity measurement (Section 4) were carried out for both the samples. Powder X-ray diffraction was taken at room temperature to distinguish the structures of the

two samples. Heat capacity measurement revealed different thermal behavior. DC conductivity measurement was extended to lower temperature (down to 6 K). A clear difference in the temperature dependence of the conductivities between the two samples was revealed. The effect of the ordering of disordered MA ion was also discussed. A high pressure DTA measurement (describes in Section 5) was carried out for $MASnI_3(T)$ at pressures between 0.1 and 160 MPa in order to investigate the pressure-temperature phase relation and compare it with that of $MAPbX_3$. Complicated *p-T* phase diagram containing two triple points and metastable phase boundary was obtained. The measurement was not carried out for $MASnI_3(G)$ because of the sensitivity limitation.

5.2 X-ray Powder Diffraction

5.2.1 Powder Patterns of $MASnI_3(T)$ and $MASnI_3(G)$.

Figure 5-1 shows the X-ray powder diffraction patterns of $MASnI_3(T)$ (in (A)) and $MASnI_3(G)$ (in (B)) observed at room temperature. There is no significant difference between the two diffraction patterns. They were indexed successfully on a cubic perovskite structure (space group Pm3m). Thus, no structural difference was recognized between $MASnI_3(T)$ and $MASnI_3(G)$ on the basis of the diffraction pattern.

5.2.2 Low Temperature Pattern of $MASnI_3(T)$.

As will be described in Section 3.1 in this Chapter, $MASnI_3(T)$ undergoes a phase transition at 272.3 K. The X-ray powder diffraction pattern of $MASnI_3(T)$ recorded at 230 K is shown in Fig. 5-2 (B). Some peaks apparently split and new peaks

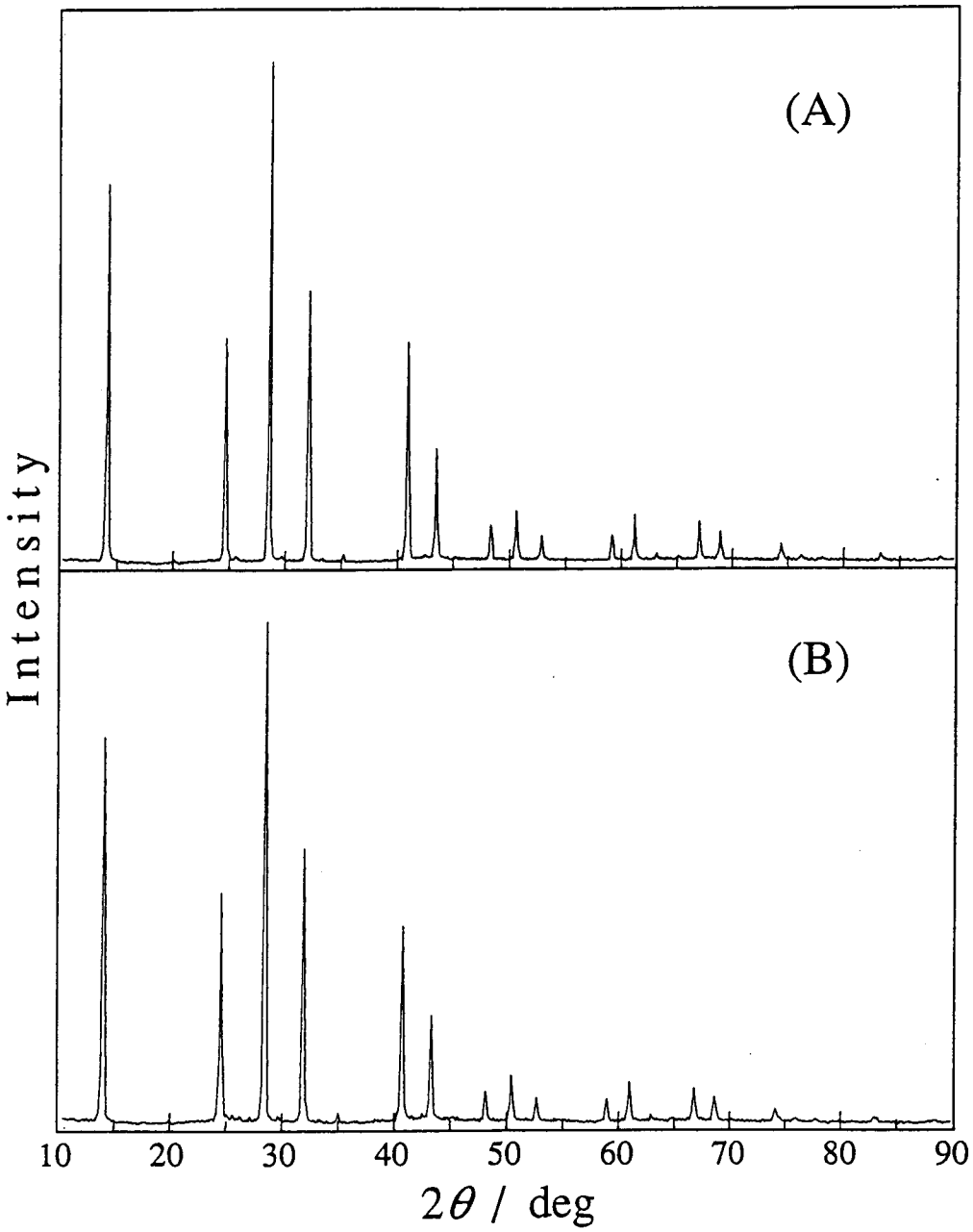

Fig. 5-1 X-ray powder diffraction patterns of $CH_3NH_3SnI_3$.
(A): $CH_3NH_3SnI_3$(T), (B): $CH_3NH_3SnI_3$(G).

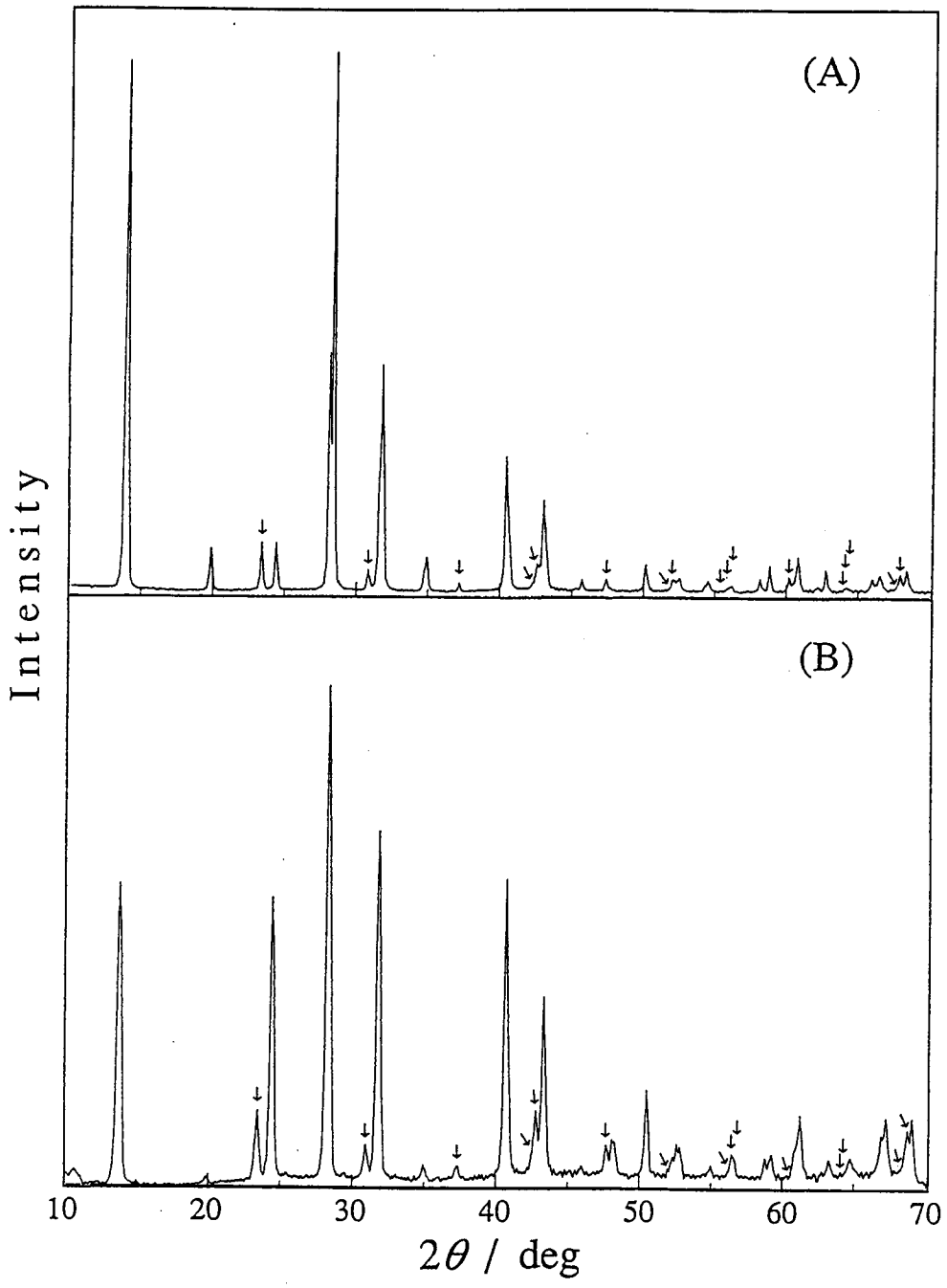

Fig. 5-2 X-ray powder diffraction patterns of $CH_3NH_3PbI_3$ and $CH_3NH_3SnI_3$(T).
(A): observed at room temperature for $CH_3NH_3PbI_3$.
(B): observed at 230 K for $CH_3NH_3SnI_3$(T).
Diffraction peaks due to Cu Kα_2 radiation have been removed by computation.

appeared. This pattern resembles that of $MAPbI_3$ taken at room temperature reproduced in Fig. 5-2 (A). In this figure, diffraction peaks due to Cu Kα_2 radiation are removed by computation. To facilitate comparison, peak positions are shown in Fig. 5-3 by lines. $MAPbI_3$ crystal has the tetragonal I4/mcm structure at room temperature [8]. The arrows in Fig 5-2 (A) indicate the peaks due to the larger unit cell of this structure ($\sqrt{2}$ x $\sqrt{2}$ x 2 times the ideal perovskite unit cell). Corresponding peaks were found in the pattern of $MASnI_3$(T) (Arrows in Fig. 5-2 (B) indicate them). Therefore, it is probable that $MASnI_3$(T) has the same structure as that of the room temperature phase of $MAPbI_3$ (tetragonal I4/mcm).

5.3 Heat Capacity

5.3.1 Heat Capacity of $MASnI_3$(T) and $MASnI_3$(G)

The numerical values of the molar heat capacity of $MASnI_3$(T) and $MASnI_3$(G) are given in Table 5-1 and 5-2, respectively. They are reproduced graphically in Fig. 5-4. The dotted curve represents the normal heat capacities for $MASnI_3$(T) determined as described below.

In $MASnI_3$(T), five heat-capacity anomalies were found at 98.5 K, 109.4 K, 114.7 K, 150.5 K and 272.3 K. The last one corresponds to the DTA peak reported by Yamada *et al.* [2]. The other four are observed here for the first time. As is apparent from Fig. 5-4, four anomalies at the low temperatures are considerably smaller than that at 272.3 K and they overlap each other. The phase transition at 150.5 K is of the higher order and the others are of the first order. The highest temperature transi-

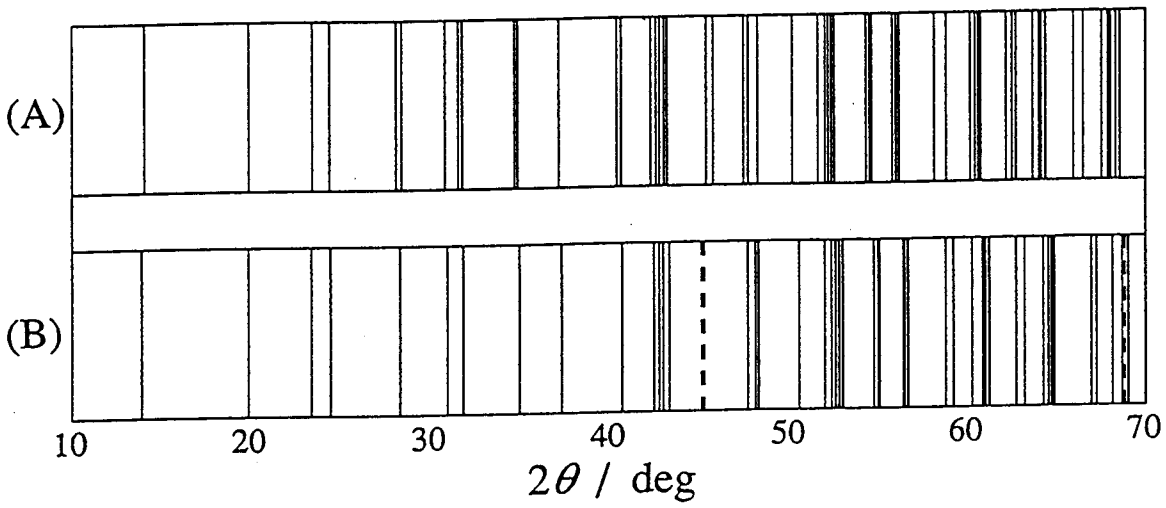

Fig. 5-3 Peak positions of the X-ray powder diffraction patterns.
(A): observed at room temperature for $CH_3NH_3PbI_3$.
(B): observed at 230 K for $CH_3NH_3SnI_3$(T).
Broken lines indicate ambiguous peaks.

Table 5-1 Molar heat capacity of $CH_3NH_3SnI_3$(T).

T_{av} / K	C_p / J K^{-1}mol^{-1}	T_{av} / K	C_p / J K^{-1}mol^{-1}	T_{av} / K	C_p / J K^{-1}mol^{-1}	T_{av} / K	C_p / J K^{-1}mol^{-1}	T_{av} / K	C_p / J K^{-1}mol^{-1}	T_{av} / K	C_p / J K^{-1}mol^{-1}
12.12	19.60	51.61	107.6	109.50	197.3	163.21	162.7	258.33	188.5	274.07	178.8
12.77	21.60	52.62	108.8	110.20	188.9	165.31	163.0	259.88	189.5	274.41	177.6
13.49	24.07	53.65	110.0	110.90	186.1	166.06	163.1	261.18	190.3	274.82	177.1
14.26	26.70	54.69	111.3	111.60	183.2	168.21	163.4	262.24	191.0	275.28	176.4
15.00	29.06	55.75	112.4	112.31	179.2	170.36	163.8	263.29	192.1	275.79	175.8
15.75	31.41	56.90	113.6	113.02	176.8	172.50	164.2	264.34	192.9	276.36	175.4
16.50	33.76	58.17	114.9	113.73	177.3	174.65	164.7	265.39	193.9	276.99	174.8
17.25	36.06	59.81	116.5	114.44	177.9	176.80	165.0	266.44	195.4	277.68	174.6
17.98	38.37	61.55	118.2	115.14	178.1	178.95	165.5	267.48	197.0	278.42	174.2
18.67	40.52	63.38	119.8	115.85	176.5	181.09	166.1	268.25	198.5	279.22	174.0
19.33	42.54	65.30	121.6	116.55	174.0	183.22	166.5	268.73	199.4	280.08	173.6
20.00	44.61	67.26	123.2	117.00	171.5	185.34	167.0	269.22	200.8	280.99	173.5
20.65	46.53	69.26	124.8	117.92	167.3	187.45	167.4	269.59	202.0	281.96	173.1
21.28	48.29	71.33	126.5	118.84	164.5	189.55	167.9	269.85	202.7	282.99	173.0
21.90	50.04	73.47	128.1	119.76	163.1	191.65	168.4	270.12	204.3	284.08	172.7
22.53	51.84	75.64	129.8	121.08	162.1	193.73	169.0	270.34	204.7	285.22	172.6
23.20	53.64	77.84	131.5	122.78	161.4	195.81	169.4	270.53	205.8	286.27	172.6
23.91	55.59	80.10	133.3	124.52	161.1	197.88	170.0	270.71	207.0	288.27	172.4
24.65	57.59	82.42	135.1	126.30	160.9	199.98	170.4	270.88	208.1	290.27	172.3
25.41	59.56	84.77	137.0	128.06	160.8	202.11	170.9	271.03	209.2	292.28	171.8
26.17	61.53	86.68	138.7	129.81	160.9	204.24	171.4	271.16	210.2	294.33	171.8
26.94	63.44	88.15	140.0	131.55	161.0	206.38	171.9	271.29	211.5	296.43	171.7
27.72	65.35	89.60	141.4	133.29	161.1	208.51	172.6	271.41	213.1	298.55	171.5
28.49	67.22	91.03	142.9	135.02	161.3	210.63	173.1	271.54	214.7	300.67	171.3
29.27	69.07	92.44	144.5	136.74	161.5	212.76	173.5	271.66	216.9	302.84	171.2
30.15	71.09	93.83	146.2	138.45	161.8	214.88	174.1	271.78	219.9	305.01	171.1
31.11	73.27	95.13	148.6	140.15	162.0	217.00	174.8	271.90	225.2	307.13	171.2
32.07	75.39	96.27	151.8	141.85	162.3	219.12	175.2	272.00	240.6	309.25	171.2
33.02	77.46	97.08	156.6	143.18	162.5	221.27	175.8	272.10	276.1	311.01	171.3
33.96	79.43	97.63	166.1	144.16	162.7	223.46	176.4	272.20	310.6	313.04	171.3
34.90	81.33	98.06	180.9	145.14	163.0	225.64	177.0	272.29	333.0	315.11	171.4
35.83	83.16	98.38	191.9	146.12	163.2	227.82	177.6	272.38	322.8	317.20	171.5
36.76	84.98	98.70	183.0	147.10	163.4	230.81	178.6	272.47	297.4	319.29	171.5
37.68	86.13	99.03	163.8	148.07	163.7	235.49	179.9	272.57	271.1	321.53	171.6
38.60	88.36	99.37	153.9	149.04	164.1	237.05	180.5	272.67	252.0	323.92	171.7
39.57	90.03	99.71	151.3	150.00	164.5	238.61	181.0	272.77	238.9	326.32	171.6
40.60	91.73	100.11	150.6	150.97	164.5	241.15	181.6	272.86	231.1	328.72	171.6
41.61	93.40	100.86	151.0	151.93	164.3	242.72	182.0	272.96	224.5	331.13	171.6
42.59	94.96	101.90	152.0	152.89	163.7	244.29	182.5	273.06	216.4	333.54	171.5
43.57	96.44	102.93	153.1	153.85	163.2	245.86	183.1	273.16	208.1	335.94	171.6
44.54	97.93	103.96	154.5	154.81	162.7	247.43	183.6	273.26	201.0	338.34	171.6
45.53	99.40	104.97	156.4	155.77	162.4	248.99	184.2	273.35	197.0	340.74	171.5
46.55	100.9	105.86	160.2	156.73	162.3	250.55	184.9	273.45	193.7	343.13	171.5
47.56	102.3	106.61	165.9	157.68	162.1	252.11	185.5	273.55	189.7	345.52	171.7
48.55	103.7	107.35	172.2	158.64	162.2	253.67	186.1	273.65	184.0	347.95	171.9
49.56	105.0	108.08	177.6	159.59	162.2	255.23	186.9	273.75	180.6	350.42	171.7
50.59	106.3	108.80	188.5	161.11	162.4	256.78	187.7	273.87	179.6		

Table 5-2 Molar heat capacity of $CH_3NH_3SnI_3(G)$.

T_{av} / K	C_P / $J K^{-1} mol^{-1}$	T_{av} / K	C_P / $J K^{-1} mol^{-1}$	T_{av} / K	C_P / $J K^{-1} mol^{-1}$	T_{av} / K	C_P / $J K^{-1} mol^{-1}$	T_{av} / K	C_P / $J K^{-1} mol^{-1}$
11.97	18.66	39.43	89.84	84.06	141.9	149.31	167.7	227.23	177.1
12.69	20.84	40.23	91.36	85.81	143.1	151.05	168.0	229.33	177.2
13.33	22.81	41.06	92.90	87.59	144.2	152.83	168.4	231.43	177.6
13.97	24.79	41.89	94.41	89.39	145.4	154.63	168.8	233.53	176.9
14.60	26.77	42.72	95.86	91.23	146.5	156.43	169.1	235.63	176.7
15.29	28.82	43.58	97.34	93.09	147.6	158.23	169.5	237.73	176.9
16.02	31.02	44.46	98.89	94.95	148.7	160.27	169.9	239.88	176.9
16.75	33.23	45.37	100.4	96.83	149.7	162.42	170.3	242.06	176.9
17.51	35.45	46.28	101.9	98.75	150.7	164.60	170.8	244.24	177.0
18.23	37.66	47.22	103.4	100.14	151.5	166.78	171.1	246.42	176.5
18.93	39.74	48.19	104.9	101.79	152.2	168.95	171.4	248.60	176.3
19.63	41.87	49.11	106.3	103.46	153.1	171.13	171.8	250.79	176.2
20.34	44.05	49.98	107.6	105.13	153.7	173.33	172.2	252.97	176.1
21.06	46.03	50.89	108.9	106.78	154.4	175.57	172.6	255.16	176.1
21.77	47.97	51.83	110.3	108.42	155.1	177.81	172.9	257.35	175.9
22.46	49.90	52.78	111.6	110.06	155.7	180.04	173.3	259.53	175.8
23.15	51.79	53.74	112.9	111.68	156.3	182.27	173.6	261.76	175.7
23.84	53.65	54.79	114.3	113.30	156.9	184.39	173.9	264.03	175.7
24.54	55.59	55.90	115.8	114.96	157.5	186.40	174.2	266.29	175.5
25.25	57.51	57.06	117.2	116.65	158.1	188.41	174.6	268.56	175.5
25.98	59.35	58.25	118.7	118.34	158.6	190.41	174.9	270.83	175.4
26.71	61.26	59.44	120.1	120.02	159.1	192.41	175.0	273.09	175.4
27.43	63.10	60.61	121.5	121.70	159.6	194.41	175.3	275.36	175.4
28.15	64.87	61.82	122.7	123.37	160.2	196.41	175.5	277.63	175.3
28.87	66.67	63.04	123.9	125.07	160.9	198.41	175.7	279.90	175.2
29.60	68.40	64.22	125.1	126.80	161.4	200.41	176.0	282.10	175.0
30.33	70.24	65.45	126.3	128.53	162.0	202.42	176.2	284.23	175.1
31.06	72.00	66.79	127.6	130.24	162.6	204.47	176.4	286.35	175.2
31.80	73.69	68.18	128.9	131.96	163.1	206.54	176.5	288.48	175.3
32.55	75.45	69.62	130.3	133.66	163.7	208.62	176.7	290.60	175.2
33.30	77.14	71.10	131.6	135.37	164.2	210.69	176.7	292.71	175.1
34.05	78.84	72.62	133.0	137.50	164.8	212.74	177.0	294.83	175.1
34.81	80.46	74.18	134.4	138.80	165.1	214.76	177.0	296.95	175.1
35.57	82.09	75.77	135.6	140.56	165.6	216.78	177.1	299.06	175.0
36.34	83.73	77.40	136.9	142.32	166.0	218.83	177.1	301.18	174.9
37.13	85.37	79.01	138.2	144.07	166.5	220.93	177.1		
37.90	86.91	80.66	139.4	145.82	166.9	223.03	177.2		
38.67	88.42	82.35	140.7	147.57	167.2	225.13	177.1		

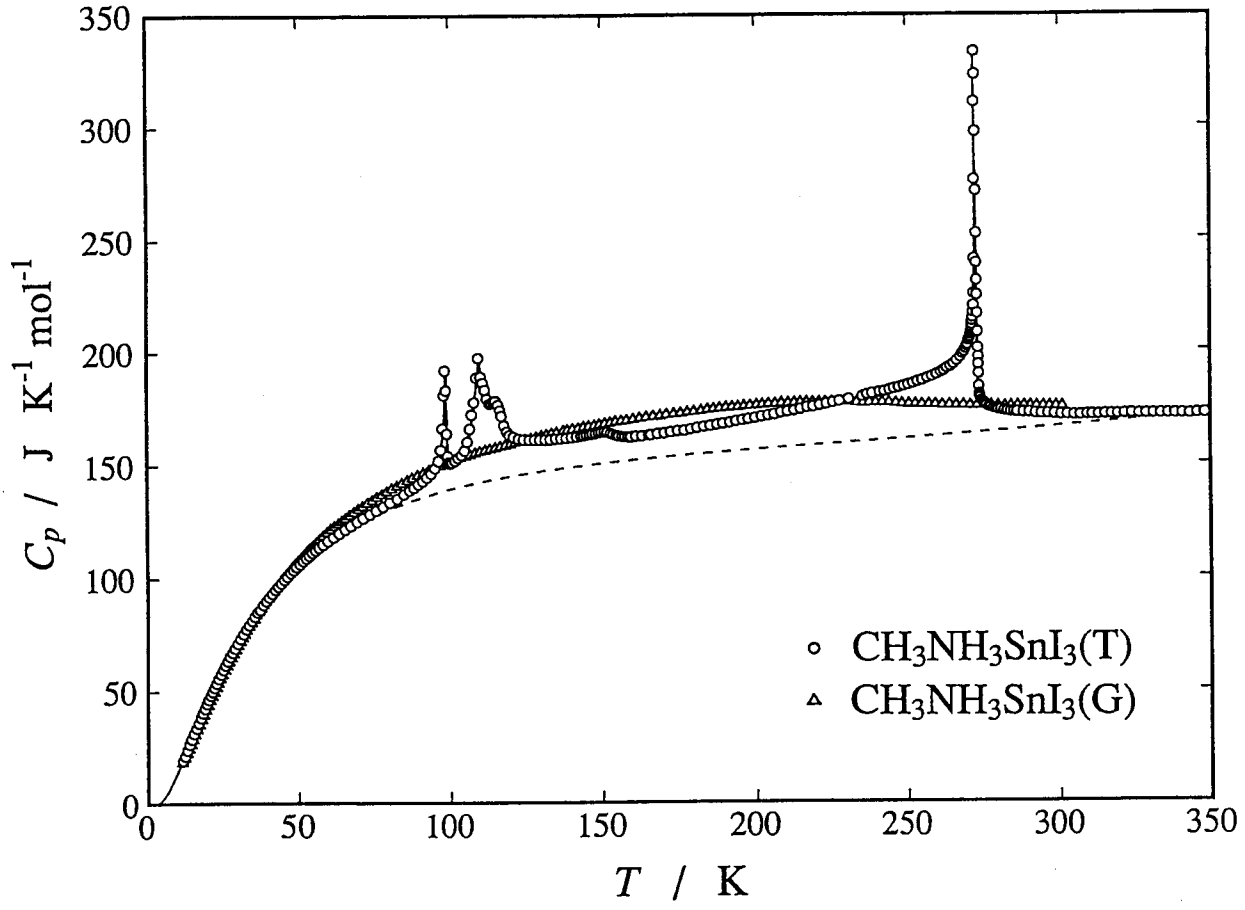

Fig. 5-4 Molar heat capacity of $CH_3NH_3SnI_3$(T) and $CH_3NH_3SnI_3$(G).

tion is accompanied by a strong precursory effect below the peak temperature. The similar effect has also been found in the highest temperature transition in $MAPbBr_3$ and $MAPbI_3$ (see Figs. 3-5 and 3-6). It is interesting that the heat capacities of the highest temperature phase are almost independent of temperature. Constant heat capacities were also found in the cubic phases of $MAPbX_3$ (X = Cl, Br, I) and $MASnBr_3$ (see Figs. 3-4, 3-5, 3-6 and 4-1). They appear to be a characteristic of the cubic phase of methylammonium halogenoperovskites.

No apparent anomaly was observed in $MASnI_3$(G). The heat capacity curve has a broad maximum near 230 K and slightly decreases above the temperature. In the temperature range lower than 80 K, where both of the curves are free from anomalies, the heat capacity of $MASnI_3$(G) is smaller than that of $MASnI_3$(T) below 40 K and larger above the temperature, as shown in Fig. 5-5. The two curves did not coincide with each other in the higher temperature region where both of the samples were cubic. The temperature at which their heat capacities become equal is estimated to be ~400 K by extrapolation.

5.3.2 Glass Transition in $MASnI_3$(G)

Figure 5-6 shows the spontaneous temperature drift rate recorded in the heat capacity measurement on $MASnI_3$(G) at temperatures between 60 and 160 K. The drift rate was determined at 17 min after each energy supply to the sample cell. Circles and triangles represent the data obtained on the samples cooled rapidly (10 K min^{-1}) and annealed at 115 K for 24 hours, respectively. The curve monotonically decreasing with temperature repre-

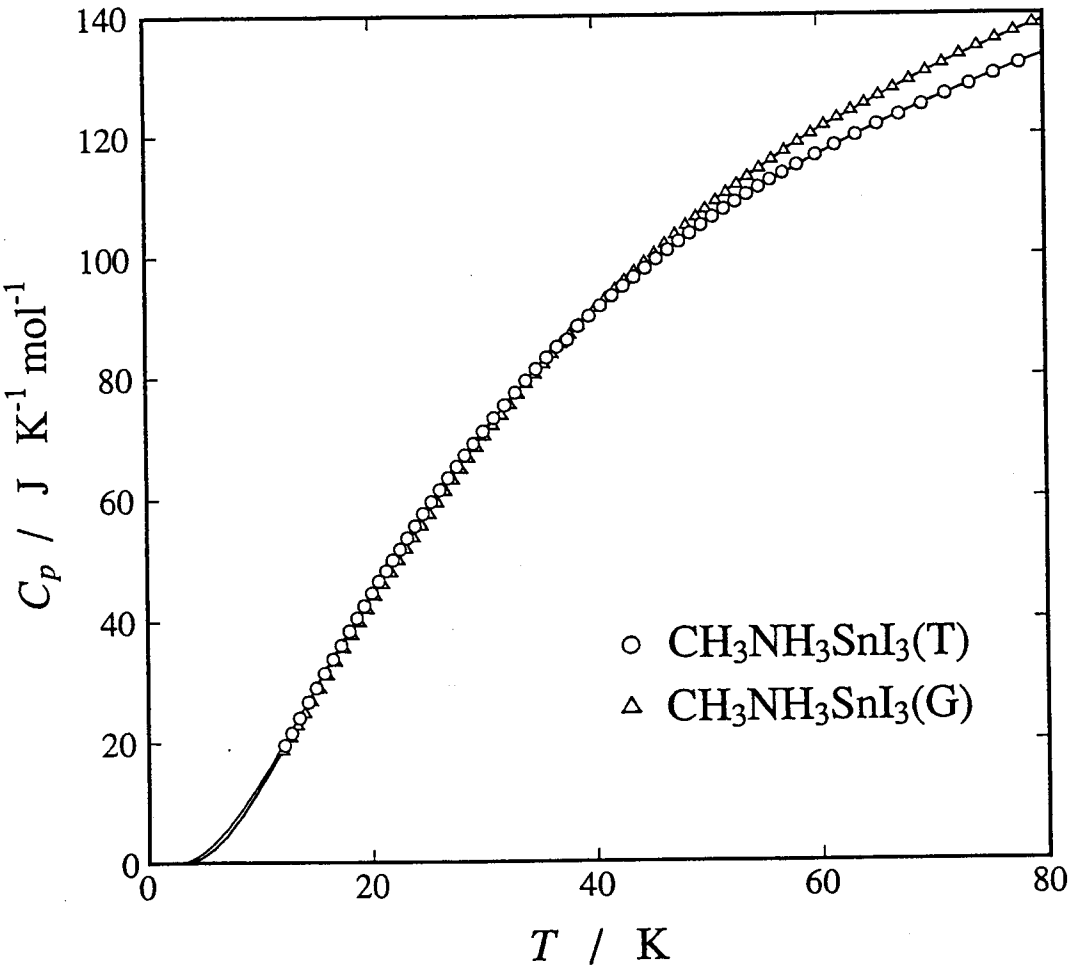

Fig. 5-5 Molar heat capacity of $CH_3NH_3SnI_3$(T) and $CH_3NH_3SnI_3$(G) below 80 K.

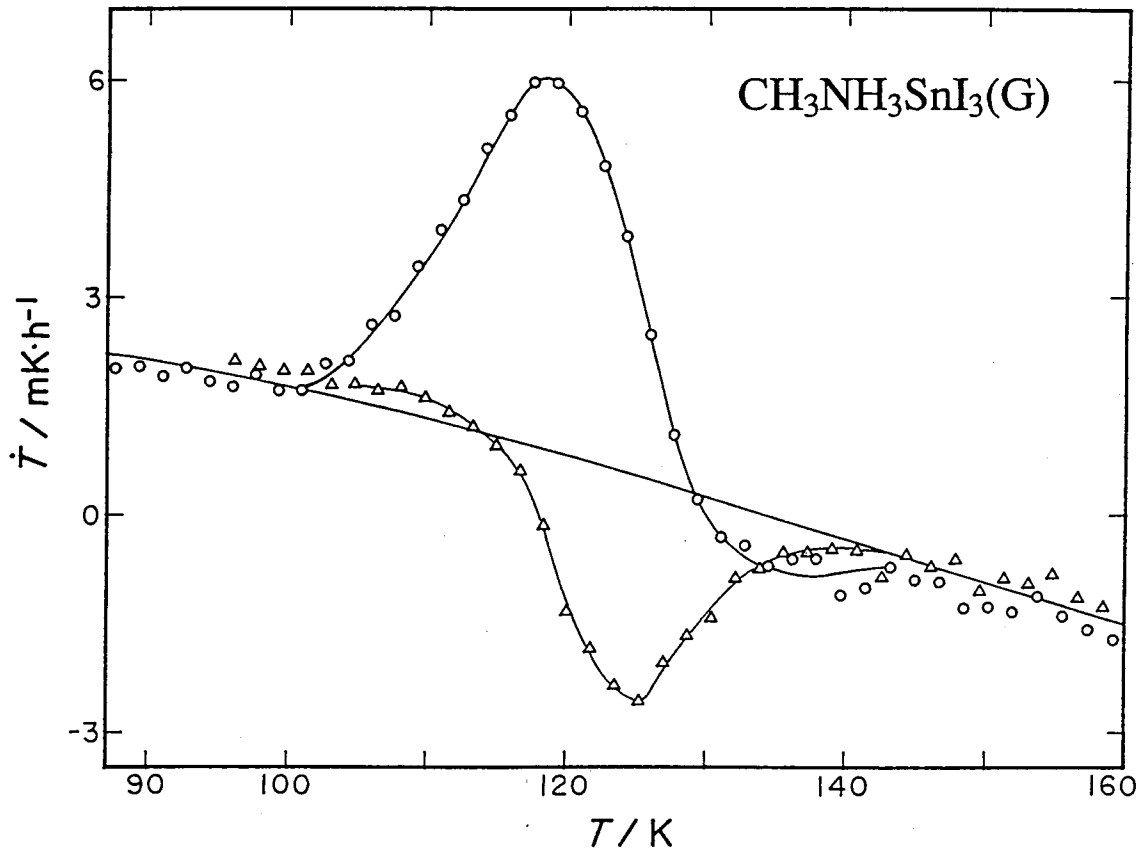

Fig. 5-6 Spontaneous temperature drift rates in the glass transition region of $CH_3NH_3SnI_3$(G).
○: cooled at 10 K min^{-1},
△: annealed at 115 K for 24 h.

sents the temperature drift rate due to incomplete adiabatic control. It was drawn by interpolation using the drift rate data in the temperature regions which are free from the endothermic or exothermic effect. In the rapidly cooled sample, the exothermic effect followed by endothermic one was observed. Only the endothermic one was observed in the annealed sample. This dependence of the drift rate on temperature and thermal history of the sample is characteristic of a glass transition. The anomalous temperature drifts were caused by the enthalpy relaxation from a non-equilibrium glassy state to the equilibrium state. The glass transition temperature was determined to be 129 K at which the sign of the drift rate changed from positive to negative. No apparent difference was observed in the heat capacities between the rapidly cooled and annealed samples.

5.3.3. Relaxation Time Analysis of $MASnI_3$(G)

In the first order reaction kinetics, the relaxation rate of configurational enthalpy dH_c/dT is related to the relaxation time τ by the relation,

$$\frac{d\Delta H_c}{dt} = -\frac{\Delta H_c}{\tau}. \qquad (5.1)$$

Here, ΔH_c is the enthalpy difference between the actual non-equilibrium state and the equilibrium state at the same temperature. Integration of this equation with time gives the following expression.

$$\Delta H_c(T, t) = \Delta H_c(T, 0)\ \exp(-t/\tau). \qquad (5.2)$$

Since the heat capacity including the sample cell did not change significantly over the temperature interval covered by the glass transition region, the equation can be rewritten by replacing the enthalpy with temperature,

$$T(t) = (T_0 - T_\infty) \exp[-(t/\tau)] + At + T_\infty . \qquad (5.3)$$

Here, $T_0 - T_\infty$ is the magnitude of the relaxation, T_0 the temperature at the beginning of the relaxation and A the heat leakage drift rate. The parameters T_0, T_∞ and A depend on the experimental conditions. However the parameter τ characterizes the relaxation and should be independent of the experimental details within the single τ approximation.

The long-time exothermic temperature evolution due to the enthalpy relaxation in the rapidly cooled sample was measured at several temperatures. The data were fitted to Eq. (5.3) by the least-squares method with four parameters, T_0, T_∞, A and τ. Figure 5.7 shows the typical temperature drifts and the fitted curves. In the present calculation, the natural temperature drift rate was treated as a parameter because better fit was obtained by doing so than by fixing the drift rate to the value determined by the interpolation (see Fig. 5.6). The drift rate at 114 K was 1.9×10^{-7} K s^{-1} from the interpolation and 4.7×10^{-7} K s^{-1} from the optimization. The relaxation times determined are 12.7 ks at 114 K and 3.9 ks at 123 K, respectively. Figure 5-8 shows the Arrhenius plots of the relaxation times in the glass transition region. The activation energy obtained from the plot is 16.6 kJ mol^{-1}.

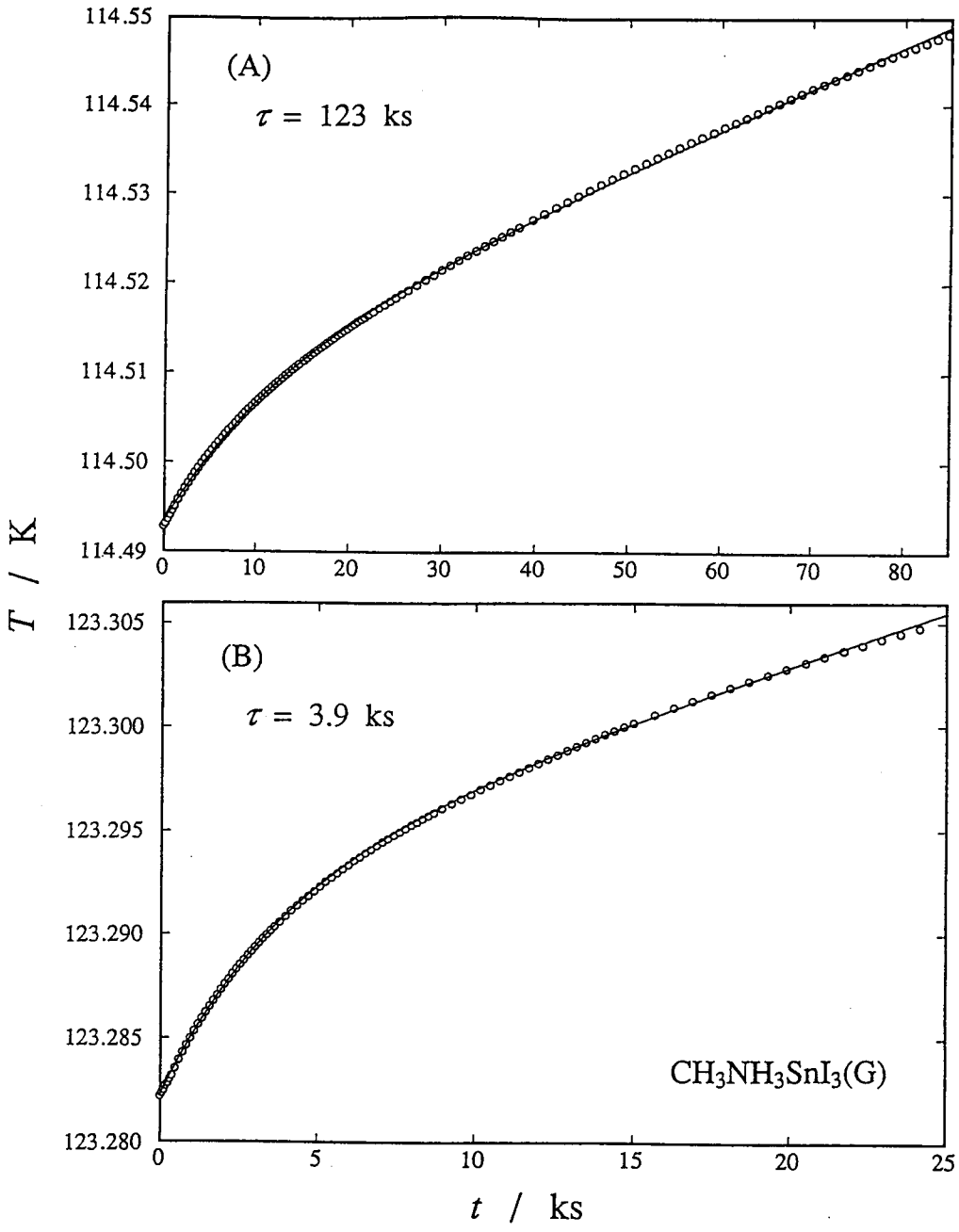

Fig. 5-7 Exothermic temperature drift curves due to enthalpy relaxation in the rapidly cooled sample of $CH_3NH_3SnI_3$(G).
(A): observed at 114 K,
(B): observed at 123 K.

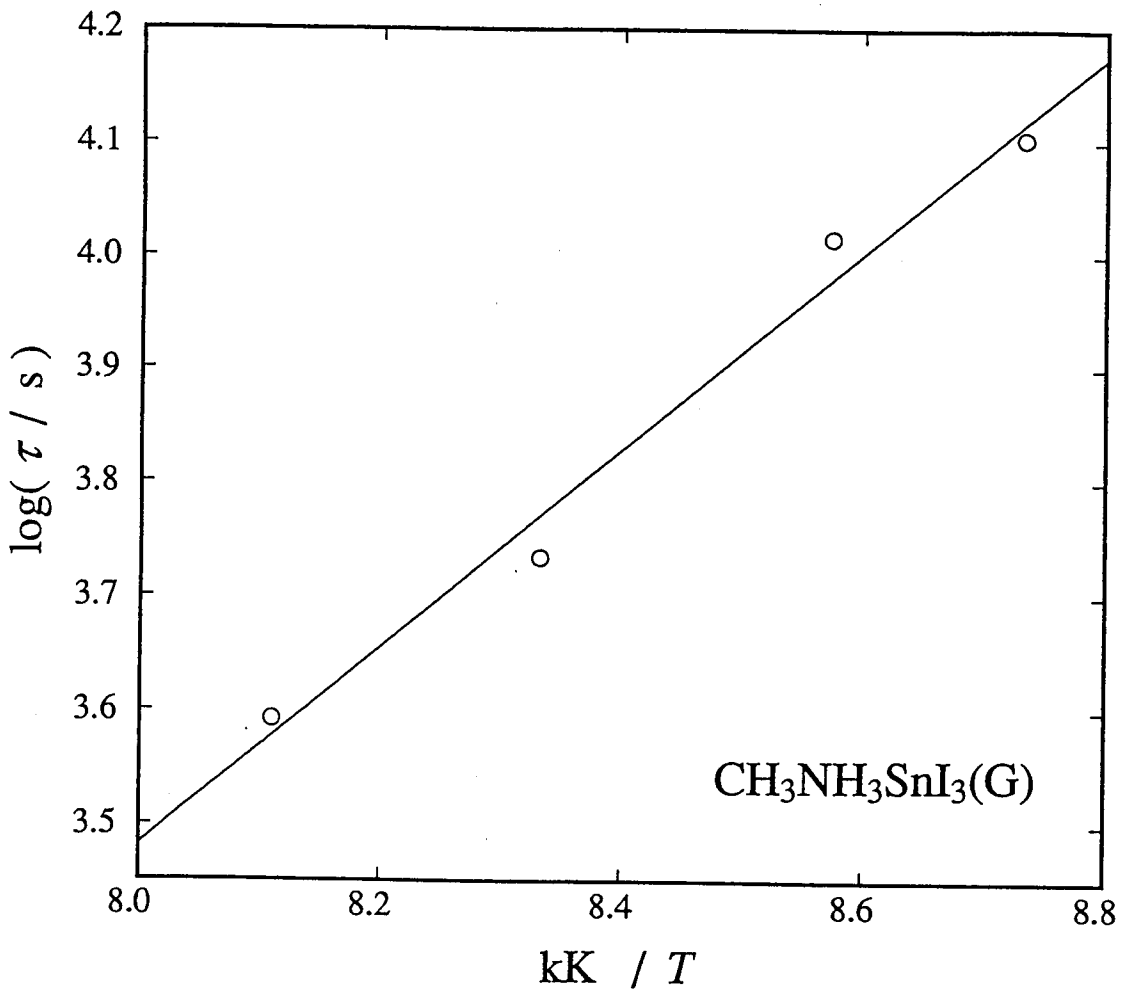

Fig. 5-8 Arrhenius plot of the relaxation time of $CH_3NH_3SnI_3$(G).

5.3.4 Enthalpy and Entropy of Phase Transition in $MASnI_3$(T)

The normal heat capacity of $MASnI_3$(T) was evaluated by the same method as that used for $MAPbX_3$ (X = Cl, Br, I) and $MASnBr_3$ (see Section 3.2 in Chapter 3). In the lack of spectroscopic data on $MASnI_3$, experimental vibrational frequencies of MA ion in $MAPbI_3$ were employed (see Table 3-1 in Chapter 3). For the external and internal rotations of MA ion, barrier heights of 5.8 kJ mol^{-1} determined for $MAPbI_3$ by NMR study [9] and 8.0 kJ mol^{-1} estimated for other MA compounds [10] were used in the calculation. At the beginning of the calculation, parameters to be optimized to reproduce the normal heat capacity were five Einstein temperatures, one Debye temperature, the $(C_p - C_v)$ correction coefficient A, and the transition temperature T_0 in the mean field approximation (see Section 3.2 in Chapter 3). It turned out that a better fitting was obtained by modifying the fitting function. The final fitting function contained the following parameters whose optimized values are as follows:

$$\theta_D^{1}(6) = 90.3 \text{ K},$$
$$\theta_E^{1}(2) = 31.3 \text{ K}, \quad \theta_E^{2}(3) = 74.8 \text{ K}, \quad \theta_E^{3}(6) = 165.5 \text{ K},$$
$$A = 9.49 \times 10^{-8} \text{ mol J}^{-1}, \quad T_0 = 188.4 \text{ K},$$

where the numbers in the parentheses give the degree of freedom and the superscripts distinguish different modes. The heat capacity data used in the least-squares determination of the above parameters are those in 12-76 K and 347-351 K. The normal heat capacity thus calculated is shown in Fig. 5-4 by the broken curve. Heat capacities below 12 K were also calculated in the same way.

The difference between the experimental and normal heat capacities is shown in Fig. 5-9. Integration of the excess heat capacity and the addition of the discontinuous part at the phase transition gave the transition enthalpy and entropy. The temperature dependence of the accumulated transition entropy thus calculated is shown in Fig. 5-10. The arrows in the figure show the phase transition temperatures. Since the phase transitions were overlapped each other, as shown in Fig. 5-9, they were divided at 100.4 K and 135.0 K where the excess heat capacity took the minimum. The 109.4 K and 114.7 K transitions and the 150.5 K and 272.3 K ones were not separated because of the small entropies of the 114.7 K and 150.5 K transitions. Figure 5-11 shows the temperature dependence of the transition entropy around the 272.3 K transition in a magnified scale. It should be noted that the discontinuous part of the transition entropy is extremely small, in contrast to the large value of the entropy change of this phase transition (12.9 J K mol^{-1}). The discontinuous part, 0.2 J K^{-1} mol^{-1}, corresponds to only 1.5 % of the transition entropy. The small discontinuity in the transition entropy and a strong precursory effect on the heat capacity (see Fig. 5-9) indicate a character of the higher order phase transition. The same has also been found in the tetragonal I-cubic phase transition in $MAPbX_3$. The discontinuous parts of the transition entropies are 4～6 % for the lead compounds (see Section 3.3 in Chapter 3).

The thermodynamic quantities associated with the phase transitions are given in Table 5-3. The entropy of the 272.3 K transition corresponds to R ln 4.7. The value ($\geq R$ ln 2) indicates that the transition is of an order-disorder type. The sum of the

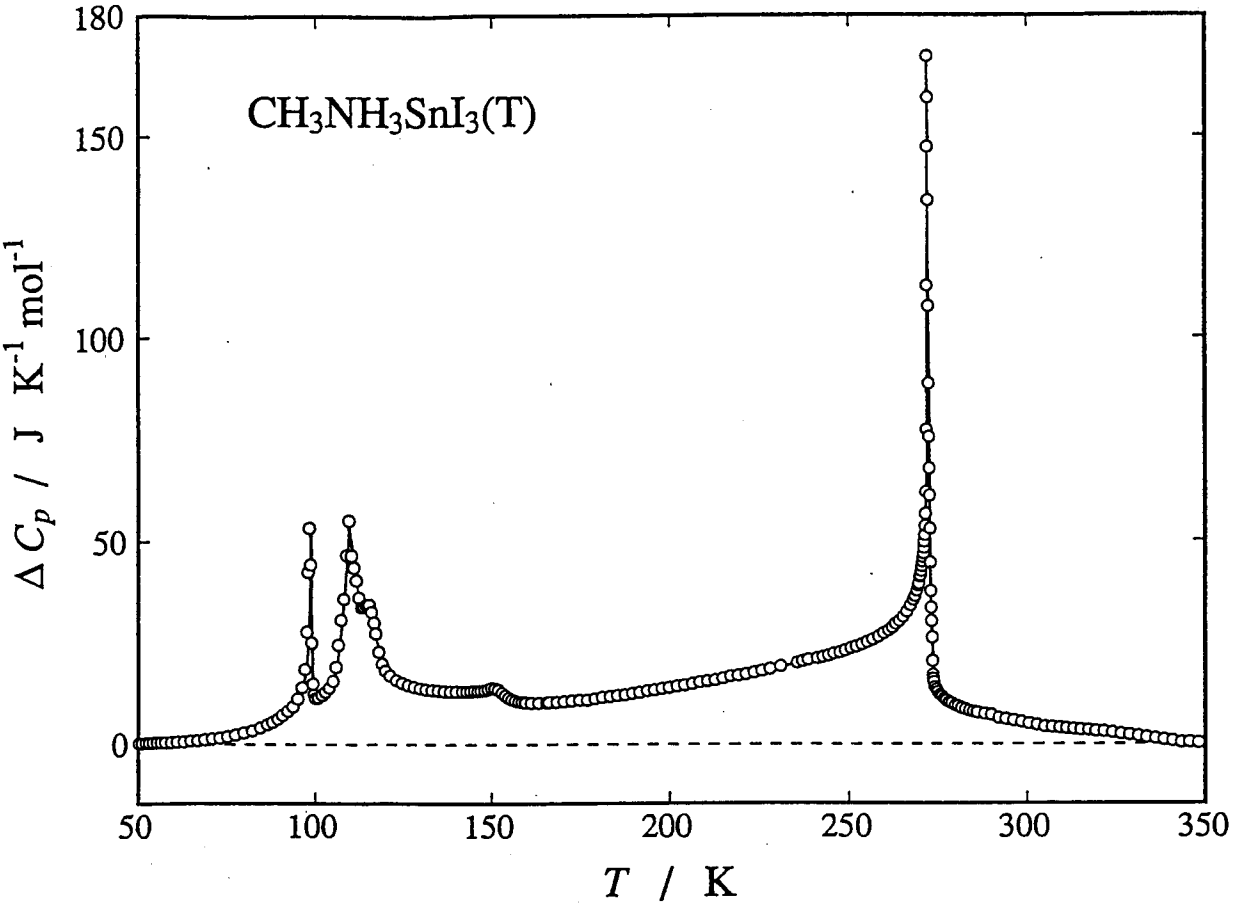

Fig. 5-9 Excess heat capacity of $CH_3NH_3SnI_3$(T).

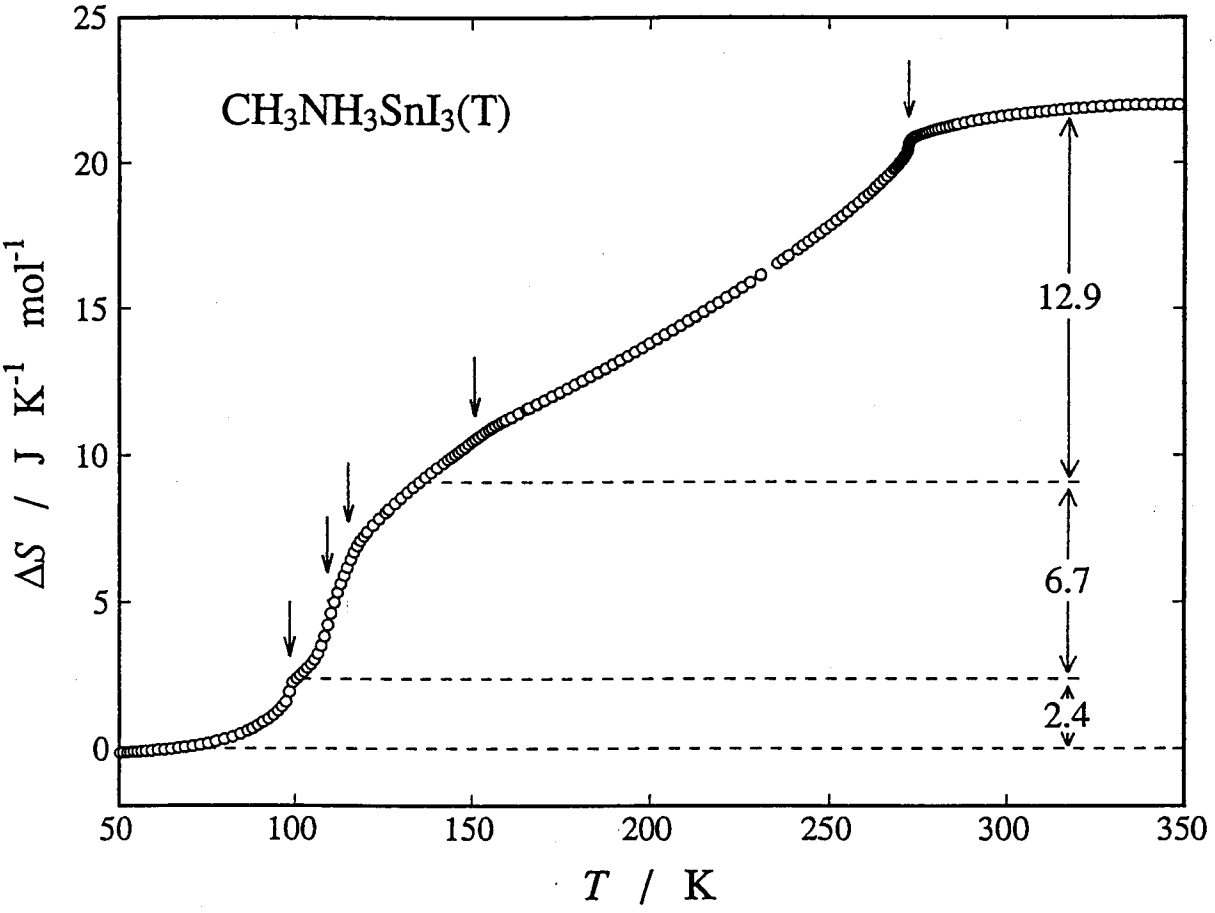

Fig. 5-10 Temperature dependence of the accumulated transition entropy of $CH_3NH_3SnI_3$(T).

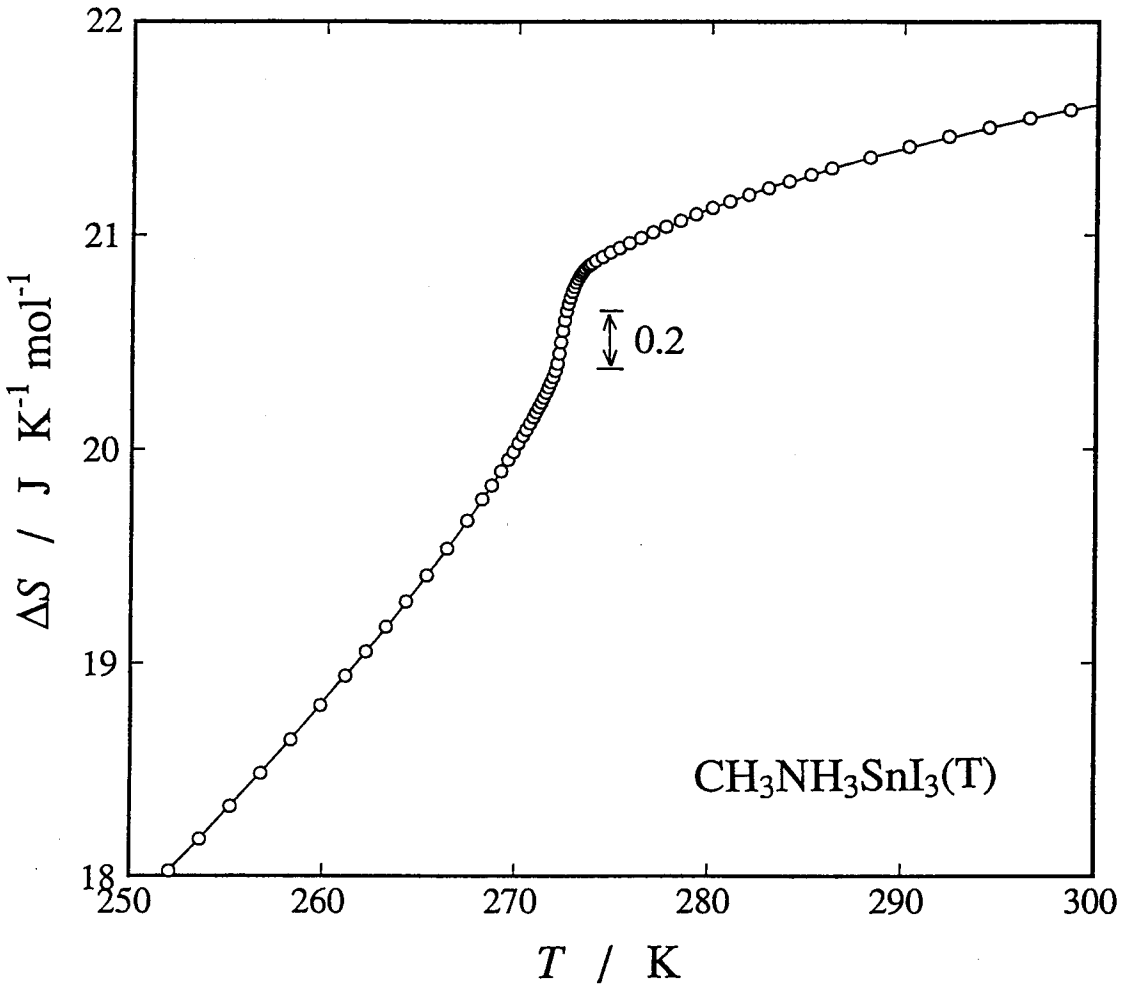

Fig. 5-11 Temperature dependence of the accumulated transition entropy of $CH_3NH_3SnI_3$(T) around the phase transition at 272.3 K.

Table 5-3 Temperatures, enthalpies and entropies of the phase transitions of $CH_3NH_3SnI_3$(T).

T_{trs} / K	$\Delta_{trs}H$ / kJ mol^{-1}	$\Delta_{trs}S$ / J K^{-1} mol^{-1}
98.5	0.23	2.4
109.4 114.7	0.77	6.7 (R ln 2.2)
150.5 272.3	2.83	12.9 (R ln 4.7)

entropy of the other transitions corresponds to R ln 3.0. The total entropy of the phase transition is 22.0 J K^{-1} mol^{-1}. Corresponding entropy values are 24~29 J K^{-1} mol^{-1} for $MAPbX_3$ (X = Cl, Br, I) and 25 J K^{-1} mol^{-1} for $MASnBr_3$. The steps by which the ordering proceeds in $MASnI_3$(T) are different from those in $MASnBr_3$ and $MAPbX_3$. The structure of the lowest temperature phase of $MASnI_3$(T) is not known at present. Assuming that the MA ions in the cubic phases of $MAPbX_3$ (X = Cl, Br, I) and $MASnX_3$ (X = Br, I(T)) are disordered in the same manner, close values of the transition entropy indicate that the MA ions in the lowest temperature phases are ordered to the same extent in these compounds.

5.3.5 Standard Thermodynamic Functions of $MASnI_3$(T) and $MASnI_3$(G)

Standard thermodynamic functions derived from the calorimetric data are summarized in Tables 5-4 and 5-5 for $MASnI_3$(T) and $MASnI_3$(G), respectively. For T < 12 K where the heat capacities were not measured, they are calculated by using the known vibrational frequencies, barriers of hindered rotations and optimized Debye and Einstein parameters for $MASnI_3$(T) (see Section 3.3). For $MASnI_3$(G), the heat capacity below 12 K was evaluated by the same method as the determination of the normal heat capacity for $MAPbX_3$. The same values as for $MASnI_3$(T) were used for the spectroscopic data and the barrier heights of hindered rotations. Of the parameters to be optimized, two Einstein temperatures each with weight 3 were combined to one Einstein temperature with weight 6 and the (C_p - C_V) correction coefficient A was fixed to zero. The following parameters were determined by the least-

Table 5-4. Thermodynamic functions of $CH_3NH_3SnI_3$(T).

$\frac{T}{K}$	C_p/R	$(H-H_0)/RT$	S/R	$-(G-H_0)/RT$
10	(1.630)	(0.4522)	(0.5949)	(0.1427)
20	5.355	1.969	2.861	0.8921
30	8.514	3.646	5.656	2.010
40	10.91	5.177	8.450	3.273
50	12.70	6.510	11.09	4.575
60	14.04	7.659	13.53	5.866
70	15.09	8.647	15.77	7.123
80	16.02	9.511	17.85	8.335
90	17.05	10.29	19.79	9.501
100	18.16	11.09	21.72	10.62
110	23.12	11.88	23.60	11.72
120	19.59	12.65	25.44	12.79
130	19.35	13.17	26.99	13.82
140	19.48	13.62	28.43	14.81
150	19.78	14.02	29.78	15.77
160	19.52	14.37	31.05	16.68
170	19.69	14.67	32.23	17.56
180	19.94	14.96	33.37	18.41
190	20.20	15.23	34.45	19.22
200	20.50	15.48	35.50	20.01
210	20.79	15.73	36.50	20.77
220	21.10	15.97	37.48	21.51
230	21.45	16.20	38.42	22.23
240	21.80	16.42	39.34	22.92
250	22.20	16.65	40.24	23.59
260	22.80	16.87	41.12	24.25
270	24.46	17.11	42.01	24.89
273.15	25.12	17.24	42.33	25.09
280	20.86	17.33	42.86	25.52
290	20.72	17.45	43.58	26.13
298.15	20.63	17.54	44.16	26.62
300	20.61	17.56	44.28	26.72
310	20.58	17.66	44.96	27.30
320	20.65	17.75	45.61	27.86
330	20.64	17.84	46.25	28.41
340	20.62	17.92	46.87	28.95
350	20.66	18.00	47.46	29.47

Table 5-5. Thermodynamic functions of $CH_3NH_3SnI_3$(G).

$\frac{T}{K}$	C_p/R	$(H-H_0)/RT$	S/R	$-(G-H_0)/RT$
10	(1.527)	(0.3835)	(0.4911)	(0.1076)
20	5.160	1.870	2.673	0.8028
30	8.354	3.515	5.389	1.873
40	10.94	5.061	8.161	3.100
50	12.95	6.446	10.83	4.381
60	14.50	7.665	13.33	5.667
70	15.72	8.732	15.66	6.930
80	16.71	9.670	17.83	8.159
90	17.53	10.50	19.84	9.346
100	18.20	11.24	21.73	10.49
110	18.73	11.90	23.49	11.59
120	19.14	12.48	25.14	12.65
130	19.55	13.01	26.68	13.67
140	19.90	13.49	28.15	14.66
150	20.18	13.93	29.53	15.60
160	20.43	14.33	30.84	16.51
170	20.65	14.69	32.08	17.39
180	20.84	15.03	33.27	18.24
190	21.02	15.34	34.40	19.06
200	21.16	15.63	35.48	19.86
210	21.26	15.89	36.52	20.63
220	21.31	16.14	37.51	21.37
230	21.30	16.36	38.46	22.09
240	21.25	16.57	39.36	22.80
250	21.20	16.75	40.23	23.48
260	21.14	16.92	41.06	24.14
270	21.10	17.08	41.86	24.78
273.15	21.09	17.12	42.10	24.98
280	21.08	17.22	42.62	25.40
290	21.06	17.35	43.36	26.01
298.15	21.05	17.46	43.95	26.49
300	21.05	17.48	44.08	26.60

squares method with the heat capacity data below 40 K.

$\theta_D^1(3)$ = 83.8 K, $\theta_E^1(2)$ = 34.7 K, $\theta_E^2(3)$ = 55.8 K,
$\theta_E^3(3)$ = 115.3 K, $\theta_E^4(6)$ = 147.6 K,

where the numbers in the parentheses give the degrees of freedom and the superscripts distinguish different modes.

At room temperature, no difference was recognized in the diffraction patterns between $MASnI_3(T)$ and $MASnI_3(G)$. It can be regarded that the MA ions of both samples are randomized to the same extent. $MASnI_3(G)$ underwent no phase transition at the low temperature. Therefore the crystal was expected to retain the disorder to the lowest temperature. By estimating the total entropy at 400 K where the heat capacities of $MASnI_3(T)$ and $MASnI_3(G)$ approach each other, it was found that $MASnI_3(T)$ has 1.2 J K^{-1} mol^{-1} larger entropy than $MASnI_3(G)$. This indicates that $MASnI_3(G)$ loses most of the orientational entropy due to the MA ion at the lowest temperature. The process of decreasing entropy may be described as development of short range order. The MA ions are orientationally disordered independently of each other at the high temperature. With decreasing temperature, orientational short-range ordering among neighboring MA ions grows. This is indicated by the excess heat capacity of a significant magnitude over the wide temperature range (see Fig. 5-4). If the complete orientationally ordered state is realized at the lowest temperature, the entropy decrease associated with this ordering is expected to be 20~30 J K^{-1} mol^{-1} by comparison with the transition entropy of $MAPbX_3$ and other member of $MASnX_3$. The entropy change in $MASnI_3(T)$ (22 J K^{-1} mol^{-1}) shows that the actual situa-

tion is close to this picture. Most of the orientational entropy carried by MA ions at 300 K is lost at temperatures between 300 and 10 K in which temperature region the sample $MASnI_3$(G) does not exhibit any phase transition. The short range ordering is not complete as the glass transition (T_g = 129 K) shows. Magnitude of the remaining disorder may be estimated if one attaches a significance to the residual entropy of $MASnI_3$(G) relative to $MASnI_3$(T). The residual entropy, 1.2 J K^{-1} mol^{-1} indicates that orientation of 10~20 MA ions is correlated at the lowest temperature. It roughly equals the number of the nearest and second nearest neighbors (6 + 12 = 18). In the other halogenoperovskites, orientational ordering of MA ions develops stepwise as the crystals undergo phase transitions. The reason why $MASnI_3$(G) alone behaved in this peculiar way is not known at present.

5.4 DC Conductivity

As will be described in the next section (Section 5.5), these samples are very sensitive to the pressurization. The $MASnI_3$(T) sample without heat treatment after disk preparation shows no phase transition. Removal of the effect of the pressure by thermal annealing applied was checked by the DTA measurement.

Figure 5-12 shows the temperature dependence of the dc conductivity of $MASnI_3$(T) and $MASnI_3$(G). Circles and triangles represent $MASnI_3$(T) and $MASnI_3$(G), respectively. Open and closed symbols denote the data obtained on heating and cooling. Arrows indicate the transition temperatures determined by the heat capacity measurement (see Section 3.1). The conductivities of the

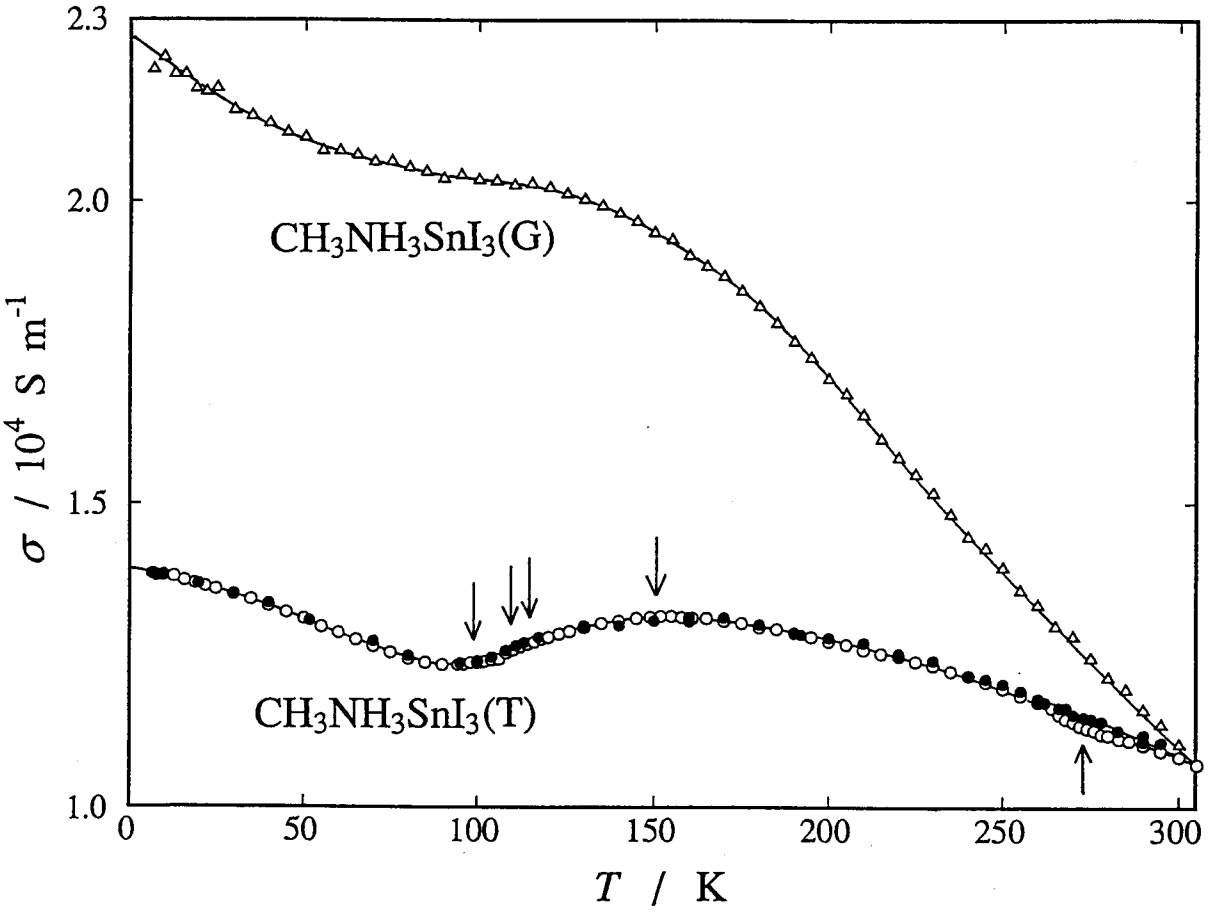

Fig. 5-12 Temperature dependences of the dc conductivities of $CH_3NH_3SnI_3$(T) and $CH_3NH_3SnI_3$(G).

two samples happened to be the same at 300 K. But they differed markedly at lower temperature, though they are similar with respect to the uneven temperature dependence. A drastic change was expected at the phase transitions for $MASnI_3$(T) in analogy with $MASnBr_3$. Actually there was none except for a small thermal hysteresis observed around the 272.3 K transition, as indicated by the arrow in Fig. 5-12. The conductivity in the temperature region around the low temperature transitions are shown in Fig. 5-13 in a magnified scale. The conductivity curve is hardly influenced by the phase transitions in any significant way. However, the positive slope between 100 and 150 K may be connected with the phase transition and disordering of MA ions. The disordering may also be responsible to the plateau of the conductivity observed in $MASnI_3$(G) between 100 and 150 K, because it was shown above that there is an excess (orientational) contribution to the heat capacity of $MASnI_3$(G) in the same temperature region. Negative slope of the conductivity with increasing temperature in $MASnI_3$(G) can be accepted as an indication of metallic conductivity in the observed temperature range. $MASnI_3$(T) also shows metallic behavior except in the temperature region between 100 and 150 K.

5.5 High Pressure DTA

5.5.1 Pressure Dependence of the DTA Curves of $MASnI_3$(T)

The DTA curve at each pressure was taken in the order of decreasing pressure from the maximum pressure applied. For $MASnI_3$(T), the pressure was applied four times in all. The shape of the DTA peak changed as the pressure was applied repeatedly.

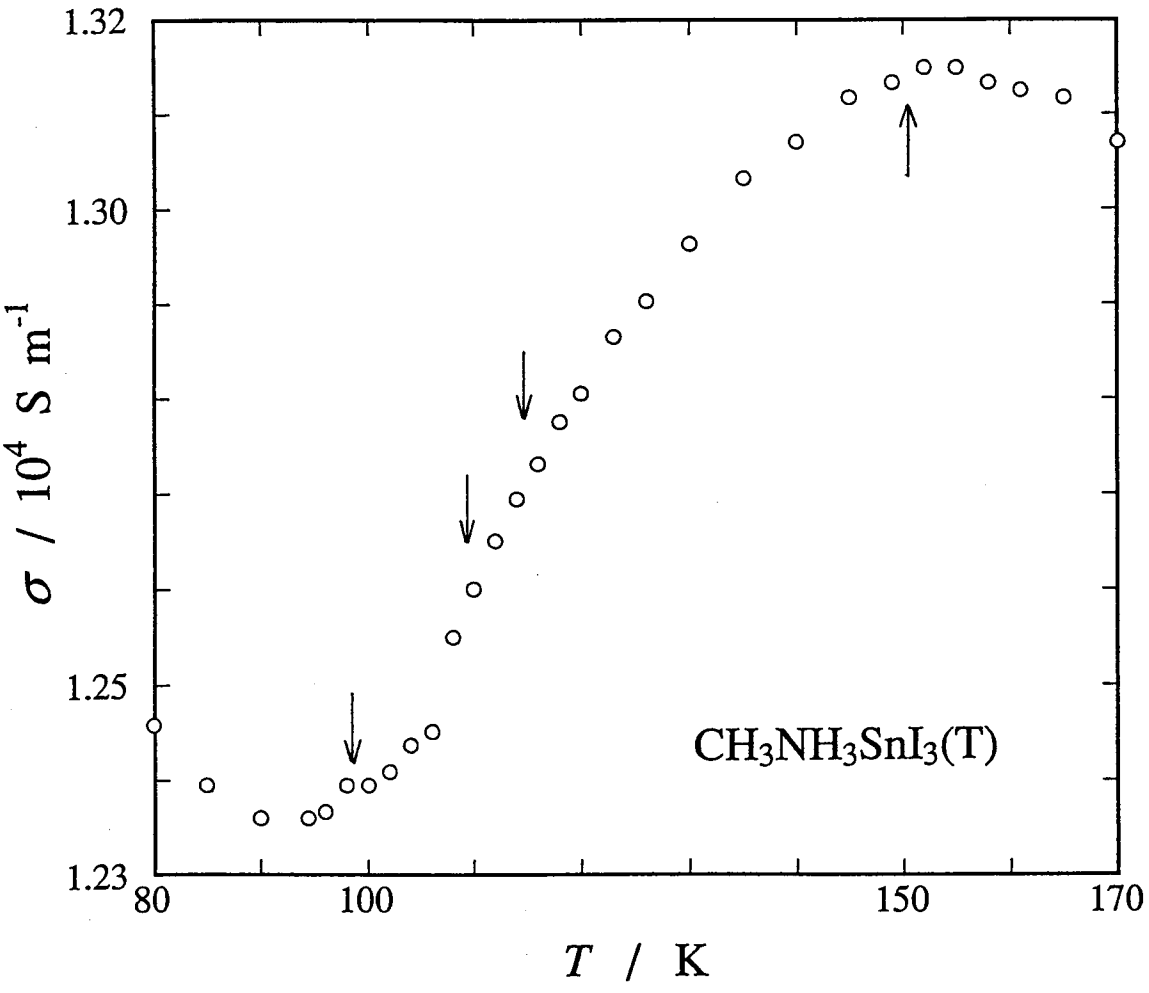

Fig. 5-13 Temperature dependence of the dc conductivity of $CH_3NH_3SnI_3$(T) around the phase transitions in the low temperature range.

Figure 5-14 shows the experimental DTA curves at 0.1 MPa (atmospheric pressure) observed before and after pressurization. The curves (A) was obtained before pressurization, (B) after the first pressurization and (C) after the fourth pressurization. The heating rate was 0.8-1.2 K min^{-1} and 0.8-0.9 K min^{-1} for the low and high temperature regions, respectively. Three endothermic peaks were observed in each curve. Their temperatures agree with each other and with those observed in the heat capacity measurement at 0.1 MPa (see Section 3.1). The phase transitions at 114.7 K and 150.5 K observed in the calorimetry at 0.1 MPa (see Section 3.1) were not detected in the DTA measurement. As is clear from the figure, the peaks broadened as the measurement was repeated. In the curve (C) where the broadening is most severe, the peaks in the low temperature region are only slightly above the noise level, while the peak at 271.2 K also broadened considerably.

The peak at the highest temperature (~271 K at 0.1 MPa) shifted monotonically to higher temperatures with increasing pressure. The peak shape and area did not change significantly with the increased pressure, even though the peaks broadened on repeated high pressure measurement as discussed in the previous paragragh referring to Fig. 5-14. This fact indicates that the nature of the phase transition does not change significantly.

The experimental DTA curves under various pressures in the low temperature region are shown in Fig. 5-15. They were observed after the first pressurization up to 156 MPa. At 155.9 MPa (curve (A)), only one endothermic peak was observed at 116.1 K. With decreasing pressure, the peak shifted to lower tempera-

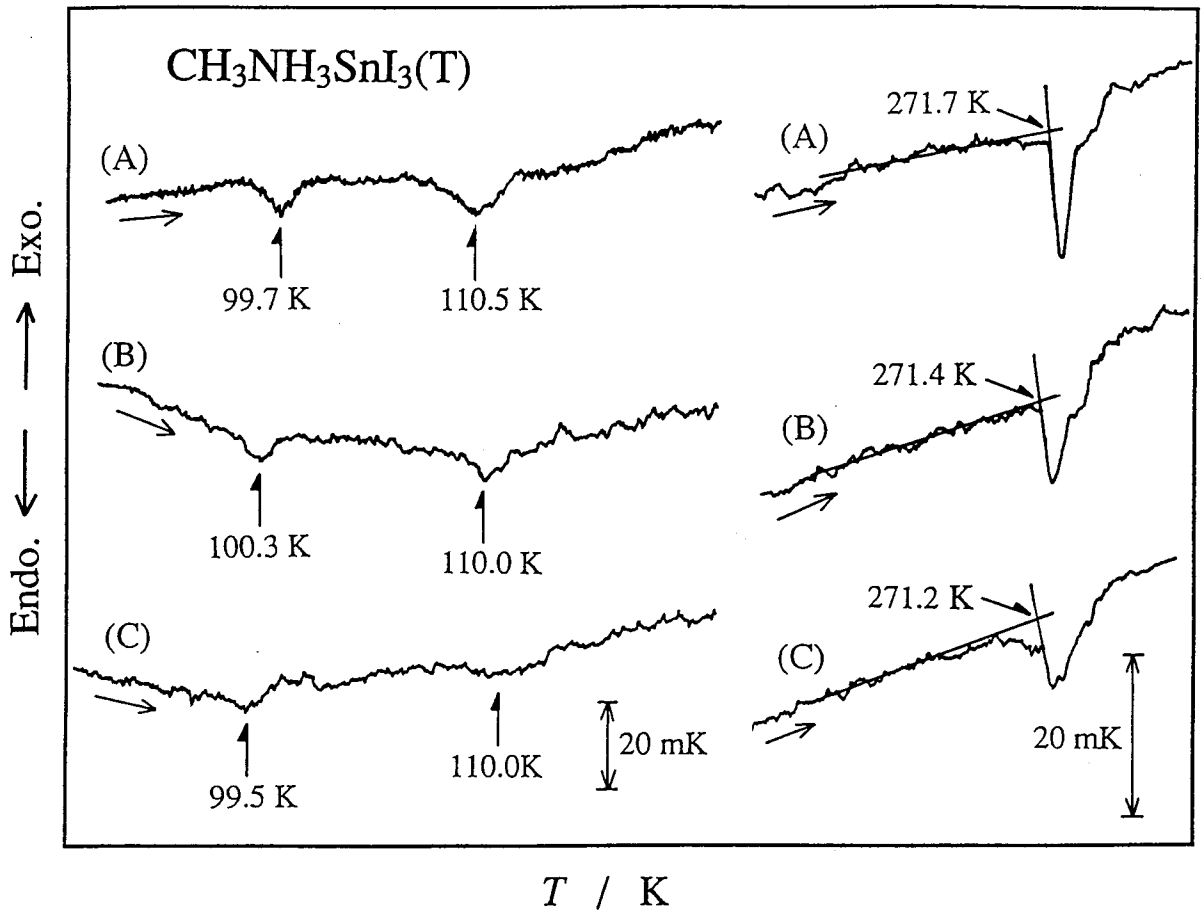

Fig. 5-14 DTA curves of $CH_3NH_3SnI_3$(T) at 0.1 MPa before and after pressurization.
(A): before pressurization, (B): after the first pressurization, (C): after fourth.
The arrows indicate the transition temperatures.

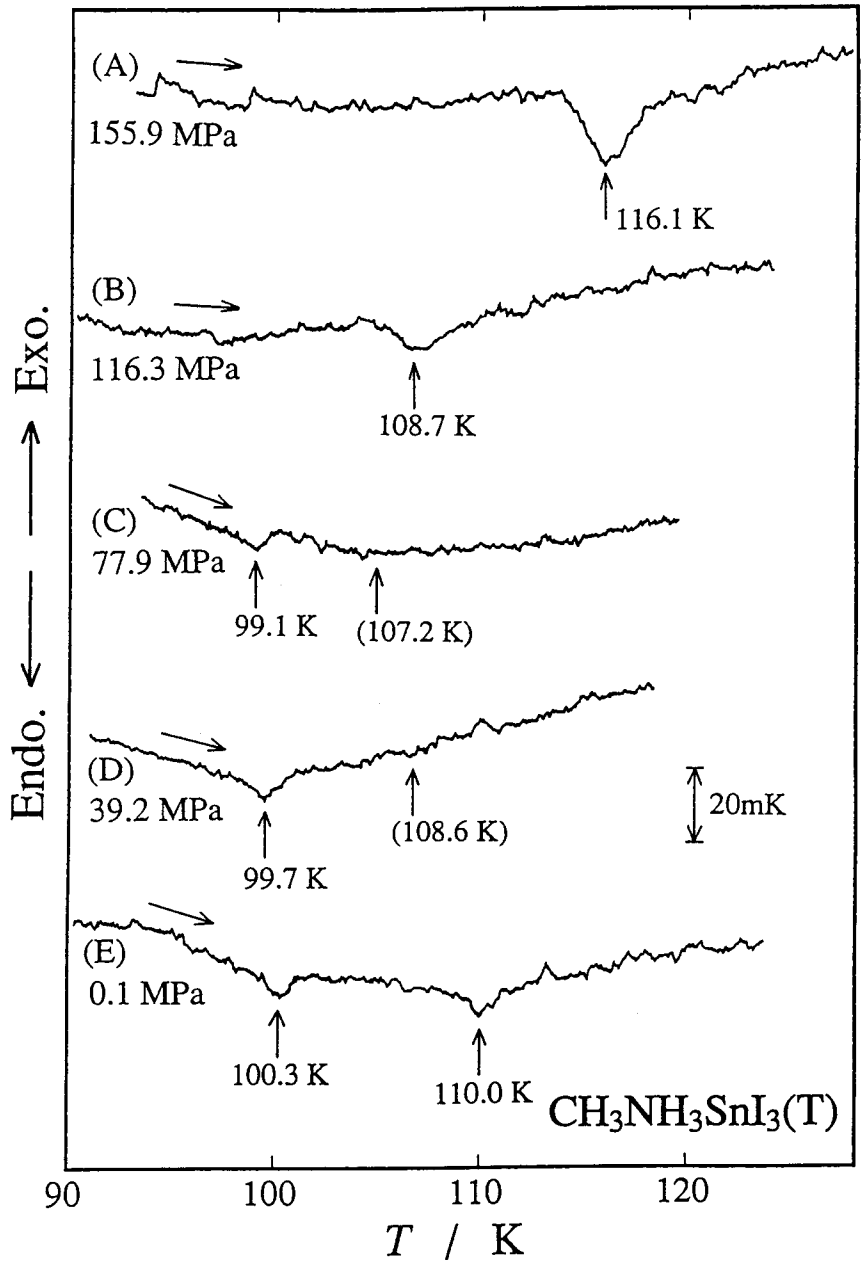

Fig. 5-15 DTA curves of $CH_3NH_3SnI_3$(T) under various pressures in the low temperature range.

tures. At 116.3 MPa (curve (B)), the peak was observed at 108.7 K. The pressure dependent behavior was complicated at lower pressures. At 77.9 MPa (curve (C)), a very small peak was barely observed at 99.1 K. At 39.2 MPa (curve (D)), a small peak was observed at 99.7 K. The peak temperature is higher than that in the curve (C). At 0.1 MPa (curve (E)), two peaks were observed at the same temperatures as were observed before pressurization. The arrows with temperature values in parentheses represent the phase transitions which were recognized by the further investigation (described below). From Fig. 5-15, one may expect a triple point at a pressure between 77.9 and 116.3 MPa. However, the actual pressure-temperature phase diagram is more complicated. This is because the peak observed at the higher pressure has a positive pressure dependence whereas the two peaks observed at the lower pressure have negative ones. As is apparent from Fig. 5-15, it is very difficult to distinguish peaks from noise levels. To elucidate the pressure-dependent behavior, further experiment with higher sensitivity was required.

Figure 5-16 shows experimental DTA curves observed at 19.6 MPa after the second pressurization. The curve (A) is obtained with a chopper type microvolt amplifier and the curve (B) with a photo-coupled nanovolt amplifier. The heating rate was 1.0-1.1 K min^{-1}. One can barely see the endothermic peak at 100.1 K and scarcely find the one at 109.3 K in the curve (A). In contrast, two peaks are observed at 100.1 and 109.3 K in the curve (B).

Figure 5-17 shows experimental DTA curves under several pressures between 85.5 and 98.9 MPa. The curves (A), (B) and (C) were obtained after three times pressurization and the curves (D)

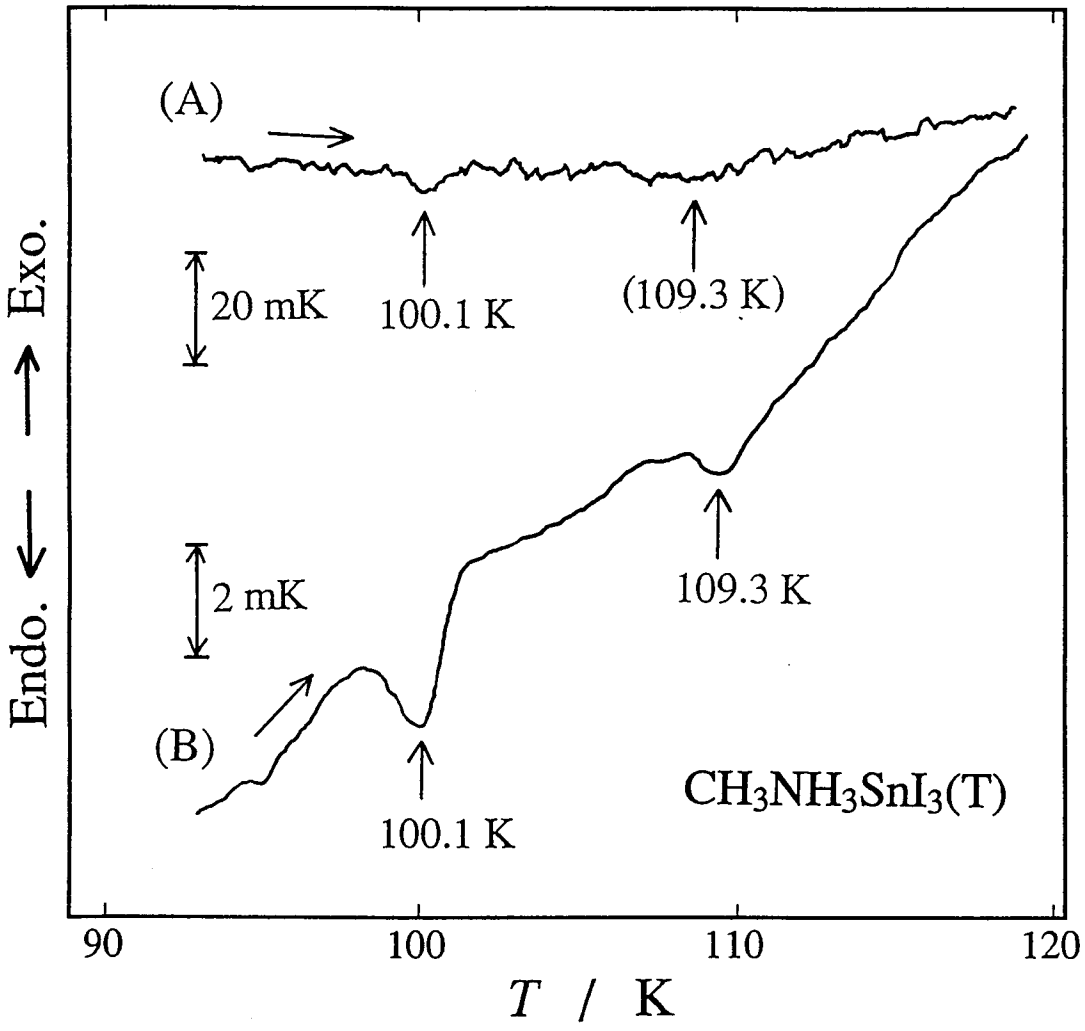

Fig. 5-16 DTA curves of $CH_3NH_3SnI_3$(T) at 19.6 MPa after second pressurization.

(A): with a chopper microvolt amplifier,

(B): with a photo-coupled nanovolt amplifier.

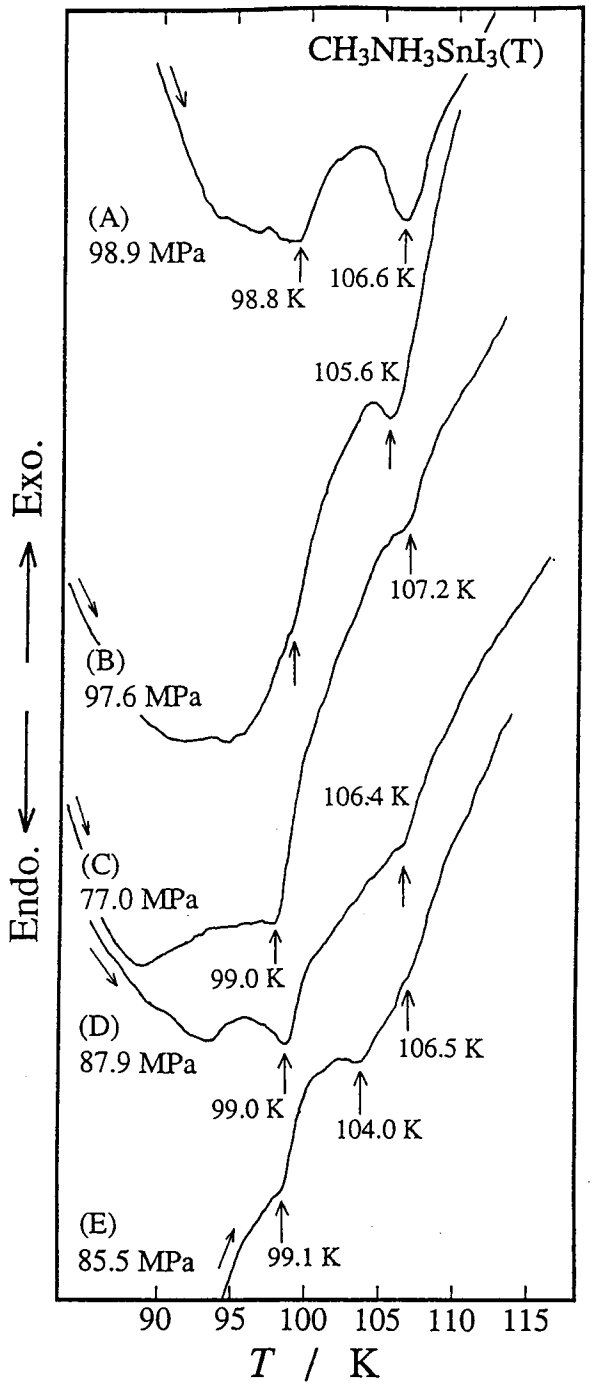

Fig. 5-17 DTA curves of $CH_3NH_3SnI_3$(T) under various pressures in the low temperature range. (A), (B) and (C) were obtained after third pressurization and (D) and (E) after fourth. (E) was obtained by annealing at 101.6 K for 7 hours after cooling down to 84 K.

and (E) after four times. The heating rate was 0.9-1.0 K min^{-1}. At 98.9 MPa (curve (A)), two endothermic peaks occurred at 98.8 and 106.6 K, respectively. At 97.6 MPa (curve(B)), only one peak was observed at 105.6 K. The arrow without a temperature value indicates the location of 98.8 K on the curve where the peak was observed at 98.9 MPa in the curve (A). No apparent peak was observed around this temperature. At 77.0 MPa, two peaks were observed at 99.0 and 107.2 K, respectively. Disappearance of the peak at the lower temperature in the curve (B) suggests that the peak is due to the phase transition between the metastable phases at this pressure. A triple point is expected to exist at a pressure lower than 97.6 MPa. The temperature shift of the peak at the higher temperature was not monotonical and the peak became smaller with decreasing pressure. This suggests that the three peaks observed in the curves (A), (B) and (C) at 105.6-107.2 K are due to the phase transitions belonging to different, at least two, transition lines. Another triple point may exist at around these pressures. To clarify the metastable transition line and to reveal the triple point, further investigation was carried out. At 87.9 MPa, two endothermic peaks were observed at 99.0 and 106.4 K, respectively. After cooling down to 84 K, the sample was annealed at 101.6 $\pm$ 0.5 K for 7 hours. Three peaks were observed in the measurement after annealing (curve E). A new peak was found at 104.0 K. The peak temperatures of the others, 99.1 and 106.5 K, agree with those observed before the annealing. The peak at 99.1 K is obviously smaller than before. These observations indicate that the peak at 99 K is due to the transition between the metastable phases at this pressure. Thus, it

became clear that there exists a second triple point at a lower pressure than 85 MPa, and above the pressure a new phase appears. Appearance of the new peak at 104 K confirms the transition line which connects the two triple points. On comparing the area and the temperature of the peak, it became clear that the phase transition observed at 105.6 K at 97.6 MPa is on the transition line connecting the two triple points and that observed at 106.6 K at 98.9 MPa is on the transition line at above the pressure of the triple point.

5.5.2 Pressure-Temperature Phase Relation of $MASnI_3(T)$

Figure 5-18 depicts the pressure-temperature phase diagram of the $MASnI_3(T)$ crystal obtained in the present DTA study. The broken line indicates the metastable transition line. The phase transitions which were not observed here (114.7 K and 150.5 K in the calorimetry at 0.1 MPa) are not shown in the figure. The temperature region between 120 and 260 K is left out. The space group, tetragonal I4/mcm, for one of the intermediate temperature phase was concluded in the X-ray diffraction study (see Section 1.2). The structures of the other phases are not known at present. They are denoted by the symbols A, B, C and HP for convenience. Two triple points were found in the narrow pressure range. Their locations are (~59 MPa, 99.4 K) and (98 MPa, 106 K), respectively. The phase transition between the lowest temperature phase (C) and the high pressure phase (HP) was not observed in the present measurement. The transition line between these phases in Fig. 5-18 was arbitrarily drawn. Even though it is obviously desirable to examine the p-T region at lower temper-

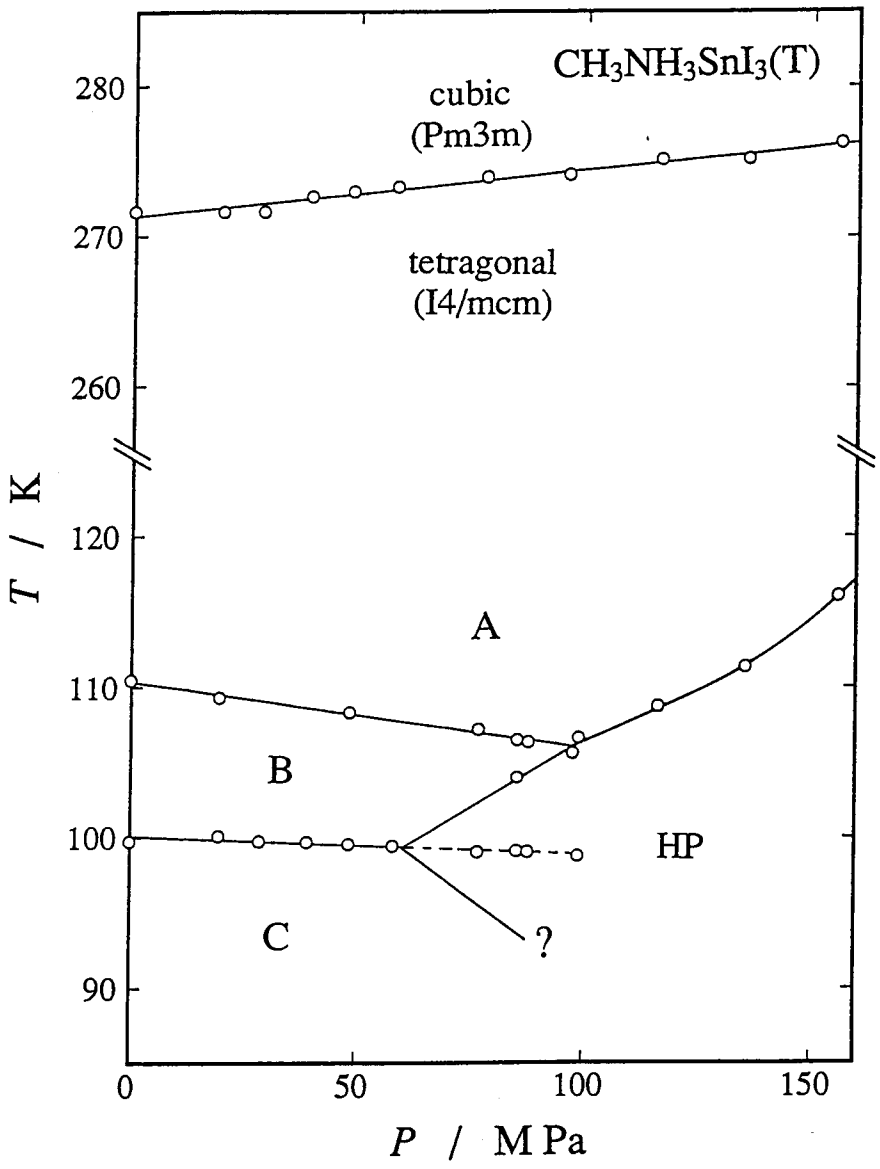

Fig. 5-18 *p-T* phase diagram of $CH_3NH_3SnI_3$(T) crystal. The temperature range of 120 - 260 K is omitted. The broken line indicates the metastable phase boundary. The transition line with a question mark was not observed. It was drawn arbitrarily.

ature, it was not practicable because of the coolant limitation.

The phase boundaries between the phases C and B, between the phases B and A and between the tetragonal and cubic phases are essentially straight lines in the pressure range studied here. Their slopes dT_{trs}/dP are -1.2, -4.5 and 3.1 x 10^{-2} K MPa^{-1}, respectively. The phase boundary between the HP phase and the phase A is downward convex. The positive(negative) slope indicates the increase(decrease) of the molar volume as the temperature is traversed from below. The volume changes associated with the phase transition which were derived by using the Clausius-Clapeyron's equation (Eq. (3-11)) are -0.03, -0.30 and 0.40 cm^3 mol^{-1} for the III-II, II-I and the tetragonal-cubic transitions, respectively. Here, the values of the transition entropy $\Delta_{trs}S$ derived from the calorimetric measurement at atmospheric pressure (from Table 5-3) were used. The volume changes are quite small (0.02, 0.2 and 0.3 %, respectively) as compared with the molar volume (146 cm^3) [8]. It is to be noted that the molar volume of the cubic phase is larger than that of the tetragonal phase. For $MAPbX_3$ (X = Cl, Br, I), the molar volume of the cubic phase is smaller than that of the tetragonal phase (in the iodide, for p > 120 MPa) (see Section 5.2 in Chapter 3). The molar volume of the cubic phase of $MASnBr_3$ is also smaller than the intermediate phase, although the structure of the latter is not known (see Section 5.2 in Chapter 4).

For $MAPbX_3$ (X = Cl, Br, I), a general statement was made on the phase diagram: the stability domain of the tetragonal phase narrows at higher pressure both below and above (see Section 5.2 in Chapter 3). For $MASnX_3$ (X = Br, I), however, one cannot find

such a simple general relation in the phase diagram.

References to Chapter 5

1. D. Weber, *Z. Naturforsch.*, 33b, 862 (1978).
2. K. Yamada, T. Tsuritani, T. Okuda and S. Ichiba, *Chem. Lett.*, 1325 (1989).
3. K. Yamada, T. Matsui, T. Tsuritani, T. Okuda and S. Ichiba, *Z. Naturforsch.*, 45a, 307 (1990).
4. J. Barrett, S. R. Bird, J. D. Donaldson and J. Silver, *J. Chem. Soc. A*, 3105 (1971).
5. S. J. Clark, C. D. Flint and J. D. Donaldson, *J. Phys. Chem. Solid*, 42, 133 (1981).
6. J. D. Donaldson, J. Silver, S. Hadjiminolis and S. P. Ross, *J. C. S. Dalton*, 1500 (1975).
7. K. Yamada, S. Nose, T. Umehara, T. Okuda and S. Ichiba, *Bull. Chem. Soc. Jpn.*, 61, 4265 (1988).
8. A. Poglitsch and D. Weber, *J. Chem. Phys.*, 87. 6373 (1987).
9. Q. Xu, T. Eguchi, H. Nakayama, N. Nakamura and M. Kishita, *Z. Naturforsch.*, 46a. 240 (1991).
10. R. Ikeda, Y. Kume and D. Nakamura, *J. Magn. Reson.*, 24, 9 (1976).

Chapter 6

GENERAL DISCUSSION

6.1 Transition Entropy

Five methylammonium halogenoperovskites studied in the present thesis have the cubic perovskite structures in the highest temperature phases and undergo phase transitions (excepting $MASnI_3$(G)). All of the phase transitions observed in $MAPbX_3$ (X = Cl, Br, I) are first order phase transitions of the order-disorder type. Transition entropies were accounted for with the models of orientational disorder of an MA ion assuming that the MA ion is completely ordered with respect to both the C-N axis itself and around the C-N axis in the lowest temperature phases. In contrast to $MAPbX_3$, phase behavior of $MASnX_3$ is complicated. In addition to two first-order phase transitions of the order-disorder type, a higher order phase transition of the displacive type was found at low temperature (46 K) for $MASnBr_3$. For $MASnI_3$, four successive phase transitions were found in the narrow temperature range, 95 - 150 K, in addition to the first order phase transition of the order-disorder type at 273 K. Figure 6-1 summarizes the transition entropies of these compounds. For the Pb compounds, the broken lines between the histogramic bars indicate probable structural correspondence between respective phases of the different crystals. The broken lines in the bars (for the Sn compounds) indicate that the transition entropies presented are the sum of the two unresolved transitions. The steps by which the ordering proceeds in the Sn compounds are

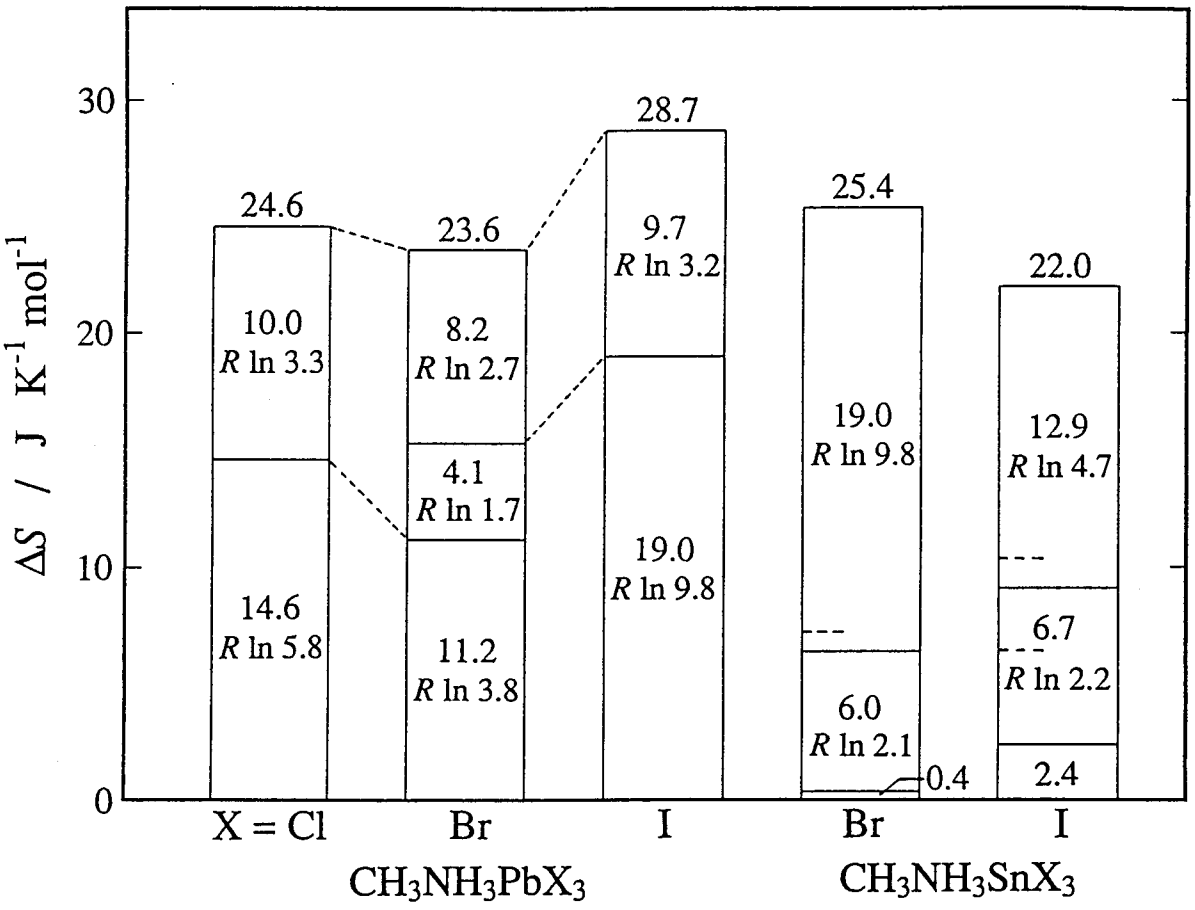

Fig. 6-1 Transition entropy of $CH_3NH_3PbX_3$ (X = Cl, Br, I) and $CH_3NH_3SnX_3$ (X = Br, I).

different from those in the Pb compounds, as indicated by the different sequences of the transition entropies. However, the total amounts of the transition entropies are close to each other, which are 22～29 J K^{-1} mol^{-1}. Thus, all of the five methylammonium halogenoperovskites have the same extent of disorder in the highest temperature phases.

6.2 The Ionic Packing and the Transition Temperatures

The ionic radii used in this section were taken from Shannon's table for the ionic radii [1] and are reproduced in Table 6-1.

In the perovskite structure, each MA ion is surrounded by twelve halogen ions. The maximum radii of the contact sphere in which the MA ion is situated are calculated from the lattice constants [9,10,11] and the ionic radii of halogens as follows;

$MAPbCl_3$: 220 pm, $MAPbBr_3$: 221 pm, $MAPbI_3$: 227 pm,
$MASnBr_3$: 220 pm, $MASnI_3$: 221 pm.

While the values increase with increasing the size of halogen as expected, there is no significant difference between the values for the Pb and Sn compounds. For MAI which has the CsCl type cubic structure in the highest temperature phase (ε phase, a = 486 pm) [2], the radius of the contact sphere is 201 pm. The value is about 10 % smaller than those for the perovskites. This fact suggests that the reorientational motion of the MA ion in the perovskites is closer to free rotation than in MAI.

Table 6-2 shows the $M^{2+}-X^-$ distances derived from the lattice constants $R_{exp.}$ and from the ionic radii (the sum of the

Table 6-1 Shannon's effective ionic radii used in Chapter 6

ions	CN	*r*/pm
Cs^{+}	12	188
Rb^{+}	12	172
K^{+}	12	164
Pb^{2+}	6	119
Sn^{2+}	6	93
Mg^{2+}	6	72
Zn^{2+}	6	75
Co^{2+}	6	75 (HS)
Mn^{2+}	6	83 (HS)
Cd^{2+}	6	95
F^{-}	6	133
Cl^{-}	6	181
Br^{-}	6	196
I^{-}	6	220

CN: coordination number, HS: high spin.

R. D. Shannon, *Acta Crystallogr.*, A32, 751 (1976).

Table 6-2 $M^{2+}-X^{-}$ distances, $R_{exp.}$ and $R_{calc.}$, derived from the lattice constants and from the ionic radii, respectively in ABX_3 (A=MA, Cs, B=Pb, Sn, X=F, Cl, Br, I).

Compounds	a/pm	$R_{exp.}$/pm	$R_{calc.}$/pm	ref.
$CsPbCl_3$	560.5	280.3	300	3,4
$CsPbBr_3$	587.4	293.7	315	4,5
$CsPbI_3$	~618	309	339	5
$CsSnF_3$	447	223.5	226	6
$CsSnCl_3$	556	278	274	7
$CsSnBr_3$	580	290	289	7,8
$CsSnI_3$	~615	307.5	313	8
$MAPbCl_3$	567.5	283.8	300	9
$MAPbBr_3$	590.1	295.1	315	9
$MAPbI_3$	632.9	316.5	339	9
$MASnBr_3$	589	295	289	10
$MASnI_3$	624	312	313	11

ionic radii of M^{2+} and X^-) $R_{calc.}$. The table also includes analogous perovskites containing Cs^+ in place of MA^+. The value of $R_{calc.}$ is evidently larger than that of $R_{exp.}$ in Pb compounds. This may indicate that the bonds between the Pb and X (halide) ions have appreciable covalent character. The variation in the lattice constant on replacing Cs by MA is larger in the Sn compounds than in the Pb compounds. This may be related to the covalent character in the Pb compounds.

To understand the distortions from the cubic structure of ABO_3 perovskites, the relation between the radii of the A, B and O^{2-} ions has been discussed in terms of the tolerance factor t defined by the following equation,

$$r_A + r_0 = \sqrt{2}\, t\, (r_B + r_0). \qquad (6\text{-}1)$$

The closer t is unity, the more complete is the contact of all the (spherical) atoms in the structure. Figure 6-2 shows the dependence of the noncubic-cubic transition temperatures on the tolerance factor in halogen perovskites. In addition to MA compounds, the figure also includes the data on $CsPbX_3$ [9], $CsSnX_3$ [10,11], $CsGeX_3$ [12], NH_4MF_3 [13,14,15], KMF_3 [14,16] and $RbMF_3$ [15,17]. Closed symbols indicate the compounds for which the cation has no orientational degree of freedom (*i. e.* monatomic cations) and opened ones that the cation can be orientationally disordered. The ionic radius of the MA ion was taken to be 201 pm calculated from the lattice constant of the ε phase of MAI and the standard value of the ionic radius of I^-. The ionic radius of the NH_4^+ ion, 154 pm, was derived from the lattice constant of NH_4MgF_3 which is the smallest among those of the

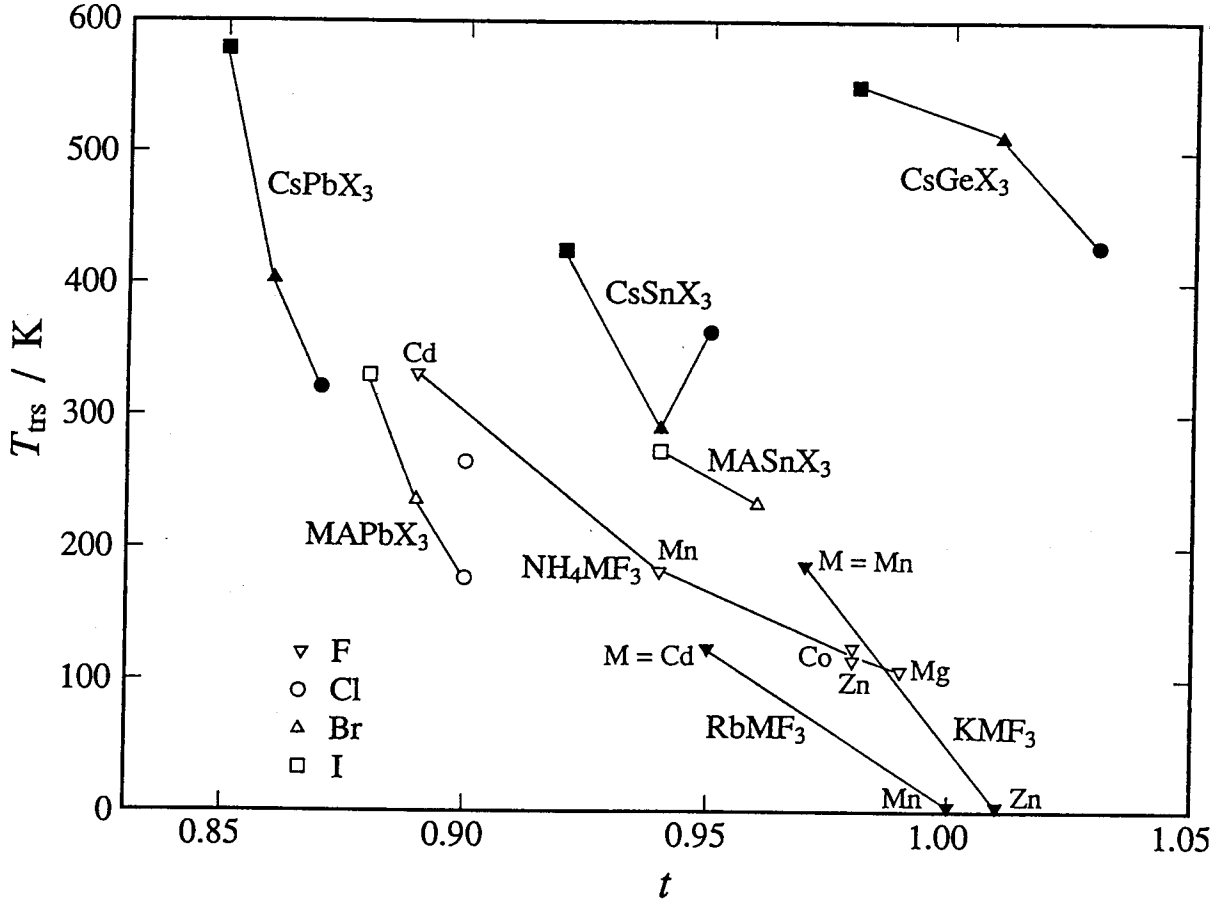

Fig. 6-2 Dependence of the noncubic-cubic transition temperatures on the tolerance factor in halogen perovskites.

NH_4MF_3 compounds presented here. As is apparent from Fig. 6-2, the transition temperatures decrease as the tolerance factor approaches unity. There is no obvious division in the plot between the compounds with orientational degrees of freedom and those without. This was unexpected because the large transition entropy associated with the orientational disorder might influence the stability of the cubic phase and drastically reduce the transition temperature. However, it has to be remembered that the transition temperature is determined by the relation:

$$T_{trs} = \Delta_{trs}H/\Delta_{trs}S, \qquad (6.2)$$

for a first order transition. An essentially same relation holds for a higher order transition. The large transition entropies of the MA perovskites are counterbalanced by large transition enthalpies, thus resulting in the transition temperatures which are not much different from those of the simple halide perovskites. A significance of the plot in Fig. 6-2 is that much larger energies are associated with a given value of $|1-t|$ in the MA perovskites than in the simple perovskites. This, in its turn, indicates that the molecular forces responsible for the phase transition are different among the different perovskite crystals even though they do fit well in the argument employing the tolerance factor.

References to Chapter 6

1. R. D. Shannon, *Acta Crystallogr.*, A32, 751 (1976).
2. H. Ishida, N. Matsuhashi, R. Ikeda and D. Nakamura, *Chem. Lett.*, 1859 (1985).
3. J. Hutton, R. J. Nelmes, G. M. Meyer and V. R. Eiriksson, *J. Phys. C. Solid State Phys.*, 12, 5393 (1979).
4. M. Sakata, J. Harada, M. J. Cooper and K. D. Rouse, *Acta Crystallogr.*, A36, 7 (1980).
5. C. K. Møller, *Mat. Fys. Medd. Danske Vindensk Selsk.*, 32, No. 2 (1959).
6. J. D. Donaldson and J. Silver, *J. C. S. Dalton*, 666 (1973).
7. J. Barrett, S. R. Bird, J. D. Donaldson and J. Silver, *J. Chem. Soc. A*, 3105 (1971).
8. K. Yamada, T. Matsui, T. Tsuritani, T. Okuda and S. Ichiba, *Z. Naturforsch.*, 45a, 307 (1990).
9. A. Poglitsch and D. Weber, *J. Chem. Phys.*, 87, 6373 (1987).
10. K. Yamada, S. Nose, T. Umehara, T. Okuda and S. Ichiba, *Bull. Chem. Soc. Jpn.*, 61, 4265 (1988).
11. K. Yamada, T. Tsuritani, T. Okuda and S. Ichiba, *Chem. Lett.*, 1325 (1989).
12. G. Thiele, H. W. Rotter and K. D. Schmidt, *Z. anorg. allg. Chem.*, 545, 148 (1987).
13. R. B. Helmholdt, G. A. Wiegers and J. Bartolome, *J. Phys.*, C13, 5081 (1980).
14. R. Navarro, R. Burriel, J. Bartolome and D. Gonzalez, *J. Chem. Thermodyn.*, 18, 1135 (1986).
15. E. Palacios, R. Navarro, R. Burriel, J. Bartolome and D. Gonzalez, *J. Chem. Thermodyn.*, 14, 1713 (1981).

16. J. Hutton and R. J. Nelmes, *J. Phys. C. Solid State Phys.*, 14, 1713 (1981).

17. A. Kornblit and G. Ahlers, *Phys. Rev.*, B8, 5163 (1973).